Quantitative Magnetophoresis of Micro and Nano Particles

Timothy D. Meehan

A dissertation submitted to the faculty of the University of North Carolina at Chapel Hill in partial fulfillment of the requirements for the degree of Doctor of Philosophy in the Department of Chemistry.

Chapel Hill
2008

Approved by:

Richard Superfine

Mark Wightman

Royce Murray

Leandra Vicci

James Jorgenson

Abstract

Timothy D. Meehan: Quantitative Magnetophoresis of Micro and Nano Particles
(Under the Direction of Richard Superfine and Mark Wightman)

Micro- and nanoscale magnetic particles are becoming increasingly utilized in a variety of settings. Magnetophoresis is commonly used in diagnostic devices, research applications, and medicinal science. The applications of magnetophoresis in drug delivery, gene transfection, and hyperthermic treatment of tumours are in the initial phases of development.

While a large body of work in magnetophoresis exists, here are few reports of the relevant magnetophoretic parameters of a system being quantitatively correlated with driven particle mobility. The relationships between the size, shape, and magnetic properties of the particles, the applied magnetic field, and the viscosity of the medium are relevant to particle magnetophoresis and the design of magnetophoretic systems.

The investigation described here begins with the room temperature magnetic characterization of the three particles used: commercial beads, nanorods, and for the first time ferritin. Ferritin is a magnetic protein which has been used extensively in a research context for labelling biological particles, however such systems have not been quantifiably characterized to enable the development of loading/force causal relationships. Here, a model platform was used to correlate for the first time, the quantified ferritin loading, the empirically determined magnetic properties of the ferritin labelled particles, and the magnetophoretic forces.

The quantified magnetophoresis of spheres and rods in a model viscous medium and shear thinning polymer networks was performed for the first time. This investigation also represents the first report of particle shear thinning of DNA. The decreasing viscosity experienced by the particles in DNA points toward potential implications for considering the benefits of particle induced shear thinning in the designing of magnetic particle drug delivery systems.

In the final investigation, the results of the previous chapters are brought together in the fabrication and magnetophoresis of a novel, ferritin based, rod shaped, biocompatible, nanoparticles. For the first time, magnetophoresis of the nanoparticles is demonstrated and validated by spatially resolved Raman spectroscopic analysis of the magnetically concentrated material. This dual component magnetic particle has potential application in the fabrication of new functionally graded biomaterials and drug and gene delivery.

Acknowledgements

There are many individuals who assisted, both professionally and personally, in the creation of this document. I would like to offer my appreciation to my wonderful friends and family for your undying support, patience, and confidence.

I would like to thank my advisors, and committee members for their guidance and professional development. I am grateful for the scientific and personal support provided by the members of the Nano Science Research Group (NSRG) throughout my graduate career. Thanks to Dr. Michael Stadermann for your insights and encouragement, to Dr. Adam Hall for your wisdom and exemplary persistence and to Dr. Lucile Teague for your constancy and tenacious friendship.

Thanks to Kwan Skinner for helpful discussions and for tailoring the fabrication of the nanorods to meet my experimental needs. Thanks to Jeremy Cribb for his valuable assistance in the design of many of the magnetophoresis experiments and in guiding me through my initial forays into polymer physics.

Special thanks to Dr. Jennifer Weinberg-Wolf and Dr. Eric Harley for their eagerness to help me by taking the spatially resolved Raman data, and to Dr. Luarie McNeil for the use of the Raman facility. I am grateful for the assistance provide by Dr. Liang He and Dr. Frank Tsui in making SQUID susceptometry measurements of the particles used in these investigations.

I would like to acknowledge the support of the National Science Foundation (NSF) and the National Institutes of Health (NIH) for the funding of my research at UNC. I would also like to acknowledge the support of the NSF for supporting me through the East Asia and Pacific Summer Institutes (EAPSI) fellowship. Thanks to Dr. Kevin Jack of the University of Queensland, Australia for mentoring me during my EAPSI fellowship and to Dr. Matt Trau for hosting me in his lab.

Dedicated in loving memory of my grandparents, Warren Nameska (1918-1996) and Gladys Lentz (1925-2005).

Table of Contents

List of Symbols

a, r	radius
B	magnetic induction
E	electric field
χ_m	mass susceptibility
χ_v	volumetric susceptibility
ε	dielectric constant
η	viscosity
F	force
γ	drag coefficient
$\dot{\gamma}$	maximum shear rate
$\tilde{\gamma}$	geometric component of drag coefficient
H	magnetic field
I	current
k	Boltzman constant
K	Clausius-Mossotti factor
L	length
M	magnetization
m	magnetic moment
m	mass
$m_{\perp}$	saturating magnetic field applied perpendicular to major axis
$m_{\|\|}$	saturating magnetic field applied parallel to major axis
μ_0	permitivity of free space
μ_{eo}	electroosmotic mobility

R_e	Reynolds number
ρ	density
ρ	distance from wire axis to line path
σ	mass magnetization
σ	standard deviation
T	temperature Kelvin
τ	time constant at where 1/τ is the critical shear at which viscosity begins to decrease
U	energy
V	volume
v	velocity
v_{eo}	velocity of electroosmotic flow
ζ	zeta potential

CHAPTER ONE: Magnetic Materials and Magnetophoresis

This chapter will serve to introduce the reader to some of the basic principles of magnetics and magnetic force which will be necessary for understanding the later research investigations. This chapter will also provide a historical context for considering magnetic manipulation techniques by comparison with traditional separation methods such as electrophoresis and cell sorting. The fundamentals of magnetics will be introduced first followed by the comparison of magnetic manipulation with other separation applications. The more lengthy mathematical descriptions of the principles which are introduced in this chapter are included in the appendices to provide the reader with the basic equations which will be utilized through out the later chapters.

Physical Considerations of Magnetophoresis

Magnetophoresis

The term magnetophoresis is used to describe the movement or separation of magnetic particles from non-magnetic ones.[1] The applications of magnetophoresis cover a range of scales from bulk separations to high precision analytical isolation. Magnetophoresis has been used for some time in the mineralogical industries as a means for bulk separation of ore and has more recently become a commercialized method for separating biological material.[2, 3]

The following discussions of the physical origin of magnetic force and the mathematical description of the parameters which result in the movement of magnetized particles will enable an understanding of the research investigations which were undertaken. The historical examples of the evolution of magnetophoretic technology, the advantages over competitive methods of particle transportation, and the outlook for new and developing magnetophoretic applications will help to give a context to the following discussions of this research investigation.

The study of magnetic phenomena routinely utilizes both centimeter gram second (cgs) and International Standard (SI) unit systems. There also exists a lack of uniformity in the nomenclature and notation within the field. Therefore in order to aid the reader, a table of the most relevant magnetic parameters in cgs and SI units has been set out in table 1.1. The notations in this table will be utilized for the remainder of this document.

Introduction to Magnetic Materials

While fundamental principles of magnetization based in quantum physics are outside the scope of this investigation, an introduction to the basic concepts of magnetic materials is appropriate. Magnetic fields result from moving charge. In an atom the spins of electrons produces a magnetic field which results in individual dipoles. The magnetization of a material is thus due to the magnetic moments of individual atoms. When a material is placed in a magnetic field the orientations of the individual dipole moments are changed. The extent of this magnetization is specific to the strength of the applied field and to the characteristics of the material. Materials which are composed of elements having a large number of unpaired spins generally exhibit greater magnetic behaviour.[4]

Materials are generally categorized as diamagnetic, paramagnetic, antiferromagnetic, ferrimagnetic, or ferromagnetic based on their magnetic characteristics. The most relevant of these categories in this discussion are diamagnetic, paramagnetic, and ferromagnetic. Many materials exhibit properties of multiple categories. All materials, for example, show a diamagnetic response to an applied field which results in a weakly repulsive force. If the material demonstrates any other magnetic response however the weak diamagnetic behavior will be easily offset.[5]

Ferromagnetic Materials

Ferromagnetic materials are frequently referred to as *magnetic* in that a majority of the dipoles have been permanently oriented parallel after the initial application of a magnetic field. A ferromagnetic material maintains the resulting net dipole moment after the external field is removed. This residual magnetization of the material after the removal of the externally applied field is known as the remanent magnetization. After the application of a magnetizing field, the individual dipoles in ferromagnetic material will remain mutually aligned unless significant energy is put into the material such that the dipoles become randomized, and the material is thus demagnetized.[6] This energy input which de-magnetizes a material may come in several forms such as heat, physical vibration, or the application of a demagnetizing magnetic field. The intentional application of an external magnetic field in order to reduce the remanent magnetization is know as *degaussing*.

Paramagnetic Materials

Unlike a ferromagnetic material, the dipoles of a paramagnetic substance are not ordered without the application of a magnetic field and the material maintains no net magnetic dipole. When a magnetic field is applied to a paramagnetic material, the individual dipoles will align parallel to the field and result in the material acquiring a net dipole moment which is also aligned parallel to the field. When the external magnetic field is removed however the dipoles will relax to a randomized orientation and the material will cease to be magnetized.[7]

Characterization of Magnetic Materials

The magnetic properties of a material are characterized by measuring the magnetization of a sample induced by an external applied field. When the sample magnetization is measured in response to an applied field which is cycled positive and negative, a cyclic hysteresis curve is obtained. A great number of magnetic characteristics of a sample such as the remanent magnetization, susceptibility, and saturation may be gleaned from a hysteresis curve. The essential magnetic characteristics will be briefly discussed to introduce the reader to the fundamental properties of magnetic materials.[8] A simulated hysteresis curve typical of a ferromagnetic sample is presented in figure 1.1 with some of the common magnetic characteristics of a material indicated.

The magnetization response of a material to the application of a magnetizing field H is described by the magnetic susceptibility of the material χ. The maximum magnetization that a material may attain is the saturation magnetization M_{sat}. A material at saturation has the maximum number of dipoles oriented parallel and the application of greater field does not result in a commensurate increase in the magnetization of the material. A material will therefore exhibit a linear magnetization response to an applied field until it approaches the saturation magnetization at which point the magnetization as a function of the applied field will plateau as shown in figure 1.1.[5]

Magnetic Force

A magnetized body in a non-homogeneous magnetic field will experience a force in the direction of increasing field strength. The difference between the susceptibility of a particle in a medium, and the susceptibility of that medium is monotonically related to the magnitude of the magnetic driving force applied to the particle.[9] It is helpful in understanding the origins of magnetic force to proceed through a mathematical description of the relevant properties and their relationships. The derivation of magnetic force in practical quantities has been set out in appendix 1 to aid the reader.

An equation of practical utility for describing the magnetophoretic force on particles in the experiments described here is derived in appendix 1 and also shown in equation 1.0. This equation is a useful approximation for describing the magnetic force ($\vec{F}$) on a particle where the susceptibility of the particle is much greater than that of the medium. The formal expression for magnetic force can be found in appendix 1. In equation 1.0, V is the volume of the magnetic material, χ is the volumetric susceptibility of the material, μ_0 is the permeability of free space (a constant), and $\vec{\nabla}B^2$ is the product of the magnetic field (B) and the magnetic field gradient (∇B).

$$\vec{F} = \frac{1}{2}\frac{V\chi}{\mu_0}\vec{\nabla}B^2 \qquad \text{Equation 1.0}$$

A table of relevant magnetic properties has been set out in table a1.0 in appendix 1 to aid the reader.

It is evident from equation 1.0 that the force which can be applied to a magnetic particle is dependent on the susceptibility of the material and the volume of the particle according to ($F \propto \chi V$) for small χ. Even for a material with a relatively high susceptibility, such as magnetite (Fe_3O_4), the small volume of a microparticle makes the application of large forces a challenge. In order to controllably manipulate small particles, forces larger than those due to thermal (Brownian) motion must be applied. Described in terms of energy requirements, the potential energy of a particle (U) with magnetic moment (m) in a field (B) must be larger than thermal energy as summarized in equation 1.1, where k is the Boltzman constant and T is degrees Kelvin.

$$|U| = m \bullet B = -\frac{\chi B^2 V}{\mu_o} \gg {}^{3}\!/_{2}\, kT \qquad \text{Equation 1.1}$$

Brownian motion resulting from thermal energy represents a fundamental constraint on the applied force requirements for the magnetophoretic manipulation of particles.

Practical Considerations in Magnetophoresis

Reynolds Number

Many common examples of magnetophoresis, and all the examples presented here, involve the transportation of particles in a fluid medium. It is helpful in discussing the magnetically driven mobility of particles in a fluid to consider the system in terms of its *Reynolds number* (R_e). The Reynolds number describes the ratio of the inertial forces to the viscous resistance forces in the system. This ratio is expressed in equation 1.2 where the inertial force is the product of the fluid density (ρ), the mean fluid velocity (v_s), and the characteristic length (L). The viscous force is characterized in the equation by the fluid viscosity (η) in units of Pa sec.[10]

$$\mathrm{R_e} = \frac{\rho v_s L}{\eta} \qquad \text{Equation 1.2}$$

The inertia of a magnetically driven micro-particle in water is typically much smaller than the viscous drag force on the particle due to the low mass of the particle relative to the viscosity of medium. In such a low Reynolds number system, the magnetically driven particle attains terminal velocity very quickly. This has the effect of the instantaneous velocity of a particle being approximately proportional to the applied force at that instant.[11]

Viscous Drag

According to Stokes' Law, the drag force of a particle in a viscous medium is determined by the velocity of the particle (v) and the geometric drag coefficient (γ), which includes the viscosity of the medium, as expressed through equation 1.3.[12]

$$F = -\gamma v \qquad \text{Equation 1.3}$$

This relationship is generally applicable for small objects moving through a viscous fluid at relatively slow speeds such as will be encountered in this investigation.

When a driving force is applied to a particle in a low Reynolds number system the particle travels with a constant velocity as previously mentioned. When the driving force is removed the particle stops essentially instantly.[11] Equating the drag force with the driving force according to equation 1.4 is therefore a reasonable practical assumption.

$$\left|F_{drag}\right| = \left|F_{driving}\right|, \left|\gamma v\right| = \left|\mathrm{m}a\right| \qquad \text{Equation 1.4}$$

The equating of the drag and magnetic driving forces on a bead in water is a practical example of this relationship as illustrated by equation 1.4, where η is the viscosity of the medium, *a* is the radius of the bead, and *v* is the particle velocity. The right side of equation 1.4 is simply the equation for magnetic force (equation 1.0).

$$6\pi\eta a v^{[13]} = {}^{1}\!/_{2}\,\frac{V\chi}{\mu_0}\vec{\nabla}B^2 \tag*{Equation 1.4}$$

The drag coefficients have been calculated in the literature for many simple particle geometries, and can be estimated for more complex shapes.[13] The assumption of terminal velocity due to low Reynolds number conditions provides a convenient method for determining the driving force on a particle by simply measuring the velocity of the particle, provided that the dimensions of the particle and the medium's viscosity are known. This technique of determining the forces on a driven particle based on the dimensions of the particle, the viscosity of the medium, and the velocity of the particle is known as *velocitometry* and will be used throughout this investigation.

Magnetophoresis and Competitive Techniques

The remainder of the chapter will describe some traditional separation and particle manipulation techniques which can be utilized for similar purposes as magnetophoresis. The purpose of the comparison is to provide a context for the reader to consider magnetophoretic techniques in terms of current technology, and to illustrate the differences between magnetophoresis and these competitive methods. Some of the examples of magnetophoretic applications are analytical in nature. While *analytical* magnetophoresis is not the primary focus of this thesis, the methodology of quantifying the magnetic characteristics of the complete magnetophoretic system, including the particles and the applied field, utilized here has direct relevance to the design of analytical magnetophoretic systems.

Industrial Applications of Magnetophoresis

The idea of being able to separate small magnetic particles from a bulk matrix via high gradient magnetic separation (HGMS) was first proposed by researchers looking for the Dirac monopole on the sea floor in the 1930's.[14] Since then, HGMS systems have become common in minerals beneficiation and pollution control. These systems often have field strengths of 300 A/m and gradients as great as 3 $x10^6$ A/m^2. HGMS are used in the clay industry to remove microscopic weakly magnetic impurities. As well as being used to control the emissions of coal power plants through desulphurization and de-ashing. By seeding polluted water with microscopic iron oxide particles functionalized to bind contaminants, water purification has been achieved.[15] Ferrography is another niche of magnetophoretic separation which is used industrially to determine machine wear. Wear particles in lubricating oil are magnetically separated and examined with optical microscopy in order to assess wear on machine parts.[16]

Biological Applications of Magnetophoresis

The use of magnetophoresis to separate cell types based upon the differences in their susceptibilities has generated much enthusiasm in the biological sciences. However, since most cells consist primarily of water their susceptibility differs little from their surrounding aqueous medium resulting in only a weak magnetophoretic force. While magnetophoresis has been used in mineralogy and mining for bulk separations, the necessity for specific labelling prior to magnetophoretic separation represents a significant barrier to its use as an analytical technique. There are two exceptions to this generality however, erythrocytes (red blood cells) and magnetotactic bacteria have been isolated without magnetic labelling.[17-20]

In the deoxygenated form hemoglobin is paramagnetic enabling erythrocytes to be isolated by magnetophoresis. Magnetotactic bacteria have paramagnetic iron nanoparticles which allow them to navigate along geomagnetic field lines.[21] The inherent susceptibilities of erythrocytes and magnetotactic bacteria allow them to be separated without any additional magnetic labelling.[22, 23] Magnetophoretic separation of other cell types however requires specific magnetic labelling to increase the overall susceptibility and permit magnetophoretic separation. This is largely why magnetophoresis has failed to be competitive with flow cytometry for cell isolation in terms of specificity or throughput.

Magnetophoretic Cell Separation

There are several commercially available magnetophoretic cell separation systems.[24-26] In general these traditional magnetic separators subject a suspension of paramagnetic or magnetically labelled cells to a magnetic field gradient which is produced by a particular geometric arrangement of rare earth permanent magnets which results in a high gradient. Many of the early magnetophoresis systems achieved high field gradients by incorporating steel wool directly in to the flow tube. External permanent magnets magnetized the mesh which in turn produced the field gradients.[27] Today, high field gradients are often realized by surrounding a capillary with a quadrupole magnetic geometry similar to the quadrupole electrodes found in some mass spectrometers.[28] The cells are typically labelled by the attachment of magnetic beads or nanoparticles which have been functionalized with monoclonal antibodies specific to an antigen expressed on the cell.[29]

Ferritin as a Magnetic Label

One of the earliest reports of magnetic labelling of cells for separation was by Owen et al in 1979. This was performed by allowing T cells to form rosettes with paramagnetic sheep red blood cells.[30] The first report of specifically labelling individual cells for magnetic manipulation however was by Odette and coworkers in 1984.[31] Odette used the iron containing protein ferritin to magnetically label rat erythrocytes in order to increase their susceptibility. Since this initial demonstration of ferritin as a magnetic label there have been several seminal reports which further support its utility.[32, 33] Because it is water soluble and non-cytotoxic, ferritin can be used conveniently and safely to label living cells.[34]

Characteristics of Ferritin

Ferritin is well studied and has been used as a high contrast label for biological samples in electron microscopy imaging for decades and it is widely distributed among animals, plants, and microbes. The reason for the broad distribution of ferritin across many kingdoms is because of the physiological necessity of iron. High levels of extracellular iron can be toxic however and therefore biological iron stores are maintained as a hydrous ferric oxide nanoparticle inside a spherical protein shell. The protein has 24 subunits and is 12 nm in diameter. The iron core is between 6-8 nm in diameter and may contain as many as 4500 iron atoms.[35]

The first study of the magnetic properties of ferritin was by Michaelis et al in 1943.[36] Due to the small size of the iron core, it was predicted to be superparamagnetic at room temperature. It was determined that the susceptibility was in fact independent from the applied magnetic field and therefore ferritin was completely paramagnetic without any ferromagnetic character. It was also found that the slight diamagnetic property of the protein shell was negligible and that the iron core was the sole contributor to the susceptibility. The researchers used a combination of two techniques to study the properties of ferritin. The macromethod[37] determined the amount of force on ferritin while in a magnetic field in terms of the weight. The micromethod[38] measured the magnetic pull in terms of the deflection of a pointer of a magnetically damped semi-micro balance. The small size, availability, and unique magnetic characteristics of ferritin made it immediately attractive as a magnetic label.

Separation Techniques Competitive with Magnetophoresis

It is helpful in the discussion of magnetophoresis and its applications to compare it with the more familiar phenomena of electrophoresis and dielectrophoresis (DEP). It is likewise useful to compare magnetophoretic cell sorting with the traditional technique of flow cytometry. For simplicity the term *particle* will be used broadly to describe any microscale, nanoscale, or molecular bodies.

Field Induced Separations

Electrophoresis, DEP, and magnetophoresis involve the manipulation of particles through the application of a force which results from an applied field. Electrophoresis is the migration of electrically charged particles due to an electric field, while DEP is the movement of an electrically polarized body due to an electric field gradient. Magnetophoresis is similar to DEP in that it describes the migration of a magnetically polarized (magnetic dipole) due to an applied magnetic field gradient.[9]

The mobility of a polarizable or magnetizable particle in a medium with an imposed electric or magnetic field gradient can be described in similar ways. In both circumstances the mobility is a function of the polarization or magnetization of the particle with respect to the medium. If the polarization or magnetization of the medium is less than that of the particle then the particle will experience a net force toward the high field strength. The *Clausius-Mossotti function* (K) is a convenient means for determining the effective polarization or magnetization of a particle in a medium. A mathematical description of the comparison of the electric polarization of a particle in an electric field with a magnetically polarized particle in a magnetic field can be found in appendix 2. Table a2.0 in the appendix summarizes the particle mobilities and forces associated with electric and magnetic fields.[9] The following brief descriptions of electrophoretic techniques will prepare the reader for the subsequent comparison of electrophoresis and magnetophoresis.

Electrophoresis

Electrophoresis has been widely used as a separations tool by a variety of disciplines for decades while magnetophoresis is still in its infancy as a quantitative separation technology. Electrophoresis is most widely used in biological sciences because of the complex mixtures of compounds routinely encountered in biochemistry.[39] Gel electrophoresis has been a mainstay of protein separation for decades. Gel electrophoresis uses a polymer which is swollen with buffer as the separation medium. A voltage is applied across the gel and the ions migrate according to their electrophoretic mobilities. The polymer matrix acts as a molecular sieve causing larger molecules to become entangled and slowed down relative to smaller molecules which easily pass through the polymer network. A variety of different linear and cross-linked polymers are used, such as polyacrylamide, polyethylene glycol, and agarose. The specific polymer matrix can be selected based upon particular analyte considerations. [40]

Traditional gel electrophoresis requires the use of relatively large quantities of analyte. The development of capillary electrophoresis (CE) in the 1980s, which required a much smaller quantity of material for analysis, led to an explosion in the isolation and identification of biochemicals.[41] It is hard to envision the existence of fields such as proteomics, and genetics without capillary electrophoresis. While the analyte of electrophoretic separations is most often a molecule, there is work involving electrophoresis of particles including bacteria and cells.[42]

Capillary Electrophoresis

Capillary electrophoresis is typically performed inside a fused silica capillary. The surface of silica is composed of silanol groups which exist as SiO^- at pH higher than 2. This dictates a net negative charge to the inner surface of a capillary and results in the electrostatic attraction of positive ions from the buffer. When the electric field is applied to the buffer the adsorbed positive ions will migrate toward the negative electrode carrying the waters of hydration along with them. This results in a net flow near the walls of the capillary known as electroosmotic flow (EOF). The velocity of the EOF (v_{eo}) is defined by the product of the electroosmotic mobility (μ_{eo}) and the electric field (E) as expressed by equation 1.5.[43]

$$v_{eo} = \mu_{eo} E \qquad \text{Equation 1.5}$$

The double layer formed by the negatively charged silica and the layer of counter ions produces an electric potential known as the zeta potential (ζ). The electroosmotic mobility is proportional to the zeta potential and the dielectric constant (ε) of the media, while inversely proportional to the viscosity of the media (η) as shown in equation 1.6.

$$\mu_{eo} = \frac{\varepsilon\zeta}{4\pi\eta} \qquad \text{Equation 1.6}$$

The EOF produces a flow velocity gradient across the capillary which can decrease the resolution of the separation.[44] Since a magnetic field does not interact with charged species, electroosmosis does not represent a limiting parameter in magnetophoretic separations and manipulations.

Joule heat is caused by the resistance of the mobile phase and the current passed as a result of the high voltages applied in electrophoresis. The heat is more readily dissipated by the small capillaries used in CE than in the slabs used in traditional gel electrophoresis and voltages in the tens of kilovolts are routinely used in CE. Joule heating results in convective flow within the column and serves to decrease the resolution of a separation. [43] In DC magnetophoresis manipulations, the sample is not heated as it is by the resistance affects in electrophoresis. The lack of Joule heating initiated convection which can disturb the sample and limit separation efficiency is therefore avoided in magnetophoretic methods.

A number of variable elution parameters are accessible in electrophoresis that are fundamentally unavailable in magnetophoresis. By manipulating these parameters a variety of specific separation modes have been developed for CE. Capillary zone electrophoresis (CZE) is the simplest form and relies solely on the electrophoretic mobility of the ions for separation. Micellar electrokinetic capillary chromatography (MECC) adds the partitioning of analyte into micelles as an additional variable in CE.[45]

Capillary gel electrophoresis incorporates a polymeric matrix typical in traditional gel electrophoresis in a capillary. This adds the benefits of decreasing diffusion and decreasing EOF by increasing the viscosity of the medium. These effects serve to increase the resolution of the separation. Isoelectric focusing (IEF) uses a pH gradient to focus the analyte according to its isoelectric point (pI). The charged analyte will migrate until it reaches a region where the pH is such that the ion has an equal number of positive and negative charges. When it has reached its pI it will no longer possess a net charge and will have no electrophoretic mobility. If the molecule diffuses away from this region it will regain a net charge and be refocused back to the area of its pI.[43]

The force on an ion during electrophoresis is defined as $F_E = qE$, where the force is directly proportional to the charge (q) on the ion and the magnitude of the electric field (E). [43] The relationships between the force and the imposed field for dielectrophoretic and magnetophoretic force are significantly more complicated and will be derived later. Under most circumstances an inherent assumption of the equations is that the particle is unaffected by other particles. This is generally valid under conditions of low particle concentration where the distance separating particles is significant and fields from particle dipoles are weak, such that particle-particle interactions can be ignored.

Comparing Electrophoresis with Magnetophoresis

Commercial electrophoresis instrumentation is available for a multitude of specific applications. While the practicality of magnetophoretic separations of biological material has rapidly gained acceptance in recent years, the level of sophistication of the separations remain relatively low. Because biological macromolecules (proteins, oligonucleotides, peptides) are large molecules with multiple charged groups, they are particularly well suited for electrophoretic separation.[46] The inherent characteristics of an analyte dictate its electrophoretic mobility. However, the magnetophoretic separation of an analyte from a mixture relies of the ability to specifically label the desired species with a magnetic particle.

The signal to noise ratio (S/N) of magnetophoretic separation is directly tied to the specificity with which a particular analyte can be labelled. Therefore, the efficacy of magnetophoresis depends on knowledge of the attachment chemistry of the magnetic label. If there are multiple constituents that may be labelled by a magnetic particle, then the ability to isolate a particular one will be diminished and the S/N will decrease due to interferants. Zborowski et al have addressed this challenge through the use of cationic ferritin as a label for the isolation of lymphocytes from whole blood. While the researchers report that 95% of the cells which were separated were lymphocytes, monocytes and neutrophils were also present.[1]

The numbers of magnetic particles which are attached to an analyte in part determine its magnetophoretic mobility. Under most circumstance the magnetic label would need to be removed from a magnetophoretically isolated target once the separation was complete. This hurdle adds extra technical complexity to magnetophoresis over electrophoresis as well as increasing the number of steps, and consequently the time and cost necessary to conduct a separation. Non-homogeneous labelling of an analyte represents a potential source of decreased resolution. Given a population of cells which are magnetically labelled, for example, a distribution of labelling will occur; some will be labelled more than others. The entire population will not have the same mobility and some will be separated more readily than others.[33] In addition to magnetophoresis, flow cytometry is widely used for separating cells and other microscale particles. The following brief description of the technique will enable comparison between flow cytometry and magnetophoretic separations.

Flow Cytometric Separations

Flow cytometry allows for the identification of specific cell populations in a bulk specimen by individually interrogating cells. Fluorescently tagged antibodies are used to specifically label cellular substrates which correlate to a certain cell type. The combination of excitation of a fluorophore label and light scattering enables the identification of cell type according to size and the fluorescent response. The cells pass through an excitation source (typically a laser) where the fluorescence and light scattering of the cell are detected. These data allow for the identification of the number of cells which fit specific fluorescence and size criteria, and thus for the identification of the cell type.[47]

Flow cytometry has been incorporated in cell sorting which serves to not only identify cell types but also to separate (sort) the cells. The first fluorescence activated cell sorter (FACS) was developed by Herzenberg et al and published in 1972.[48] The system has not fundamentally changed since the instrument was first introduced. Modern instrumentation often utilize multiple lasers for excitation of up to 12 different fluorophores and has dramatically increased throughput (10^4 cells/s)[49] over the early instruments.

A cell suspension is specifically labelled with fluorophores and intracellular dyes which will serve to identify particular cell types. The cells are ejected from a nozzle one by one while being maintained in a single file line hydrodynamically by a sheath fluid. An oscillator vibrates the stream at kilohertz frequencies which separates the stream into discrete droplets, a technique which was originally developed for ink-jet printing. Only a small percentage of the drops contain a cell. A laser is directed on the stream just prior to it being separated into droplets. As each cell passes through the laser a signal is recorded on a photodetector for fluorescence and light scatter which allows individual cells to be identified according to fluorescence parameters and size.[50]

If either the correct size or fluorescence criteria are met, the droplet is given an electric charge; either positive or negative. As the drop falls it passes between two charged plates which deflect the drop according to the charge it has been given. Drops which did not meet the set fluorescence or size criteria are uncharged and are not deflected. The deflection of the drops adjusts their trajectory and deposits them into their appropriate collection receptacle.[51]

The large number of cells which can be interrogated in a short time allows for the identification of rare cell types to be identified and isolated from a bulk specimen. The early detection of particular cell types is fundamental in diagnosis of a variety of diseases. FACS provides a means to determine the ratio of a particular cell type in a sample. This technique is routinely used to identify malignant cells, T cells and B cells. In addition to the identification and quantification of a particular cell type, FACS serve to concentrate a sample according to cell type.[47]

Current magnetophoretic methods can not compete with the combination of high-throughput and resolution offered by modern flow cytometric instrumentation. The size and cost of flow cytometry instrumentation requires significant investment in facilities which places limits on the broad application of flow cytometry to many point-of-care, low-tech and field based analyses. The recent drive for smaller and less expensive analytical devices has created a niche which gives magnetophoresis potential advantages over flow cytometry.

MicroMagnetophoresis

Lab-on-a-chip (LOC), or micro total analytical system (μTAS), devices have miniaturized many of the reaction, separation, and analysis techniques previously performed by researchers at the bench. μTAS devices hold the promise of fast, inexpensive, disposable analysis systems with multiple tests and separations being carried out in parallel on the same chip. As a result, efforts have been made to reduce the scale of the instrumentation used in magnetophoresis. Advances in the commercialization of micro-scale magnetic beads are aiding the development of systems which perform magnetophoretic manipulation at the micro-scale. While designs are being pursued which dramatically decrease the size of the instrumentation necessary for FACS, to date there have been few reports of microfluidic FACS.[52] The ability to scale down magnetophoretic systems represents a significant advantage over flow cytometry.

Current commercially available magnetophoresis instruments require large permanent or electromagnets in order to apply significant forces to isolate magnetically labelled cells or analyte.[24, 25, 53] These commercial systems are useful for bulk separations but lack the ability to manipulate individual particles and beads. Because of the physical size of the magnets used in these commercial systems, it is difficult to obtain the high field gradients at the small scales which are necessary for micromanipulation.

A magnetophoretic μTAS design allows for localized high field gradients through the miniaturization of the magnetics and by the placement in close proximity to the particles to be manipulated. Although applying high forces to particles with magnetic systems small enough to fit on a chip presents a real challenge, it has been shown that it is possible to apply fields large enough to manipulate or separate individual microscopic particles.[54] Some LOC magnetophoresis devices have been designed for simple separation, cell sorting[55-57], while others have sought to manipulate individual cells and particles.[58-60]

Introduction to Electromagnetic Micromagnetophoresis

Many microfluidic magnetophoresis devices utilize current carrying wires in order to generate magnetic fields. Traditional lithographic techniques, such as are used in the production of printed circuit boards, can be used to fabricate micron size wires on flat substrates which can be sealed to microfluidics channels. Wires produced in this manner can easily be made to any geometry and from dimensions of tens of nanometers to tens of microns. The designs are generally inexpensive and amenable to mass production. The magnetic fields which can be produced by current carrying wires are often small compared to those of permanent magnets however.

The magnetic field (*B*) produced by the current in a wire (*I*) can be described by the line integral with respect to *dl* shown in equation 1.7.

$$\oint B dl = \mu_o I \qquad \text{Equation 1.7}$$

For an infinitely long cylindrical wire, *dl* can be integrated along a circular path which encloses the wire as shown in equation 1.8, where ρ is equal to the distance from the axis (center) of the wire to the line path enclosing the wire and $l = 2\pi\rho$.

$$B = \frac{\mu_o I}{2\pi\rho} \qquad \text{Equation 1.8}$$

The gradient of *B* would then simply be the derivative of *B* with respect to ρ as shown in equation 1.9.

$$\nabla B = \frac{\mu_o I}{2\pi\rho^2} \qquad \text{Equation 1.9}$$

Equations 1.10 and 1.11 follow from the force proportionality of a magnetizable particle in a magnetic field gradient.

$$\nabla B^2 = \frac{\mu_o{}^2 I^2}{4\pi^2\rho^3} = \frac{-\mu_o{}^2 I^2}{2\pi^2\rho^3} \Rightarrow (12 \cdot 10^{-7}\, {}^{T}\!/_{m \cdot A}) \frac{I^2}{\rho^3} \qquad \text{Equation 1.10}$$

$$Force \propto \frac{I^2}{\rho^3} \qquad \text{Equation 1.11}$$

It can be seen from equation 1.11 that the magnetic force which can be applied using this type of magnetic system is proportional to the square of the current carried by the wires. The passage of currents large enough to apply the necessary magnetic field for an effective separation may pose significant challenges. Thermal energy in the devices produced by resistive heating can lead to degradation or failure of the devices. Resistive heating may also contribute to thermal convection which can decrease the efficiency of the seapartion.

Electromagnetic MicroMagnetophoretic Devices

Westervelt has demonstrated the ability to use a simple lithographically fabricated current loop as a magnetophoretic trap. A 2.7 T magnetic field was produced with the passage of 0.35 A through the ten micron wide wire loop.[61] The current loop was used to magnetophoretically trap magnetically labelled yeast cells, and magnetotactic bacteria.[58] The researchers also developed a waffle shaped, two dimensional electromagnetophoretic manipulator which has been incorporated into a microfluidics design.[59] Two sets of parallel micron size wires in two electrically isolated planes are oriented perpendicular to each other. By passing current along adjacent wires top and bottom a localized high field gradient is created. By alternating which wires are electrified they were able to manipulate paramagnetic nanoparticles[61] and magnetic beads.[58]

Boeck and co-workers have also used the magnetic field produced by current carrying wires to manipulate magnetic beads. Their system incorporates a unique saw-toothed electrode design in order to produce a magnetic field that varies with the width of the electrode.[56] The co-planar electrode orientation has the two electrodes arranged parallel with the flat edges facing together and off set by half a period. This produces a forward zig-zag movement of the bead. The stacked conductor design overlays two offset electrodes which are separated by an insulating layer of polyimide. By energizing the upper and lower electrodes alternatively the beads travel along a linear path.

Another design which utilizes a wire geometry in order to produce alternating high field localizations is presented by Whitesides' laboratory.[62] Parallel castellated (serpentine) wires which are offset out of phase from each other produce a magnetic field track for beads to follow. By alternating current in one wire then the other the beads are pulled from a high field region on one wire to an adjacent high field region on the other wire. An external field produced by a permanent magnet amplifies the effect of the current in order to produce fields large enough to effectively trap the beads. The wires were fabricated by soft-lithography and electroplating with gold and had dimensions of 50-100 μm wide and 10-20 μm high. Values for the field and field gradients produced by this system are not reported although the researchers state that 3 A was sufficient to trap the 4.5 μm Dynal beads.

Summary

The focus of this thesis is not the physics of magnet fields and as such the principles of magnetics and magnetophoresis which have been briefly described in this chapter will be sufficient to furnish the reader with the basics concepts necessary for understanding the following research chapters. There are significant challenges to magnetophoresis as a technique competitive with other methods of separation as has been illustrated by the comparison with traditional techniques. However magnetophoresis also has unique advantages over these traditional separation techniques which are leading to its increased use in a range of analytical and medical applications.[63-65]

Figures

Figure 1.1

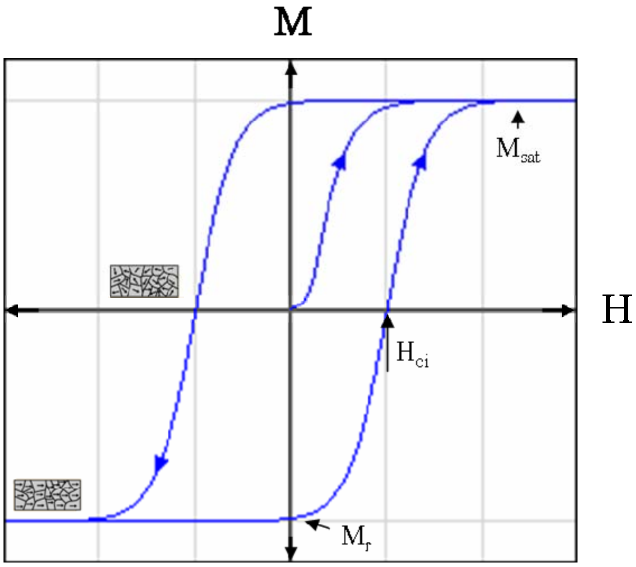

This figure presents a typical hysteresis curve of a ferromagnetic sample. M is the magnetization of the sample as a function of the applied field H. M_{sat} is the saturation magnetization, M_r is the remanent magnetization, and H_{ci} is the coercivity. Upper and lower cartoon insets represent the orientation of the magnetic dipoles in the material at zero magnetization and at saturation respectively.[66]

Table 1.1

Term	**Symbol**	**SI unit**	**CGS unit**	**Conversion Factor**
Magnetic Induction	B	Tesla (T)	Gauss (G)	1 T = 10^4 G
Magnetic Field	H	A/m	Oersted (Oe)	1 A/m = $4\pi/10^3$ Oe
Magnetization	M	A/m	emu/cm^3	1 A/m = 10^{-3} emu/cm^3
Mass Magnetization	σ	Am^2/kg	emu/g	1 Am^2/kg = 1 emu/g
Magnetic Moment	m	Am^2	emu	1 Am^2 = 10^3 emu
Magnetic/Volumetric Susceptibility	χ_v	Dimensionless	Dimensionless	4π (SI) = 1 (cgs)
Mass Susceptibility	χ_v/ρ, χ_m	m^3/kg	emu/Oe g	1 m^3/kg = $10^3/4\pi$ emu/Oe g
Permeability of Free Space	μ_o	H/m	Dimensionless	$4\pi 10^{-7}$ Tm/A, H/m = 1 (cgs)

This table summarizes some of the magnetic properties most relevant to this investigation in cgs and SI units.

References

1. Zborowski, M., et al., *Analytical Magnetapheresis of Ferritin-Labeled Lymphocytes.* Analytical Chemistry, 1995. **67**(20): p. 3702-3712.

2. Assi, F., et al., *Massively parallel adhesion and reactivity measurements using simple and inexpensive magnetic tweezers.* Journal of Applied Physics, 2002. **92**(9): p. 5584-5586.

3. Amblard, F., et al., *A magnetic manipulator for studying local rheology and micromechanical properties of biological systems.* Review of Scientific Instruments, 1996. **67**(3): p. 818-827.

4. Schlenker, M., *Magnetism: Fundamentals*, ed. E. du Tremolet de Lacheisserie. 2003, New York, NY.

5. Morrish, A.H., *The Physical Principles of Magnetism*. 2001, New York, NY: IEEE.

6. Wohlfarth, E.P., *Ferromagnetic materials : a handbook on the properties of magnetically ordered substances*. 1995, Amsterdam: Elsevier North-Holland.

7. Johnson, H.R., *Discovering magnetism* 2006, Santa Barbara, CA: Cheniere Press.

8. Zhu, Y., *Modern Techniques for Characterizing Magnetic Materials*. 2005, New York, NY: Kluwer Academic Publishers.

9. Jones, T.B., *Electromechanics of Particles*. 1995, Cambridge: Cambridge University Press.

10. Happel, J.A.B., Howard, *Low Reynolds number hydrodynamics : With special applications to particulate media* 1973: Noordhoff International Publishing.

11. Berg, H.C., *Random Walks in Biology*. 1993, Princeton, NJ: Princeton University Press.

12. Halliday, D., *Fundamentals of physics* 2007, Hoboken, NJ.

13. Howard, J., *Mechanics of Motor Proteins and the Cytoskeleton*. 2001, Sunderland, MA: Sinauer.

14. Kolm, H., *Search for Magnetic Monopoles.* Phys Rev D, 1971. **4**(5): p. 1285-1296.

15. Oberteuffer, J., *High Gradient Magnetic Separation.* Ieee Transactions on Magnetics, 1973. **9**(3): p. 303-306.

16. Scott, D., *The Particles of Wear.* Scientific America, 1974. **230**: p. 88-97.

17. Zborowski, M., et al., *Red blood cell magnetophoresis.* Biophysical Journal, 2003. **84**(4): p. 2638-2645.

18. Watarai, H. and M. Namba, *Capillary magnetophoresis of human blood cells and their magnetophoretic trapping in a flow system.* Journal of Chromatography A, 2002. **961**(1): p. 3-8.

19. Denham, C.R., R.P. Blakemore, and R.B. Frankel, *Bulk Magnetic-Properties of Magnetotactic Bacteria.* Ieee Transactions on Magnetics, 1980. **16**(5): p. 1006-1007.

20. Blakemore, R., *Magnetotactic Bacteria.* Science, 1975. **190**(4212): p. 377-379.

21. Lins de Barros, H.G., D.M. Esquivel, and M. Farina, *Magnetotaxis.* Sci Prog, 1990. **74**(295 Pt 3): p. 347-59.

22. Chikov, V., et al., *Single-Cell Magnetophoresis and Its Diagnostic-Value.* Journal of Magnetism and Magnetic Materials, 1993. **122**(1-3): p. 367-370.

23. Bahaj, A.S., P.A.B. James, and F.D. Moeschler, *High gradient magnetic separation of motile and non-motile magnetotactic bacteria.* Ieee Transactions on Magnetics, 1996. **32**(5): p. 5106-5108.

24. Dynal, B., www.dynal.no. Brown Deer WI.

25. Miltenyi Biotec, I. Auburn CA.

26. Chemicell. *12103 Berlin Germany*. [cited.

27. Melville, D., *Direct magnetic separation of red cells from whole blood.* Nature, 1975. **255**(5511): p. 706.

28. Sun, L.P., et al., *Continuous, flow-through immunomagnetic cell sorting in a quadrupole field.* Cytometry, 1998. **33**(4): p. 469-475.

29. McCloskey, K.E., J.J. Chalmers, and M. Zborowski, *Magnetic cell separation: Characterization of magnetophoretic mobility.* Analytical Chemistry, 2003. **75**(24): p. 6868-6874.

30. Owen, C.S., et al., *Rapid magnetic purification of rosette-forming lymphocytes.* J Immunol, 1979. **123**(4): p. 1778-80.

31. Odette, L.L., M.A. McCloskey, and S.H. Young, *Ferritin Conjugates as Specific Magnetic Labels - Implications for Cell-Separation.* Biophysical Journal, 1984. **45**(6): p. 1219-1222.

32. Owen, C.S. and J.G. Lindsay, *Ferritin as a Label for High-Gradient Magnetic Separation.* Biophysical Journal, 1983. **42**(2): p. 145-150.

33. Zborowski, M., et al., *Immunomagnetic isolation of magnetoferritin-labeled cells in a modified ferrograph.* Cytometry, 1996. **24**(3): p. 251-259.

34. Bothwell, M. and T. Block, *Use of iron- or selenium-coupled monoclonal antibodies to cell surface antigens as a positive selection system for cells.* Methods Enzymol, 1986. **121**: p. 771-83.

35. Brady, G.W., et al., *The structure of an iron core analog of ferritin.* Biochemistry, 1968. **7**(6): p. 2185-92.

36. Michaelis, L., C.D. Coryell, and S. Granick, *FERRITIN. III. THE MAGNETIC PROPERTIES OF FERRITIN AND SOME OTHER COLLOIDAL FERRIC COMPOUNDS.* J. Biol. Chem., 1943. **148**(3): p. 463-480.

37. Granick, S., Michaelis, L., J. Biol. Chem., 1943. **147**(91).

38. Coryell, C.D., Stitt, F., and Pauling, L., J. Am. Chem. Soc., 1937. **69**(633).

39. Westermeier, R., *Electrophoresis in practice : a guide to methods and applications of DNA and protein separations* 2005, Weinheim: Wiley-VCH.

40. Jones, P., *Gel electrophoresis : nucleic acids*. 1995, Chichester: Wiley.

41. Martin, R., *Gel electrophoresis : nucleic acids*. 1996, Oxford: Oxford.

42. Kremser, L., D. Blaas, and E. Kenndler, *Capillary electrophoresis of biological particles: Viruses, bacteria, and eukaryotic cells.* Electrophoresis, 2004. **25**(14): p. 2282-2291.

43. Weinberger, R., *Practical Capillary Electrophoresis, 2nd Ed.* 2000, San Diego: Academic Press.

44. Righetti, P.G., *Capillary electrophoresis in analytical biotechnology*. 1996, Boca Raton, Fla.: CRC Press.

45. Deyl, Z., *Electrophoresis : a survey of techniques and applications*. 1983, Amsterdam: Elsevier Scientific Pub. Co.

46. Strege, M.A., LaguAvinash L. , *Capillary electrophoresis of proteins and peptides*. 2004, Totowa, N.J. : Humana Press.

47. Shapiro, H., M., *Practical Flow Cytometry*. 2003, Hoboken, NJ: Wiley-Liss. 681.

48. Bonner, W.A., et al., *Fluorescence activated cell sorting.* Rev Sci Instrum, 1972. **43**(3): p. 404-9.

49. Andersson, H. and A. van den Berg, *Microfluidic devices for cellomics: a review.* Sensors and Actuators B-Chemical, 2003. **92**(3): p. 315-325.

50. Shapiro, H.M., *Practical flow cytometry*. 2003, Hoboken, NJ Wiley-Liss.

51. Perkel, J.M., *How It Works | Fluorescence-Activated Cell Sorter.* The Scientist, 2004. **18**(14): p. 40.

52. McClain, M.A., et al., *Flow cytometry of Escherichia coli on nucrifluidic devices.* Analytical Chemistry, 2001. **73**(21): p. 5334-5338.

53. Micromod, P.G., www.micromod.de.

54. Ahn, C.H., et al., *A fully integrated micromachined magnetic particle separator.* Journal of Microelectromechanical Systems, 1996. **5**(3): p. 151-158.

55. Rida, A., V. Fernandez, and M.A.M. Gijs, *Long-range transport of magnetic microbeads using simple planar coils placed in a uniform magnetostatic field.* Applied Physics Letters, 2003. **83**(12): p. 2396-2398.

56. Wirix-Speetjens, R. and J. de Boeck, *On-chip magnetic particle transport by alternating magnetic field gradients.* Ieee Transactions on Magnetics, 2004. **40**(4): p. 1944-1946.

57. Choi, J.W., T.M. Liakopoulos, and C.H. Ahn, *An on-chip magnetic bead separator using spiral electromagnets with semi-encapsulated permalloy.* Biosensors & Bioelectronics, 2001. **16**(6): p. 409-416.

58. Lee, H., A.M. Purdon, and R.M. Westervelt, *Micromanipulation of biological systems with microelectromagnets.* Ieee Transactions on Magnetics, 2004. **40**(4): p. 2991-2993.

59. Lee, H., A.M. Purdon, and R.M. Westervelt, *Manipulation of biological cells using a microelectromagnet matrix.* Applied Physics Letters, 2004. **85**(6): p. 1063-1065.

60. Lee, H., et al., *Controlled assembly of magnetic nanoparticles from magnetotactic bacteria using microelectromagnets arrays.* Nano Letters, 2004. **4**(5): p. 995-998.

61. Lee, C.S., H. Lee, and R.M. Westervelt, *Microelectromagnets for the control of magnetic nanoparticles.* Applied Physics Letters, 2001. **79**(20): p. 3308-3310.

62. Deng, T., et al., *Manipulation of magnetic microbeads in suspension using micromagnetic systems fabricated with soft lithography.* Applied Physics Letters, 2001. **78**(12): p. 1775-1777.

63. Zborowski, M., et al., *Continuous progenitor cell selection by magnetophoresis.* Experimental Hematology, 2007. **35**(9): p. 92-93.

64. Jing, Y., et al., *Blood progenitor cell enrichment from clinical leukapheresis product by magnetic immunolabeling and magnetophoresis.* Experimental Hematology, 2006. **34**(9): p. 72-72.

65. Espy, M.A., et al., *An instrument for sorting of magnetic microparticles in a magnetic field gradient.* Cytometry Part A, 2006. **69A**(11): p. 1132-1142.

66. Dunlop, D., *Rock magnetism : fundamentals and frontiers*. 1997, Cambridge: Cambridge University Press.

CHAPTER TWO: Fabrication and Characterization of Magnetic Particles

Introduction

Three different types of magnetic particles were utilized for these magnetophoresis investigations: horse spleen ferritin, superparamagnetic polymer beads, and ferromagnetic nickel nanorods. The choice of these particular particles for use in this investigation will be discussed in detail later. This chapter describes the magnetic characterization of the particles utilized in this investigation. The magnetic characterization of the particles used in these investigations was the first step in fully characterizing the magnetophoretic systems which were used for magnetically driving the particles. This is also the first report to focus on the room temperature magnetic characterization of ferritin.

Magnetometry

All of the magnetic characterizations were performed at room temperature using a Quantum Design MPMS-5S Superconducting Quantum Interference Device (SQUID) magnetometer with the gracious support of Dr. Frank Tsui, University of North Carolina. The SQUID magnetometer measured the magnetization of a sample as a function of an applied magnetic field. The magnetic field of the magnetometer was produced by a superconducting magnetic coil into which the sample was placed. The position of the magnetized sample was changed within the applied magnetic field which produced a slight variation in the overall field. This change in the field was detected using a Josephson junction which in turn enabled the determination of the magnetization of the sample.[67] The SQUID magnetometer used in these analyses was capable of applying fields of up to 5 Tesla and had a lower magnetization detection limit of 1 x10^{-7} emu.[68]

A typical magnetization measurement involved cyclically scanning the applied field starting at a maximum positive field, through zero to a maximum negative field and then back to the original field. This type of measurement is generally referred to as a hysteresis scan, though the data may or may not exhibit hysteresis depending on the nature of the sample. Although low temperature magnetization measurements can be performed using the SQUID magnetometer, all of the magnetization measurements reported in this study were taken at 290K. Given the biomedical context of this study, only the magnetization of the particles at room temperature was relevant to magnetophoretic investigations. The sample holder used in the magnetic characterizations consisted of a gelatin capsule (gel cap) placed inside a plastic drinking straw as per the manufacturer's protocol.

While the term susceptibility denotes the magnetization of a sample as a function of the applied field, it is associated with several specific conventional systems of units related to an intrinsic material characteristic such as the density, such as emu/Gauss per gram. For this reason it is not appropriate to refer to the magnetization of a *sample* versus the applied field as the susceptibility without normalizing with respect to the volume, or to the mass of the sample. Therefore throughout the description of the magnetic characterization of the particles, the term susceptibility will be reserved for cases when the magnetization of a sample as a function of field has been determined with respect to either the volume or mass of the sample.

Experimental, Results and Discussion

MyOne Bead Characterization

Commercial MyOne beads supplied by Dynal Biotech were characterized by SQUID magnetometry. At the time of this investigation the manufacturer was not able to supply reliable values for the magnetic characteristics of the beads. This opinion was formulated based on personal communication with representatives of the manufacturer[24], and a report in the literature by Amblard et al which described discrepancies between the manufacturer supplied values and the measured magnetic characteristics of Dynal beads[3]. MyOne are paramagnetic, highly monodispersed beads 1.05 μm in diameter. The beads are available from the supplier with a variety of surface functionalizations. Carboxy functionalized MyOne beads were used for this study although the specific functionalization is not relevant to the magnetic properties of the particles.[24] MyOne beads are reported by the manufacturer to have a composition of 37% ferrites (w/w), which consist of an unknown ratio of magnetite (Fe_3O_4) and maghemite (Fe_2O_3), within a polystyrene matrix.

The MyOne beads are available from the manufacturer as an aqueous suspension. The SQUID sample chamber was under vacuum and therefore required the dehydration of the aqueous suspension of microspheres. A 20 μL volume of bead suspension was dehydrated prior to SQUID analysis. Magnetization data was taken over a magnetic field range of ±50k Gauss (5 Tesla). The diamagnetic background of the polymer matrix of the beads and the sample holder (gel cap and straw) is perceptible in the raw data by imparting a slight negative slope to the magnetization at saturation. This diamagnetic effect linearly decreases the measured magnetization of the sample and was therefore subtracted from the magnetization data, including the hysteresis curves in figure 2.1, according to the accepted method which is described here. To remove the diamagnetic background from the magnetization data, a linear function was fit to the data in the region of saturation and the slope of the function equal to -2.3 x10^{-5} emu/g Gauss was subtracted from the magnetization values of the raw data.

The magnetization data was also normalized with respect to the mass of the beads in the sample and the magnetization per gram of sample was plotted as a function of the applied field as shown in figures 2.1. Figure 2.1 B presents the MyOne magnetization over the full range of applied fields while 2.1 A shows the same data presented over a more narrow range of applied field values in order to highlight the linear regime of the data near 0 Gauss. To calculate the mass of the beads in the sample, the concentration of beads in the suspension was measured by counting the beads by microscopic hemocytometry. From the bead count it was determined that the MyOne bead concentration of the stock which was used was 2.4 x10^7 (±8%) beads per μL. The calculations for determining the bead concentration from the hemocytometry count are shown in appendix 3.The mass of beads in the sample was calculated to be 2.6 x10^{-4} (±11%) g according to equation 2.0 where the density of the MyOne beads is 1.8 g/cm^3 (±3%) as given by the manufacturer.

$$\left(2.4\cdot 10^{7}\,beads\right)\frac{\left(6\cdot 10^{-19}\,m^{3}\right)}{bead}\rho_{bead}\left(\frac{g}{m^{3}}\right)=2.6\cdot 10^{-4}(\pm 3\cdot 10^{-5})g \qquad \text{Equation 2.0}$$

The SQUID magnetometer measured the magnetization of the sample with a user defined number of replicate magnetization measurements at each applied field value. Five magnetization measurement replicates were taken at each field value for the MyOne magnetization data presented here, with the uncertainty of the magnetization σ_m taken as the standard deviation between the replicates. The calculation of the uncertainty in the magnetization was necessary for quantifying the magnetophoretic force on the MyOne beads which will be discussed later.

The uncertainty of the magnetization per mass $\sigma_{m/mass}$ was calculated from the uncertainties in the bead concentration and σ_m according to equation 2.1 where m is the magnetization value of the sample and the uncertainty in the bead concentration is $\frac{\sigma_{conc}}{conc} = 8\%$.

$$\sigma_{m/mass} = \sqrt{\left(\frac{\sigma_{conc}}{conc}\right)^2 + \left(\frac{\sigma_m}{m}\right)^2} \cdot \frac{m}{mass} \qquad \text{Equation 2.1}$$

This uncertainty served as the y axis error in the plot of the magnetization as a function of applied field shown in figure 2.1.

The saturation magnetization of the MyOne beads m_{sat} = 30.0 ± 0.4 emu/g was determined by taking the average of the magnetization values at saturation between ±10k and ±50k Gauss. The uncertainty in m_{sat} was obtained from the standard deviation in the magnetization values within this applied field range. The MyOne sample attained a magnetization 95% of its maximum at an applied field magnitude of 5k Gauss as evinced by figure 2.1. The field value of 5k Gauss (5 T) was therefore taken as the saturating field.

The calculation of a theoretical force which can be applied to a magnetized particle in a known field, as will be needed later, necessitates the determination of the magnetization per particle. The magnetization per MyOne bead was determined by calculating the number of beads in the SQUID sample and normalizing (dividing) the sample magnetization by the number of beads. The number of beads in the sample was calculated from the volume of the MyOne bead suspension used as the SQUID sample V_{Suspen} and the concentration of the MyOne bead as determined from the hemocytometer bead counts of the microsphere suspension.

The magnetization of a single MyOne bead was calculated by the accepted method of determining the slope of the linear fit of the magnetization versus field in the linear regime; ±500 Gauss in this case. The magnetization curve deviates from linearity above +500 G and below -500G, but is well approximated by a linear fit within this range as seen in figure 2.2. The slope of the error weighted linear fit, and thus the magnetization of a MyOne bead as a function of the applied magnetic field, was determined to be $1.8 \text{ x}10^{-13} \pm 6.9 \text{ x}10^{-15}$ Am^2/Tesla. The uncertainty in the magnetization per bead, derived from the uncertainty in linear fit, represents 4% of the magnetization value.

The mass susceptibility χ_m was calculated in a similar manner as the magnetization per bead. The slope of the linear fit of the magnetization per gram of beads as a function of the applied field was taken within the applied field range of ±500 Gauss as shown in figure 2.3. The slope of the linear fit to this data is the mass susceptibility which is equal to $3.7\ \mathrm{x}10^{-2}\ \left(\pm 1.1\ \mathrm{x}10^{-3}\right)\dfrac{\mathrm{emu}}{\mathrm{Gauss}\cdot\mathrm{g}}$. The uncertainty in χ_m is 4%, also derived from the uncertainty in the slope of the linear fit.

The mass susceptibility can be converted from cgs to SI units, as presented in table 1.1, through the conversion factor $\dfrac{m^3}{kg}=\left(\dfrac{10^3}{4\pi}\right)\dfrac{emu}{Oe\cdot g}$ where Oe and Gauss are used interchangeably. Thus χ_m of the MyOne beads was $4.7\cdot 10^{-4}\dfrac{m^3}{kg}$ in SI units according to equation 2.2. The manufacturer's stated mass susceptibility range of the MyOne microspheres at the time of purchase was 8.0 to 8.5 x10^{-4} m^3/kg.[69]

$$\chi_m = 3.7\cdot 10^{-2}\frac{emu}{Oe\cdot g}\cdot\frac{1\dfrac{m^3}{kg}}{\left(\dfrac{10^3}{4\pi}\right)\dfrac{emu}{Oe\cdot g}} = 4.7\cdot 10^{-4}\frac{m^3}{kg} \qquad \text{Equation 2.2}$$

The susceptibility can also be expressed as the volumetric susceptibility χ_v rather than mass susceptibility χ_m. This is calculated in SI units by multiplying χ_m by the density of a MyOne bead ($\rho_{MyOne}=1.8g/cm^3$) according to equation 2.3.

$$\chi_v = \chi_m\cdot\rho_{MyOne}$$

$$\chi_v = \left(4.7\cdot 10^{-4}\frac{m^3}{kg}\right)1800\frac{kg}{m^3} = 0.85 \text{ (dimensionless)} \qquad \text{Equation 2.3}$$

Dimensional analysis confirms that the volumetric susceptibility is a dimensionless parameter. The volumetric susceptibility can be converted from SI to cgs units by dividing χ_v (SI) by 4π; therefore resulting in χ_v = 6.8 x10^{-2} in cgs units. The susceptibilities of the MyOne beads in SI and cgs units as well as the conversion factors are summarized in table 2.1 for convenience.

Ferritin Characterization

The superparamagnetic nature of ferritin has been studied for decades.[70, 71] Much of the interest in the magnetic properties of ferritin, has historically focused on its properties at low temperatures and there are few room temperature magnetic studies of ferritin in the literature[72]. However, the data available in the literature on low temperature magnetization of ferritin are not relevant to the use of the protein as a magnetic label in a biological context. It was consequently necessary to independently characterize the magnetic properties of ferritin at room temperature.

Type 1 horse spleen ferritin was obtained as an aqueous solution from Sigma-Aldrich.[73] The sample was prepared for magnetic characterization by slowly evaporating the water overnight from a 60 μL aliquot which was dispensed into a SQUID sample holder. The magnetization of ferritin was measured over an applied field range of ±50k Gauss (±5 Tesla). The magnetization showed a nearly linear relationship with the applied field from 0 to ±5 Tesla with no indication of saturation or remanence; as is consistent with a superparamagnetic material. A hystersis curve taken over the full range of applied field conditions with an inset plot of the range of ±1000 Gauss is shown in figure 2.4. The mass of ferritin in the sample volume was determined using the measured volume and the manufacturer's stated ferritin concentration of 76 ±1 mg/mL to be 4.56 ±0.06 x10^{-3} g. The magnetization of the ferritin sample was normalized with respect to the mass of sample.

The mass susceptibility χ_m of ferritin was determined from the slope of the linear fit to the magnetization data over the applied field range of ±1000 Gauss as shown in figure 2.4 B. The mass susceptibility (χ_m) of ferritin was therefore calculated to be $1.1 \cdot 10^{-5}\left(\pm 1.5 \cdot 10^{-7}\right)\dfrac{emu}{Gauss \cdot g}$, where the uncertainty in χ_m is derived primarily from the uncertainty in the mass of ferritin in the sample.

The mass susceptibility of ferritin in SI units is calculated to be χ_m =1.4 x10^{-7} m^3/kg, according to the same methodology as used above for the determination of the MyOne bead susceptibility. In order to calculate the volumetric susceptibility of ferritin χ_v, χ_m as previously determined needed to be multiplied by the density of the particle as was done for the same calculation for the MyOne beads. There is little information available in the literature regarding the density of ferritin, consequently it was calculated from the molecular weight and volume of the protein. Ferritin is spherical and highly regular with a diameter of 24 nm. The volume of a single protein was therefore calculated according to equation 2.4.

$$V_{ferritin} = \frac{4}{3}\pi\left(12nm\right)^3 = 7.2 \cdot 10^{-24} m^3 \qquad \text{Equation 2.4}$$

Ferritin is composed of two distinct components, a peptide shell and an iron core. The molecular weight of the peptide shell is 440kDa, or 7.3 x10^{-19} g.[73] The size of the iron core of ferritin is highly dependant on the manufacturer’s processing and the protein harvesting conditions. While the iron loading of the ferritin used in this investigation was not specifically determined, a loading of 1000 iron atoms per ferritin is typical and therefore was assumed for purposes of calculating the density.[74, 75] The iron core of ferritin is maintained in ferritin as an oxide, or as a combination of several oxides, and may be accompanied by phosphate.[76, 77] The oxidation state of the iron in the core, and the possible presence of phosphate, are unknowns in our investigation which depend on the processing of the ferritin. The core was therefore assumed to have a mass equivalent to 1000 iron atoms with the corresponding core mass calculated in equation 2.5.

$$\frac{55.9g}{molFe}\frac{N_A}{mol} = 9.3\cdot 10^{-23}\, g\big/_{Fe}\cdot 1000Fe = 9.3\cdot 10^{-20}\, g\big/_{core} \qquad \text{Equation 2.5}$$

The total mass per ferritin including the peptide shell and the iron core containing 1000 iron atoms was calculated to be 8.2 x10^{-19} g. The density of a single ferritin protein with an iron loading of 1000 Fe atoms, ρ_{ferritin} , was calculated in equation 2.6.

$$\rho_{ferritin} = \frac{8.2\cdot 10^{-19}g}{7.2\cdot 10^{-24}m^3} = 1.1\cdot 10^5\, g\big/_{m^3} = 110kg\big/_{m^3} \qquad \text{Equation 2.6}$$

The volumetric susceptibility of ferritin χ_v in SI units is calculated as described previously by multiplying χ_m by ρ_{ferritin} as in equation 2.7.

$$\chi_{V_{ferritin}} = \frac{1.4\cdot 10^{-7}m^3}{kg}\frac{110kg}{m^3} = 1.6\cdot 10^{-5}(SI) \qquad \text{Equation 2.7}$$

The volumetric susceptibility of ferritin in SI units is converted to cgs units by dividing by 4π as described previously for the MyOne beads. Table 2.2 summarizes the susceptibilities of ferritin for the convenience of the reader.

The scaling of the magnetic properties of nanoparticles is a complex issue which is outside of the scope of this dissertation.[78] Therefore no attempt is made in this document to draw connections between the magnetic properties of bulk iron oxides and ferritin which would be appropriate for the prediction of the susceptibility of ferritin. The best validation of the magnetic characterization of ferritin which is reported in this investigation is therefore available in comparison with the results of a temperature dependant study of the magnetization of ferritin by Kilcoyne.[72]

The emphasis of the work by Kilcoyne was primarily on the low temperature magnetization of ferritin, as is typical of most of the literature related to magnetic investigations of ferritin. While ambient temperature magnetization values are specifically given in the paper for ferritin, a plot of the magnetization of ferritin during a single scan from 0 to 5 Tesla for several temperatures is given in the paper which includes magnetization data taken at 290K. This plot from the paper by Kilcoyne et al is shown in figure 2.5. The mass susceptibility of ferritin at room temperature was estimated from figure 2.5 to be equal to $1.4 \cdot 10^{-5} \frac{emu}{Gauss \cdot g}$. The calculation of the susceptibility from the figure is set out in detail in appendix 4. The susceptibility estimate from Kilcoyne's data is slightly below the value reported in this investigation, but agrees reasonably well being more than 80% of our determined mass susceptibility value.

Nickel Nanorod Fabrication

Nickel nanorods were fabricated in house (courtesy of Kwan Skinner) by electrochemical deposition using a commercially available anodized alumina oxide (AAO) membrane as the template. The fabrication method was adapted from a protocol reported by Neilsch and co-workers. [79] A detailed description of the fabrication procedure is included in appendix 5.

Following fabrication, the rods were released from the membrane template and suspended in a dilute surfactant solution for storage. After processing, the rods were exposed to a magnetic field in excess of 4k Gauss which served to induce a permanent magnetization. A scanning electron micrograph of the cross section of the nickel rods embedded in the membrane is shown in figure 2.6.

Nickel Nanorod Characterization

Shape anisotropy can play a role in the magnetization of asymmetric nanoparticles. A magnetized particle will have magnetic poles at its surface which will produce a demagnetizing field in the opposing direction to the magnetization. If a field is applied along the major axis of a needle shaped particle for example, the surface dipoles will be less and the resulting demagnetizing field smaller, than if the field was applied perpendicular to the major axis.[9] This results in an easier magnetization with the field applied along the major axis.

A number of researchers have investigated the magnetization of micro-scale and sub-micron rod shaped particles as a function of the orientation of the applied field with respect to the easy axis of asymmetric particles.[78, 80, 81] It has been demonstrated that asymmetric particles will often display different magnetization characteristics depending on the angle of the rod axis with respect to the applied magnetic field.[82-84] As a result, the nickel rods used in this investigation were magnetically characterized by SQUID susceptometry with the applied field oriented both parallel and perpendicular to the easy axes of the rods.

The rods were magnetically characterized while still embedded in the AAO membrane in which they were fabricated. Maintaining the rods in the membrane during susceptometry measurements allowed for the adjustment of the rod axis with respect to the field, and also resulted in the sample having a high concentration of magnetic particles. The high particle concentration of the sample provided a good signal to noise ratio thus enabling reliable and reproducible susceptometry measurements. The hysteresis curves for the rod array embedded in the AAO membrane are shown in figure 2.7 over a narrow applied field range (A) and over the full range of applied fields as an inset plot (B). The data points in black were taken with the rod axes oriented parallel to the applied field, while the red points were taken with the rods oriented perpendicular to the applied field.

The magnetization of the rod array reached 95% of the saturation magnetization at 4k Gauss (0.4 Tesla). During magnetically driven experiments however, the maximum field applied to a rod is always less than 600 Gauss (0.06 Tesla). Therefore, under all experimentally relevant conditions the rods have a magnetization significantly less than the saturation magnetization. Since the rods were below saturation magnetization under magnetophoretic experimental conditions, the predicted magnetic force which was applied to the rods could be calculated conveniently from the susceptibility and the remanent magnetization of the particles. The predicted theoretical forces based on these values will be discussed in chapter 3.

It is apparent from figure 2.7 that the hysteresis curves values of the rod array in the two orientations are very similar. The saturation magnetization of the rod array with the rods oriented perpendicular to the applied field was $m_{\perp} = 4.3 \text{ x}10^{-5}$ Am^2. While the magnetization at saturation of the rod array when the field was oriented parallel to the rod axis was only 10% less with $m_{\|} = 3.8 \text{ x}10^{-5}$ Am^2. The gel cap and drinking straw which were used as a sample holder both had a small diamagnetic background, but due to the large magnetization of the rod sample contributed to less than 0.6% of the overall magnetization. This diamagnetic background was therefore determined to be insignificant and no efforts were made to subtract it from the sample magnetization in the case of the nickel rod sample.

The magnetization of the entire rod array sample was normalized with respect to the magnetization of an individual rod by dividing by the number of rods in the sample which was determined in the following manner. By assuming that each pore contained a rod, the number of rods in the sample used in the SQUID measurements was calculated by measuring the size of the membrane sample. The pore density of the AAO membrane was known to be 9 x10^{12} rods/m^2. The section of the membrane which was analyzed had a measured area of 6 x10^{-6} m^2. It was assumed that there was a 5% error in the area value based upon the uncertainty of the measurement of the dimensions of the membrane section. This resulted in a calculated value of 5 x10^7 (±3 x10^6) rods in the sample section which was analyzed. After normalizing with respect to the number of rods in the sample, the saturation magnetizations per rod with the applied field oriented parallel and perpendicular to the rod axis were calculated to be $m_{\|} = 7.0 \cdot 10^{-13} \dfrac{Am^2}{rod}$ and $m_{\|} = 7.9 \cdot 10^{-13} \dfrac{Am^2}{rod}$ respectively.

The magnetophoresis of the rods will be discussed in chapter 3. The direction of motion of the magnetically driven rods was parallel to the field applied with the permanent magnet. The magnetization measurements obtained with the rods parallel to the applied field was therefore the orientation with experimental relevance. As a result the SQUID data taken with the rods oriented parallel to the applied field was used in the subsequent calculations.

It has been reported that the packing density of particles, such as the nickel rods examined here, may effect the measured magnetic properties of a sample.[83, 85, 86] Ecinas-Oropesa et al obtained hysteresis curves for arrays of membrane embedded nickel nanowires at different packing densities by applying the field perpendicular and parallel the rod axes.[87] The rods used in the Ecinas-Orepesa investigation were of similar dimensions to those described here and were fabricated by a similar electrochemical deposition method. The measured susceptibilities of these rod arrays as functions of the applied field orientations were strongly influenced by the packing densities.

Figure 2.8, adapted from Ecinas-Oropesa et al, shows hysteresis curves of rod arrays at packing densities of 4% and 35-38% as a function of the orientation of the applied field. The dimensions of the rods in the arrays were 56 nm in diameter by 22 μm in length and 250 nm in diameter by 60 μm in length for the low and high packing densities respectively. At the high packing density shown in plot (b) of figure 2.8, the hysteresis curves resulting from the field applied perpendicular and parallel have the same slope in the linear regime. This indicates that the measured susceptibility of the sample was not a function of the applied field orientation. However, the hysteresis curves taken of the low packing density array shown in plot (a) of the figure indicate a strong dependence of the measured susceptibility on the applied field orientation evinced by the dramatically different slopes for the linear regimes of the two hysteresis curves.

At the low packing density, the application of the field parallel to the rod axes results in a measured susceptibility, as estimated based on the slope of the linear regime, which was approximately 5 times greater than when the field was applied perpendicular to the axes of the rods. Ecinas-Oropesa's findings suggest that the susceptibility of an individual rod used in this investigation may in fact be five times greater than the measured susceptibility per rod as calculated above. This increase in the susceptibility of an isolated rod over the value measured from the rod array sample was taken into account during the prediction of the magnetophoretic force on individual rods in chapter 3.

The saturation magnetization values measured for the arrays reported by Ecinas-Oropesa et al were constant regardless of the orientation of the applied field. The high packing density of the rod array used in this investigation was therefore not expected to have an effect on the measured saturation magnetization. The comparison of the saturation magnetization values obtained in this investigation with those taken on similar rods reported by Hultgren et al showed that the two measurements were in good agreement.[88]

The magnetization of a sample is inherently a function of the volume of magnetizable material. The rods utilized by Hultgren where fabricated by an AAO membrane electrochemical deposition method similar to ours. Hultgren's rods were of somewhat different dimensions from those of this investigation however, being 350 nm in diameter and 35 microns long. Comparing the volume of the rods used in Hultgren's investigation with ours, it was determined that ours had a volume 34% that of Hultgren.

The transition from the magnetic behavior observed for bulk materials to those of submicron particles is related to dimensions of Weiss domains in the material. Weiss domains are areas in the crystal structure of ferromagnetic material of approximately a hundred nanometers which may have uniformly oriented magnetic momenta imparting bulk magnetic properties.[89] The major axes of the rods described by Hultgren, as well as those used in this investigation, are larger than the Weiss domain. The magnetic behavior of both kinds of rods is therefore expected to be similar, thus legitimizing the comparison of the magnetic properties of the two rod types.

The comparison of our saturation magnetization per rod with that of Hultgren based on the volumes of the respective rods represents a reasonable first approximation. The saturation magnetization value reported by Hultgren was 1.4 $\times 10^{-12}$ Am^2/rod while ours was 0.7 $\times 10^{-12}$ Am^2/rod. Since our rods have a smaller volume which is only 34% that of Hultgren, it is appropriate to normalize the Hultgren magnetization value by multiplying by 0.34 in order to account for the difference in the volumes. This results in a volume normalized saturation magnetization value for Hultgren's rods of 0.5 $\times 10^{-12}$ Am^2/rod. Thus, the comparison of the saturation magnetization of our nickel nanorods with those published by Hultgren results in a value within 40% after normalizing for the difference in size between the two types of rods.

The nickel rods used in this investigation have a ferromagnetic character which results in a remanent magnetization which is observed as the residual magnetization at zero applied field in figure 2.9. Both the remanence and the magnetization as a function of the applied field were calculated from the SQUID magnetization measurements at low field between -0.2 T and 0.2 T. The upper magnetization data were taken while scanning the field from positive to negative values and the lower scan from negative field to positive field values. Both upper and lower data are substantially the same however.

The remanent magnetization and the magnetization as a function of the applied field of the rod array were determined from the hysteresis data within the linear regime between ±0.2T. The positive (lower) field scan data within this field range were transposed on to the negative field scan data by multiplying the ordinate values of the positive scan by -1. The linear fit to the data was then obtained as shown in figure 2.10. The magnetization as a function of the applied field and remanent magnetization of the rod array were determined as the slope and the y axis intercept respectively of the linear fit to the transposed data in figure 2.10. Equation 2.8 is the equation of the line of the linear fit where 1.6 x10^{-1} Am^2/T is the susceptibility and 2.5 x10^{-6} Am^2 is the remanent magnetization.

$$y = m \cdot x + b$$

$$m(B) = \left(1.6 \cdot 10^{-4} \frac{Am^2}{T} \right) \cdot B + 2.5 \cdot 10^{-6} Am^2 \qquad \text{Equation 2.8}$$

The magnetization of a single rod as a function of the applied field was calculated by dividing the slope and the y axis intercept by the number of rods in the array sample. Equation 2.9 therefore describes the measured magnetization of a single rod as a function of the applied field as determined from measurements of the rod array.

$$m(B)_{rod} = \left(3.0 \cdot 10^{-12}\,\frac{Am^2}{T}\right) \cdot B + 4.6 \cdot 10^{-14}\,Am^2 \qquad \text{Equation 2.9}$$

As has been discussed previously however, the results of Ecinas-Orepesa[87] indicate that using the measurements of an array of rods underestimates the susceptibility of an individual rod by approximately five times. The value for the magnetization as a function of the applied field of an individual rod equal to 1.5 x10^{-11} Am^2/T will therefore be used in subsequent calculations. The magnetic characterization of these particles, in addition to the characterization of the magnetic fields, will permit the calculation of the expected forces which can be applied to the particles in the next chapters. The comparison of the predicted force with the observed force will enable us to begin closing the loop between the magnetic properties of small particles and the magnetic forces which can be applied to them.

Figures

Figure 2.1

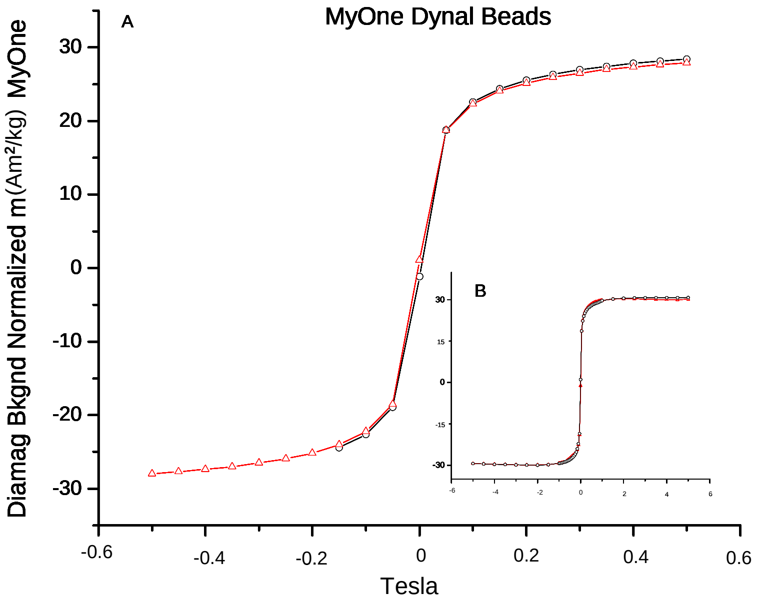

This figure presents the magnetization of MyOne beads as a function of applied magnetic field measured at 290K by SQUID magnetometry. A maximum field magnitude of 50k Gauss (5 T) was applied to the sample. The data have been normalized to account for the slight diamagnetic background due to the polymer matrix of the beads and the sample holder. The magnetization values have also been normalized with respect to the mass of the sample so that the data are expressed in the magnetization per gram of beads. The data which are plotted in red represent the forward scan from positive to negative field values, and the data plotted are black are the reverse scan from negative field values back to positive. The expanded field range in figure 2.1 B permits the observation that the magnetization plateaus at 5k Gauss illustrating that the sample is approaching saturation magnetization. The magnetization at 5k Gauss is 95% of the maximum magnetization attained and was taken to represent the field required for magnetic saturation of the particles.

Figure 2.2

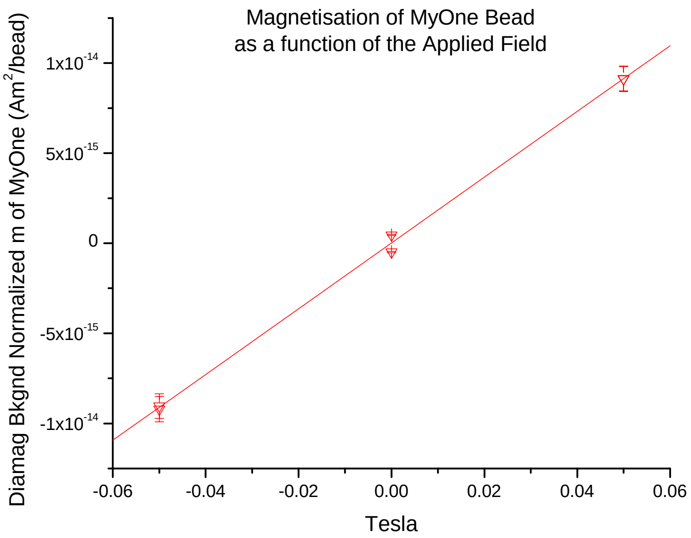

This figure presents the magnetization of the MyOne beads normalized with respect to a single bead. The red line is the error weighted linear fit to the data. The slope of the fit is equivalent to the magnetization of a MyOne bead as a function of the applied field. The uncertainty in the data is the standard deviation in the number of beads in the sample of 8% as determined by the error in the hemocytometric bead count.

Figure 2.3

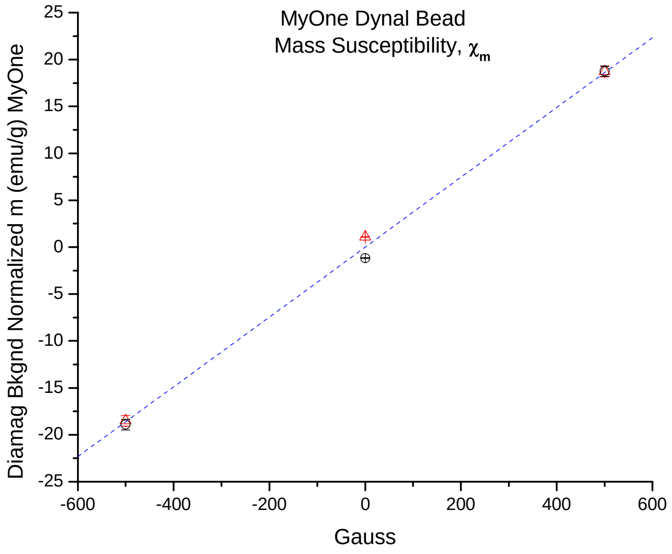

These data have been normalized to account for the slight diamagnetic background due to the polymer matrix of the beads and the sample holder. The magnetization values have also been normalized with respect to the mass of the sample so that the data are expressed in magnetization per gram of beads. The mass susceptibility χ_m of the sample is determined by the slope of the linear fit (blue dashed line) to the data within the field range of ±500 Gauss.

Table 2.1

Term	Symbol	SI units	cgs units	cgs to SI units conversion factor
MyOne volume susceptibility	χ_v	0.85	6.8 x10^{-2}	$\frac{SI}{4\pi} = c.g.s.$
MyOne mass susceptibility	χ_m	4.7 x10^{-4} m^3/kg	3.8 x10^{-2} emu/Gauss g	$\frac{m^3}{kg} = \frac{10^3}{4\pi}\frac{emu}{Oe \cdot g}$

This table summarizes the volumetric and mass susceptibility values of the MyOne beads. Volumetric susceptibility is dimensionless in the SI units system.

Figure 2.4

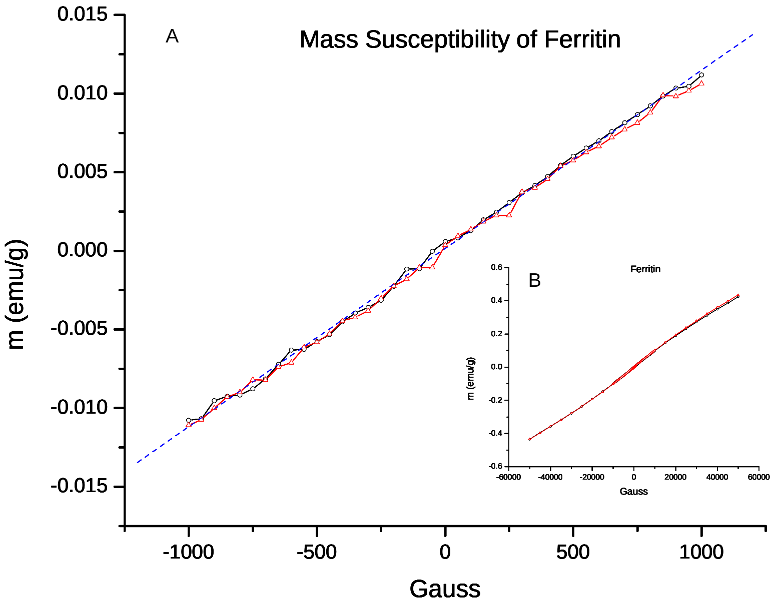

This figure shows the magnetization per gram of ferritin as a function of the applied field measured by SQUID susceptometry at 290K. These data represent both the forward and the reverse field scans. The nearly linear nature of the relationship of magnetization to the applied field over a wide range of field values, and the lack of remanence is typical of a superparamagnetic material such as ferritin. The insert plot (B) shows the magnetization as a function of the applied field over the full field range of ±5 T (50k Gauss). The primary plot (A) displays the data over the narrow range of applied fields of ±0.1 T (1k Gauss). This field range was selected due to the slight deviation from linearity in the magnetization as a function of the applied field above and below these field values. This narrow range of fields also better illustrates the highly linear nature of the magnetization of ferritin with field. The mass susceptibility is calculated as the slope of the linear fit to the data and is plotted as the blue dashed line in (A).

Table 2.2

Term	Symbol	SI units	cgs units	cgs to SI units conversion factor
Ferritin volume susceptibility	χ_v	1.6 x10^{-5}	1.3 x10^{-6}	$\frac{SI}{4\pi} = c.g.s..$
Ferritin mass susceptibility	χ_m	1.4 x10^{-7} m^3/kg	1.1 x10^{-5} emu/Gauss g	$\frac{m^3}{kg} = \frac{10^3}{4\pi}\frac{emu}{Oe \cdot g}$

This table summarizes the susceptibility values of ferritin measured by SQUID susceptometry. Volumetric susceptibility is dimensionless in the SI units system.

Figure 2.5

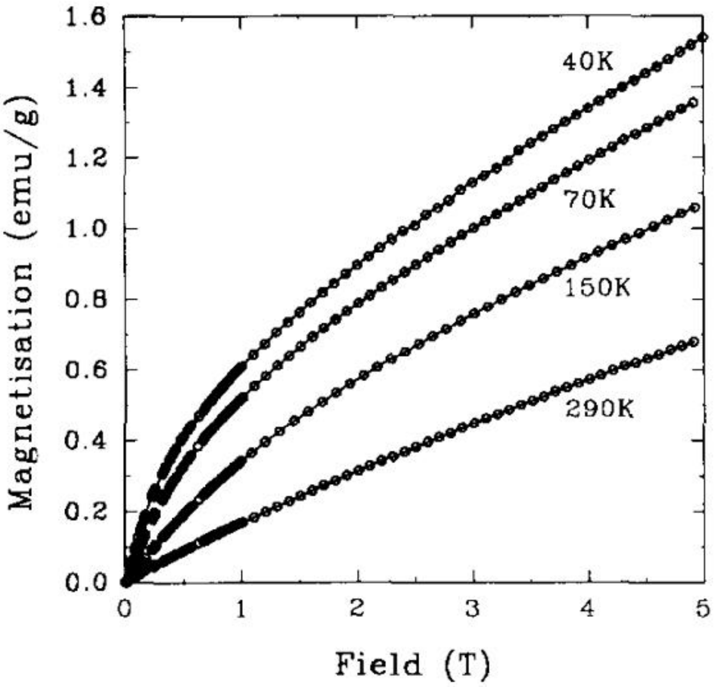

This figure shows a copy of a plot of the magnetization per gram of ferritin as a function the applied field at 4 temperatures published by Kilcoyne et al.[72] Data was taken using a vibrating sample magnetometer (VSM). The magnetization data taken at 290K demonstrates a linear dependence on the applied similar to the data presented in this investigation through figure 2.4. Since the data shown on the plot is of a unidirectional field scan, there is no way to determine if there is hysteresis indicative of remanence.

Figure 2.6

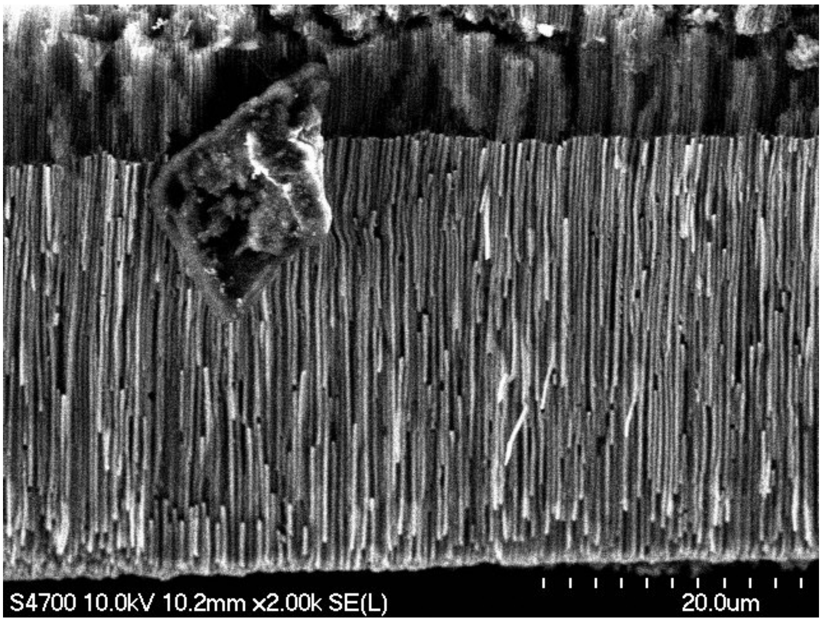

This figure shows scanning electron micrograph side view of nickel nanorods the same as those used in this investigation still embedded in the anodized alumina oxide (AAO) membrane. The membrane has been cut in half to expose the rods inside the membrane. The rods are 200 nm in diameter and 38 microns long. The rods were fabricated and the image was taken by Kwan Skinner.

Figure 2.7

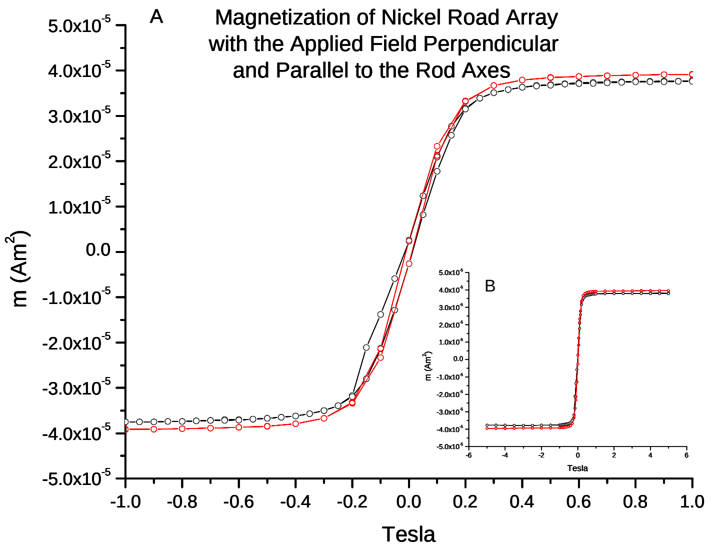

This figure shows the magnetization of the nickel nanorod array as a function of applied magnetic field measured by SQUID susceptometry at 290K. The data plotted in black represent measurements taken with the field applied parallel to the axis of the rods, while the data in red was taken with the rods oriented perpendicular to the applied field. The inset plot (B) shows the hysteresis curves over the full range of applied field values. Plot (A) depicts the same data displayed over the narrow field range of ±1 T to illustrate the similarity of the hysteresis curves at the different orientations of the field with respect to the axes of the rods..

Figure 2.8

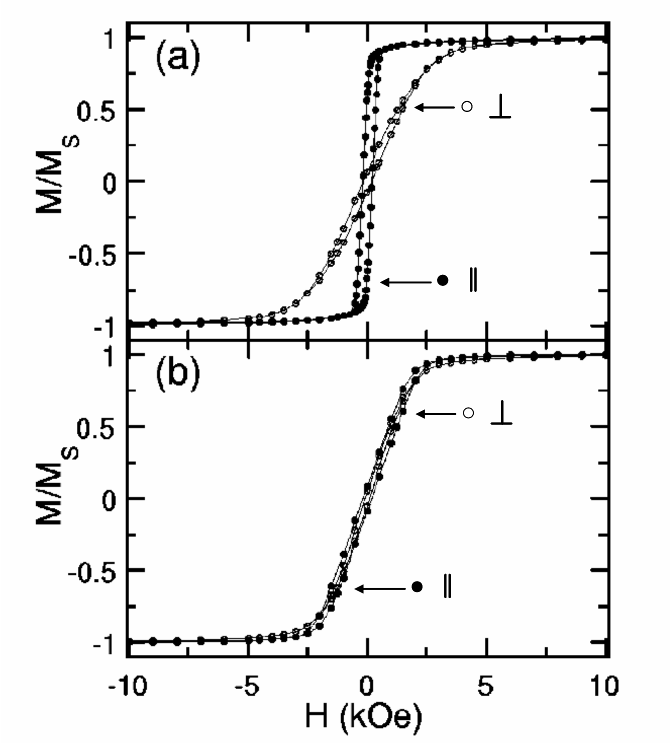

This figure is adapted from Ecinas-Orepesa et al[87]. The hysteresis curves were reported to have been taken with the magnetic field applied perpendicular (open circle) and parallel (filled circle) to the rod axes. Plot (a) shows hysteresis curves taken on a membrane bound array of Ni rods 56 nm in diameter by 22 μm in length at a packing density of 4% The rods in plot (b) are 250 nm in diameter by 60 μm in length and are at a packing density of 35-38%.

Figure 2.9

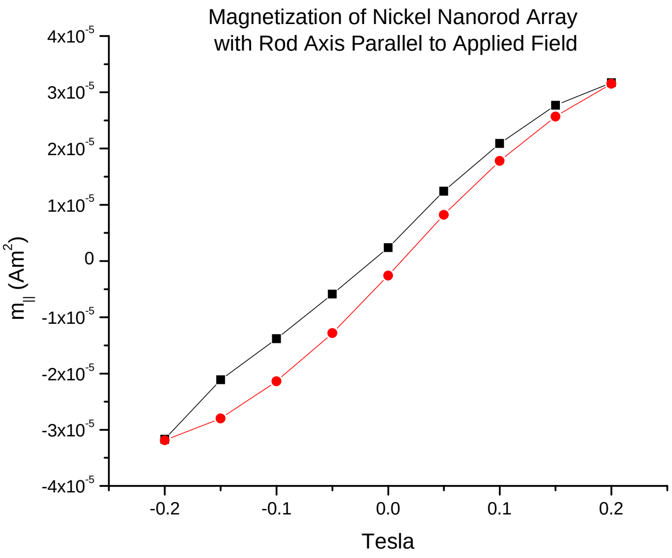

This figure shows the magnetization of the nickel rod array oriented with rod axis parallel to the applied field displayed over the narrow field range of ±0.2T to illustrate the remanent magnetization indicative of the ferromagnetic character of the rods. The data plotted in black is the magnetization of the rod array as the field is scanned negative from positive field values. The data plotted in red is the magnetization as the field is scanned positive from negative values. The hysteresis apparent through the difference in the magnetization between the positive and the negative field scans is the magnetic remanence.

Figure 2.10

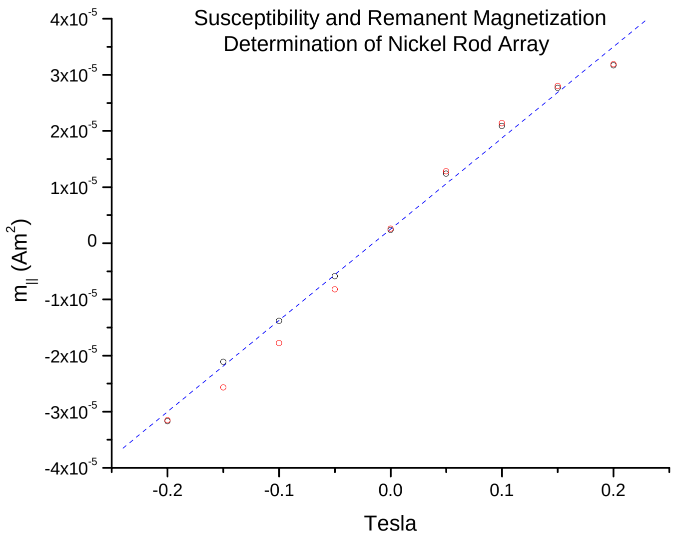

This figure shows the magnetization of the rod array over the narrow field range of the linear regime measured by SQUID susceptometry by applying the field parallel the axes of the rods in the array. The positive field scan magnetization values have been transposed on to the negative scan by multiplying the ordinate values of the positive scan data by -1. The blue dashed line is the linear fit to the magnetization data. The slope of this line is the magnetization of the array as a function of the applied field and the y intercept is the remanent magnetization of the array.

References

1. QuantumDesign, 6325 Lusk Blvd Sad Diego CA 92121-3733.

2. Gallop, J.C., *SQUIDSs, the Josephson Effects and Superconducting Electronics*. 1991, New York, NY: Taylor and Francis Group.

3. Dynal, B., www.dynal.no. Brown Deer WI.

4. Amblard, F., et al., *A magnetic manipulator for studying local rheology and micromechanical properties of biological systems.* Review of Scientific Instruments, 1996. **67**(3): p. 818-827.

5. Nokleby, L., *Dynal Biotech ASA, Tech Centre*, T. Meehan, Editor.

6. Russell, C.D. and L. Pauling, *The magnetic properties of the compounds ethylisocyanide ferrohemoglobin and imidazole-ferrihemoglobin.* Proceedings of the National Academy of Sciences of the United States of America, 1939. **25**: p. 517-522.

7. Coryell, C.D., Stitt, F., Pauling, L., *The magnetic properties and structure of ferrihemoglobin (methemoglobin) and some of its compounds.* Journal of the American Chemical Society, 1937. **59**: p. 633-642.

8. Kilcoyne, S.H. and R. Cywinski, *Ferritin - a Model Superparamagnet.* Journal of Magnetism and Magnetic Materials, 1995. **140**: p. 1466-1467.

9. Sigma-Aldrich, Ferritin from equine spleen F4503.

10. Ivano Bertini, A.S., Helmut Sigel *Handbook on Metalloproteins*. 2001, New York, NY: Marcel Dekker.

11. Treffry, A., J.M. Sowerby, and P.M. Harrison, *Variable Stoichiometry of Fe(Ii)-Oxidation in Ferritin.* Febs Letters, 1978. **95**(2): p. 221-224.

12. Treffry, A. and P.M. Harrison, *Incorporation and Release of Inorganic-Phosphate in Horse Spleen Ferritin.* Biochemical Journal, 1978. **171**(2): p. 313-320.

13. Huang, H.Q., et al., *Role of Phosphate in Fe2+ Binding to Horse Spleen Holoferritin.* Biochemistry, 1993. **32**(6): p. 1681-1687.

14. Batlle, X. and A. Labarta, *Finite-size effects in fine particles: magnetic and transport properties.* Journal of Physics D-Applied Physics, 2002. **35**(6): p. R15-R42.

15. Nielsch, K., et al., *Uniform nickel deposition into ordered alumina pores by pulsed electrodeposition.* Advanced Materials, 2000. **12**(8): p. 582-586.

16. Jones, T.B., *Electromechanics of Particles*. 1995, NY: Press Syndicate of the University of Cambridge.

17. Piraux, L., et al., *Anisotropic transport and magnetic properties of arrays of sub-micron wires.* Journal of Magnetism and Magnetic Materials, 1997. **165**(1-3): p. 352-355.

18. Fert, A. and L. Piraux, *Magnetic nanowires.* Journal of Magnetism and Magnetic Materials, 1999. **200**(1-3): p. 338-358.

19. Rahman, I.Z., et al., *Characterisation of electrodeposited nickel nanowires using NCA template.* Journal of Materials Processing Technology, 2004. **153-54**: p. 811-815.

20. Ciureanu, M., et al., *Magnetic properties of electrodeposited CoFeB thin films and nanowire arrays.* Electrochimica Acta, 2005. **50**(22): p. 4487-4497.

21. Han, G.C., et al., *Angular dependence of the coercivity and remanence of ferromagnetic nanowire arrays.* Journal of Applied Physics, 2003. **93**(11): p. 9202-9207.

22. Li, C.Z. and J.C. Lodder, *The Influence of the Packing Density on the Magnetic-Behavior of Alumite Media.* Journal of Magnetism and Magnetic Materials, 1990. **88**(1-2): p. 236-246.

23. Encinas-Oropesa, A., et al., *Effect of dipolar interactions on the ferromagnetic resonance properties in arrays of magnetic nanowires.* Journal of Applied Physics, 2001. **89**(11): p. 6704-6706.

24. Encinas-Oropesa, A., et al., *Dipolar interactions in arrays of nickel nanowires studied by ferromagnetic resonance.* Physical Review B, 2001. **6310**(10).

25. Hultgren, A., et al., *Cell manipulation using magnetic nanowires.* Journal of Applied Physics, 2003. **93**(10): p. 7554-7556.

26. J. Switalla, B.L.G., and L. Szunyogh, *Electronic theory of Bloch walls in ferromagnets.* Phys. Rev. B, 2001. **63**: p. 104423.

CHAPTER THREE: Magnetically Driven Particles in Karo and DNA

Motivation

Future applications of small particle magnetophoresis in analytical science and biomedicine will require a quantitative understanding of the forces involved in magnetically driven particle transport. The use of magnetophoresis for the predictive manipulation of particles in challenging new environments such as microfluidic devices and complex microstructured biological media necessitates a quantitative approach to investigating the relevant criterion of magnetomotive particle mobility. The application of microparticle magnetophoresis for drug delivery will require a better understanding than currently exist of the system parameters which constrain the driven transport of particles in complex biological media. General considerations which should direct the design of magnetophoretic systems include mobility requirements of the particles, the resistance of the medium to particle transport, size and shape requirements of the particles, the magnitude and geometry of the magnetic field, and the possible requirement of biocompatibility of the system.

There are few examples of published investigations which fully quantify the forces and magnetophoretic mobilities of individual micro-scale particles.[1-5] There is even less in the literature where an attempt is made to ‘close the loop’ between the magnetic properties of a particle, the applied magnetic field, the resulting magnetic mobility force and the particle mobility.[6] To intelligently address the demands of a specific magnetophoretic application, any approach will necessitate a thorough characterization of the system through the quantification of these relevant magnetophoretic parameters.

Investigation Overview

In the investigation described in this chapter, the magnetophoretic parameters of the experimental system were independently quantified. The magnetically driven velocities of individual MyOne beads and nickel nanorods in two media were measured. Karo, the first medium studied, is a model viscous medium, while the non-Newtonian fluids of DNA solutions served as the other media investigated. The velocities of the beads and the rods were correlated with the measured parameters of the system, for the first time enabling the relationships between magnetophoretic particle velocities and the relevant parameters of a fully characterized magnetophoretic system to be established.

In addition to closing the loop by connecting these causal relationships with the observed magnetophoretic phenomena, the use of Karo allowed the calculation of the forces on the two types of particles based on Stokes' law which then enabled the investigation of the shear thinning behaviour of the DNA solutions by the particle magnetophoresis. In this manner the quantification of the experimental magnetophoretic system served as a springboard to explore the influence of particle size and shape on the magnetically driven velocities on the particles in non-Newtonian biological polymer solutions of DNA.

The viscosity of the DNA solutions, as probed by the particles in this investigation, was observed to decrease with increasing particle velocity. This phenomena, known as *shear thinning*, has been observed by bulk rheology measurements for lambda DNA before.[7] However, this represents the first public disclosure of DNA shear thinning by driven particles. The observation that magnetically driven particles can induce shear thinning in biopolymer materials as demonstrated here has important implications for magnetic particle drug delivery in that it may serve to decrease the force necessary for in vivo particle transport.

Influence of Particle Shape on Velocity

As has been discussed previously, the net velocity of a particle undergoing magnetophoresis is the result of the magnetic driving forces and the drag forces. In the design of a microparticle magnetophoretic system, the question of the most efficient particle shape for rapid transportation in a particular medium should be posed. While the issue of particle shape has relevance for analytical magnetophoretic applications, its significance in complex biological media is paramount within the context of magnetic particle drug delivery.[8]

A researcher interested in developing a microparticle magnetophoretic system for drug delivery might naïvely assume, given the drag coefficients of a rod and a sphere, that a spherical particle would provide the most mobile delivery platform. Biological materials are not, as will be shown, simply viscous fluids however and the best choice of particle size and shape for a practical magnetophoretic application is not necessarily obvious. The comparison of the magnetically driven velocities of the rods and the spherical beads in both model viscous and non-Newtonian biomaterial in this investigation is motived by this question.

Theoretical Driven Velocity as a Function of Particle Shape

To be able to compare the magnetically driven velocities of particles based on differences in their shapes, it is important to assume that all of the particles have the same magnetic driving force applied. This can be accomplished by assuming that all of the particles have the same magnetization and experience the same magnetic field gradient. A convenient way of thinking about such particles which have the same magnetization is to assume that they are composed of the same material, are of equal volume, and are in the same position relative to a magnetic source.

As previously described, the magnetically driven velocity of a particle V_{part} is proportional to the inverse of the particle's drag coefficient $1/\gamma$ according to equation 3.0.

$$-v_{part} = \frac{F_{mag}}{\gamma_{part}} \qquad \text{Equation 3.0}$$

The theoretical magnetically driven velocities of a rod and a sphere having the same magnetization and under the same applied field gradient in a viscous fluid can therefore be compared through the drag coefficients of the particles. The theoretical velocities have been plotted for a one micron sphere and volume equivalent rods having a range of aspect ratios in figure 3.0. The drag on a sphere was calculated according to the Stokes' law relationship in equation 1.4 and the drag on a rod according to equation 3.8, which will discussed in detail later in this chapter. It is obvious from the figure that a sphere has less drag than a rod in a viscous medium, and therefore that the sphere will have a greater magnetophoretic velocity than a rod regardless of the aspect ratio of the rod.

This simulation of the relative mobilities of a sphere and a rod is relevant in considering the influence of particle shape on the mobility of a realistic magnetically driven particle. The simplicity of the mobility relationships between a sphere and a rod in a viscous medium can be misleading when considering applications of magnetophoresis in biological media however.

Karo as a Model Viscous Fluid

In order to recognize the relevance of the results of this investigation to practical applications of magnetophoresis it will be necessary to discuss the justification for the choice of the media and the particles which were utilized in this study. Karo syrup is a purely viscous fluid and was therefore an excellent medium in which to correlate the magnetophoretic mobility of the particles in terms of quantifiable parameters of the magnetophoretic system. The quantification of the relevant mobility parameters of the rods and beads in Karo then enabled the investigation of the driven mobility of the particles in entangled polymer networks.

Karo syrup, or simply Karo, is a commercially available and inexpensive concentrated aqueous solution of sugars derived from corn starch. This aqueous composition of Karo was advantageous in the investigation. Organic media may swell or dissolve polymer particles such as the MyOne beads used in the investigation, thereby changing their properties in an unpredictable manner. Non-aqueous media would therefore not have been compatible with the polymer beads used in this study. Many of the applications of magnetophoresis are currently, and will likely continue to be, in biological science where the media is water based. It was therefore desirable to remain consistent with the practical applications of magnetophoresis through the use of aqueous media in this investigation.

Karo has been shown to resist shear thinning over the range of shear rates potentially encountered in these driven particle experiments. As the viscosity of Karo is constant within the experimental parameters, the quantification of the magnetic force on the particles from the particle mobilities in Karo was possible. The Karo used in this investigation had an average measured viscosity of 3.4 ±0.1 (Pa sec) as determined through the use of a Bohlin Gemini cone-and-plate rheometer at 23^{o}C. The viscometry measurements of Karo were performed using a range of input stresses and resulted in creep compliance curves with a consistent slope for all replicate measurements. (Jeremy Cribb, unpublished results)

The viscosity of Karo was of the appropriate order of magnitude for use in the driven particle mobility experiments. The viscosity permitted a useful translation of the particles in a reasonable experimental timescale given the particle characteristics and the applied field conditions. Media which are orders of magnitude different in viscosity would not have suited the experimental requirements. For example, the velocity of the particles in water was too great which made it experimentally challenging to obtain mobility data on multiple particles from a single sample preparation. The use of a significantly more viscous fluid, such as pitch[9] for example, would have challenged realistic experiment time constraints.

The investigation of the driven mobility of the particles in Karo served as a good basis for quantifying the magnetophoretic parameters of the system in a medium with a known and constant viscosity. Many magnetophoretic separations applications are performed in water and as such the results of the quantification of the particle mobility in Karo are directly applicable to such techniques. Closing the loop through the correlation of the quantized magnetophoretic parameters of the applied field and the particle characteristics with the driven particle mobility should serve as a guide for the design of future systems. Many of the developing bioscience applications of magnetophoresis are not set within the context of such a simple medium as a viscous fluid however. This is particularly true for biomedical applications which will require the manipulation of particles in complex biological media.

Entangled Polymer Networks as Model Biomaterials

Biological media such as cytoplasm, the extracellular matrix (ECM), and tissues are complex and variable multicomponent materials. Because of the wide variability in biological materials, it is difficult to describe the structure of a biomaterial in general terms. A common characteristic of many biological materials however is the existence of macromolecular microstructures with inherent length scales. These microstructures exist within and between cells. In addition to the many organelles within the cytosol of a cell, eukaryotic cells contain within the cytoplasm a mesh of filamentous proteins such as actin, microtubules, and intermediate filaments which form the cytoskeleton.[10]

The ECM is an interstitial fluid present between the cells in a tissue. The ECM serves to hold cells together and provides a medium through which intercellular transport and communication can occur. The ECM is a gel-like fluid made of macromolecules such as glycosaminoglycans, proteoglycans, collagens, elastin, fibronectin, laminin, and structural glycoproteins which form a mesh like microstrucure.[10, 11] The boundary of the ECM is formed by the web like lattice of the basement membrane. The basement membrane is composed of laminin and collagen fibers and serves to support the overlying endothelial and epithelial cells.[12]

To develop a better understanding of the practical magnetophoretic mobility of particles in a biological medium, a more realistic and thus a more complex model than a viscous fluid must be employed. Solutions such as Karo are homogeneous down to the nanometer scale and are therefore of limited utility as a model for understanding the length scale dependant interactions of translating particles with the microstructure of biological media. An entangled network of linear polymers would more realistically model the microstructure present in biomaterials than Karo. An entangled polymer network has pores created by the intersections of individual polymer strands. The average size of the pores, also known as the mesh size is defined as the average distance between intersections of filaments in the polymer network. The mesh size is dependent on the concentration of polymer filaments, the length of a filament, and the rigidity of the filaments.[13]

DNA as an Entangled Polymer Network

Aqueous solutions of double stranded λ-DNA (lambda DNA) were used as a model entangled polymer network for the investigation of the driven particle mobility in biologically relevant media. λ-DNA is a commercially available product isolated from Escherichia coli infected with the bacteriophage Enterobacteria phage λ (lambda phage).[10] The DNA had a contour length of approximately 15μm, and a persistence length of 50 nm.[14, 15] It contains 48,502 bases per strand which corresponds to a length of approximately 16 μm, assuming an average length of a nucleotide equal to 0.34 nm.[16]

Solutions of DNA have several advantages over other polymer solutions as model entangled polymer networks. Since DNA is a biopolymer it has immediate relevance to other biological media. The aqueous nature of the DNA solutions maintains this fundamental characteristic of biomaterials. There is a high degree of monodispersity of the polymer lengths in the DNA solutions unusual in many synthetic polymers. While many biopolymers are more rigid than DNA, sometimes having persistence lengths on the order of microns, the persistence length of DNA is greater than many synthetic polymers which might otherwise be suitable for the investigation.[17]

The terminal 12 bases at the 5’ and 3’ ends of the DNA were unpaired as shown in figure 3.1. The high concentrations at which the DNA was shipped resulted in these unpaired bases at the terminal ends of the dsDNA hybridizing with either their opposite ends, or with the ends of other DNA strands. The end-to-end hybridizations resulted in the individual DNA strands forming interconnected geometries.

The interconnected structure of the DNA solution as supplied was undesirable for use as a medium in this investigation due to the unknown in homogeneity of these structures in the solution and the polydispersity of the effective lengths of the polymers. In order to obtain a monodispersed solution of free linear DNA filaments, the end-to-end associations of the polynucleotides were disrupted and the ends of the

DNA were blunted with short 12 base oligonucleotides, preventing the re-association of the individual DNA strands.

There are several concentration regimes of DNA solutions which determine the microstructrue of the medium. At the critical concentration C* individual DNA filaments are just touching but do not form an entangled network. C* forms the lower concentration of the semi dilute un-entangled regime. The entangled concentration C_e is the lower concentration limit of the entangled regime and is approximately ten times greater than C*. At C_e the DNA solution forms an entangled mesh with the greatest possible mesh size.[13] The two concentrations of DNA solutions, used in this investigation, 0.7 and 2.0 mg/mL, were both within the entanglement regime thus enabling the comparison of the particle velocities in the two concentrations.

Choice of Probe Particles

The MyOne beads and the nickel rods were chosen based on a number of unique characteristics of the particles. Because of their large magnetic susceptibility, the particles developed a large magnetization under the applied magnetic field conditions used in the mobility study. The large magnetization of the particles imparted a sufficiently great magnetically driven mobility to obtain a satisfactory driven translation in an experimentally reasonable time. This was important to provide a driven mobility that was significantly greater than the diffusive mobility thus enabling an adequate signal-to-noise ratio of the measurements.

Both types of particles were well dispersed in the media and remained as stable suspensions over the course of the experiments. The particles were small enough and their velocities were low enough as to enable the low Reynolds number assumptions discussed earlier. The ability to invoke these assumptions enabled the convenient determination of magnetic force directly from the particle velocity measurements. The particles were large enough to allow them to be imaged using a standard microscope however. In addition, the micron scale of the particles was comparable to the dimensions of particles utilized in other magnetophoresis applications and research investigations.[4, 18-20]

The physisorption of DNA onto the particles from solution could dramatically influence the mobility of the particles in the DNA solutions by increasing the particle dimensions in an unpredictable manner thereby and confounding the results. The surface chemistry of the particles inhibits the absorbtion of DNA however. The MyOne beads were chemically functionalized with carboxy surface groups, as obtained from the manufacturer. This surface functionalization imparted a negative surface charge to the beads in the aqueous media.

The surface of the nickel rods would be expected to be slightly oxidized due to processing forming a surface layer of nickel oxide. The metal oxide layer would also impart a negative surface charge to the rods.[21, 22] The negative surface charge of the beads and the rods was an advantage in the use of DNA solutions as transport media. Due to the phosphate backbone, DNA has a net negative charge. The negative surface charge of the particles and the negative charge of the DNA would be expected to inhibit the physisorbtion of DNA onto the particles.

To be able to reliably determine the magnetic forces on the particles, and therefore to be able to compare their mobilities from velocity measurements, it was necessary to know the physical dimensions of the particles. The MyOne beads were very symmetric and highly monodispersed. These characteristics enabled the convenient averaging of the mobilities of many beads in order to determine the driven mobility under particular magnetophoretic conditions. Without this high degree of similarity between individual beads, the mobility of each particle would have needed to be assessed independently.

The diameters of the rods were known due to the manner in which they were synthesized. The diameters of the nickel rods were constrained by the 200 nm pore diameter of the AAO membrane in which they were synthesized. Because the pore diameter of the membrane had a low variability, it was a reasonable assumption that there was not a great rod-to-rod variation in the diameter. The length of the rods varied due to breakage during processing however requiring the individual measurement of each rod from the video data.

Choice of Magnetic Field Source

A permanent magnet was used to apply the magnetomotive force to the MyOne beads and rods. This type of magnetic source was chosen in part due to the ability to empirically characterize the magnetic field of a macroscopic magnet. Since many analytical and biomedical magnetophoretic applications might utilize a permanent magnet, the use of a similar magnetic source also serves to maintain the relevance of this investigation to practical magnetophoretic applications.

The most straightforward technique of characterizing a magnetic field is to measure the field magnitude using a Gaussmeter. A Guassmeter uses a Hall probe sensor to measure magnetic flux. The sensor of the Hall probe contains an indium compound crystal to which a current is applied. When placed in a magnetic field, a Hall Effect voltage develops across the crystal serving as a measure of the magnetic flux density.[23]

While the magnitude of the magnetic field is relevant to the magnetization of a particle according to its susceptibility, the gradient of the field is also relevant to the magnetic force applied to the magnetized particle. By taking multiple measurements of the field magnitude as a function of distance from the magnetic source, the magnetic field gradient can be quantified. Since the probe measures the magnetic flux through the crystal, the spatial resolution of the field gradient measurement is inherently related to the size of the Hall probe. This makes it difficult to accurately characterize a magnetic field with a large gradient using a standard Gaussmeter. To permit the characterization of a magnetic field by direct measurement of the field using a Gaussmeter, a magnetic source of macroscopic physical dimensions and consequently small field gradient was required. A permanent magnet meets these requirements having a field which can be well characterized directly using a Gaussmeter.

The use of a macro scale magnet, having a small field gradient, as a magnetic source for magnetophoresis resulted in a commensurate decrease in the magnetophoretic force applied to the particles. In order to compensate for the smaller magnetophoretic force resulting from the small field gradient, a magnet having a large magnetic field was also required. A permanent rare earth magnet, having a large magnetic field but a small field gradient, fulfilled the experimental requirements by enabling the application of a large magnetic force while applying only a modest field gradient. The large susceptibility of the MyOne beads and nickel rods enabled the application of a useful magnetomotive force without applying a large field gradient.

The magnetophoresis experiments using the MyOne beads and nickel rods were performed using a strong, neodymium iron boron (NdFeB) cylindrical permanent magnet. The shape of a cylindrical magnet was chosen because the field is homogeneous radially outward from the long axis, with the greatest field gradient along this axis. This field geometry provided a simple gradient along the axis in z which enabled the straightforward mathematical description necessary for the calculation of the theoretical magnetic force on the particles.

The theoretical magnetic force on the MyOne beads and rods was calculated and compared with the observed magnetic force applied to the particles. In order to calculate the theoretical magnetic force, the magnetic field and the field gradient as a function of distance needed to be determined for the specific permanent magnet which was used in the study.

Experimental

Magnetic Field Characterization

The magnitude of the magnetic field of the permanent magnet was measured as a function of axial distance from the face of the magnet using a digital W. Bell

Gauss/Teslameter Model 5080. The previous manufacturer’s calibration of this Gaussmeter was not more than 60 days prior to taking the measurements assuring that the instrument was functioning properly. The measurement of the field as a function of distance was accomplished by fixing the position of the magnet and the mounting the Gaussmeter Hall probe on a calibrated translation stage. This enabled the measurement of the field at precise distances axially from the face of the magnet. It was assured that the correct side of the probe tip was toward the magnet, and that the probe surface was parallel to the face of the magnet at all times.

The field measurements were performed far from potential sources of stray magnetic fields such as electrical equipment and other magnetized objects. The Gaussmeter was set to DC mode, and to automatically adjust the measurement scale in order to obtain the most accurate reading of the field magnitude as the distance was changed. The background signal of the Gaussmeter was reset immediately prior to taking the field measurements by placing the probe in a zero field cavity and zeroing the meter according to the manufacturer’s instructions.

The zero distance position of the field as a function of distance measurements was determined by noting the probe position which resulted in the maximum field magnitude reading, as well as visually confirming that the probe tip was in contact with the face of the magnet. Magnetic field measurements were taken from this zero distance point at approximately 1 mm intervals to a distance of 18 mm from the face of the magnet as shown in figure 3.3. Figure 3.4 is a plot of the field measurements in Tesla as a function of the distance from the face of the magnet in meters. The shaded box represents the experimentally relevant distance range.

Using calipers the physical dimensions of the permanent magnet were measured to be 1.00 inch (25.4 mm) long and 0.15 inches (3.81 mm) in diameter. Rare earth magnets of this type are fragile and are coated with a protective metallic layer. It was therefore not possible to measure the actual dimensions of the magnet itself. Consequently the measured physical dimensions of the magnet are not exactly the same as the dimensions of the magnetic material but represent the maximum dimensions.

The thickness of the protective coating on similar magnets was not greater than 0.5 mm. This was determined by breaking a disc magnet and measuring the thickness of the protective metallic layer. Therefore 0.5 mm was be taken as a reasonable estimate of the maximum coating on the cylindrical magnet used. The maximum magnetic field B_{max} was measured using the Guassmeter at the face of the magnet as 0.3545 T. This maximum field however was never experienced by the particles in the sample.

DNA Preparation

DNA Ligation

The λ-DNA used for this investigation was obtained from Invitrogen in concentrations of approximately 500 μg/mL.[16] The DNA was stored in a buffer composed of 10 mM Tris-HCl (pH 7.4), 5 mM NaCl, and 0.1 mM EDTA. Short oligonucleotides used for blunting the ends of the DNA were obtained from the UNC Oligonucleotide Synthesis Core Facility.[24] These were dissolved in Tris buffer of the same composition as the DNA storage buffer. The λ-DNA was available from the supplier as a double stranded polynucleotide (dsDNA) 48kb in length.

The stock DNA media were prepared by adding the individual aliquots of DNA as obtained from the manufacturer together to form a single stock DNA sample. The DNA was then melted by heating the sample at 65^{o} C for 15 minutes resulting in single stranded DNA. Either the 3’ or the 5’ end of the single stranded DNA was then blunted by ligating the DNA with of one of the two oligos, 5’-GGG CGG CG ACCT-3’ or 5’-AGG TCG CCG CCC-3’, which were complimentary to the unpaired bases at the ends of the DNA. Figure 3.1 illustrates the ligation sequence starting with the unblunted double straqnded DNA. The 12 base oliga is then ligated to the DNA which prevents the re-hybridization of the ends of the DNA.

The blunted DNA sample was then allowed to cool slowly to permit re-hybridization. The blunted DNA was purified and concentrated by an ethanol and salt precipitation at -20^{o}C followed by high speed centrifugal sedimentation. Following the precipitation and sedimentation, the concentration of the DNA sample was measured by UV absorbance at 260 nm using the extinction coefficient of DNA equal to 0.02 mL/μg cm.[25]

DNA Particle Suspension Preparation

Suspensions of MyOne beads and rods were prepared in Tris DNA buffer at low particle concentrations. Concentrated DNA was diluted to the desired working concentration of either 0.7 mg/mL or 2 mg/mL using the either the rod or MyOne particle suspension. The particle suspensions were vortexed or sonicated prior to diluting the stock DNA in order to improve the final dispersion of the particles in the DNA solution. Shear damage to the DNA by mixing could alter the monodispersity of the DNA lengths and was a concern in the preparation of the particle dispersions. Diluting the stock DNA to the appropriate working concentration using the low concentration particle suspensions was advantageous in obtaining adequate dispersions of particles in the DNA solutions with limited mixing of the sample.

Particle-particle and particle-surface interactions, such as with the coverslips or the PDMS well, would have a deleterious influence on the measurement of the magnetophoretic mobility of the rods and the MyOne beads. Care was therefore taken to assure that mobility data was taken only for individual particles which were far from other particles and from surfaces.

Karo Particle Suspension Preparation

Suspensions of nickel rods and non-magnetic control beads or MyOne beads in Karo were made by carefully mixing a small volume of particles suspended in water into the Karo using a disposable pipette tip. The addition of the aqueous particle suspension served to dilute the Karo by less than 0.5%. It has been demonstrated by researchers in our lab that this level of dilution does not result in a measurable change in the viscosity of Karo (unpublished results).

The concentration of the rods in the Karo was adjusted in order to assure that the rods were greater than 100 μm away from one another when observed in the experimental apparatus. Maintaining this low concentration of rods limited potential magnetic dipole-dipole and physical interactions between particles. Non-magnetic one micron diameter polystyrene control beads (obtained from Polysciences) were dispersed in the samples along with the rods in order to enable global hydrodynamic drift subtraction from the magnetically driven particle velocities. The concentration of the control beads was adjusted so that each driven rod video data set contained at least 10 control beads in the field of view.

Sample Chamber

A microfluidic sample chamber was constructed from polydimethylsiloxane **(**PDMS) and two glass coverslips. A thin sheet of PDMS was made by mixing the polymer and curing agent in a 10:1 ratio and spin coating a small volume into a disposable Petri dish. The PDMS was cured at 50^{o} C overnight. The resulting thin film was measured to be approximately 150 μm thick. A small square roughly 3 mm x 3 mm was cut out of the PDMS sheet using a razor blade. A round hole 1.5 mm in diameter was punched in the square PDMS sheet using a stainless steel tube sharpened at the edge. The small PDMS square was cleaned with ethanol and water and then blown dry with nitrogen. The square was contacted to a clean 24 mm x 50 mm, number 0 coverslip, which immediately formed a tight seal with the glass surface. The diameter of the sample well was narrower than the width of the magnet which served to minimize the variation of the magnetic field laterally within the sample chamber.

The sample well formed by the PDMS sheet and the cover slip was filled with approximately 2 μL of the sample. Care was taken to avoid over filling the well. A clean 22 mm x 22 mm, number 0 coverslip was carefully sealed to the top of the PDMS square. Once the sample chamber was filled and sealed, the sample was allowed to settle for at least ten minutes before applying any magnetic field. This quiescent period allowed most of the global hydrodynamic migration of the particles caused by filling the sample chamber to cease before particle mobility data was collected.

Magnetophoresis Apparatus

The experimental apparatus used for the magnetically driven particle mobility quantification consisted of an inverted microscope, a video camera, and a permanent magnet attached to a translation stage for the application of a variable magnetic force to the particles as shown in the photo in figure 3.5 and the schematic in figure 3.6. The entire experimental apparatus was mounted on a floating optics table for vibration isolation. Images of the sample were captured in brightfield mode using a x20 objective, a Pulnix video camera, and a PC workstation. The microscope optics were spatially calibrated by recording an image of a reticule slide. The spatial length in the image was calibrated with respect to the pixel length using Adobe Photoshop software. The pixel to micron ratio of the video images was used to convert the particle displacement to a practical distance displacement and to measure the length of individual rods. A spring loaded translation stage was used to adjust the axial position of the permanent magnet with respect to the sample. A series of spacer blocks were used to axially translate the magnet to preset distances from the sample. The magnet was mounted on a non-magnetic (aluminum) translation arm attached to the translation stage which enabled the close approach of the magnet to the sample.

Prior to the collection of each particle magnetophoresis data set, the zero position of the magnet was re-calibrated. The magnet was horizontally extended above the sample stage and into the frame of view of the video camera by removing the spacers from the translation stage. The focal plane of the microscope was adjusted so that the center (axis) of the face of the magnet was in focus. Fine adjustments were then made to the position of the translation arm in order to axially move the magnet as to bring the leading edge of the magnet to the center position of the field of view in the video image. This calibration assured that the zero distance point of the magnet was at the center of the field of view prior to the collection of each particle mobility data set.

Particle Magnetophoresis

At the start of each experiment, the sample cell was positioned by eye so that the center of the sample chamber was in line with the axis of the magnet and equidistant from the edges of the magnet. The video capture frame rate and the duration of the data collection were adjusted according to the mobility of the particles. For example, slower moving particles were captured at a slower frame rate and for a longer period of time. The driven mobility of the MyOne beads and rods were recorded over a range of applied magnetic forces by axially moving the permanent magnet, mounted on a translation stage, to one of multiple preset distances from the sample using a series of spacer blocks.

The magnetophoretic mobility data collection began with the magnet at the farthest distance from the sample, with all the spacers in place. Each magnetophoretic mobility data set was bracketed by two zero field drift data sets as will be described in detail later. After the collection of the second drift data set the magnet was translated one interval nearer the sample by removing a spacer from the translation stage spring mechanism. If the particle had moved significantly from the center of the field of view over the course of the previous data collection, it was re-centered in the field of view prior to the next data collection by making fine adjustments to the sample position as needed.

Drift Control Data Collection

While every effort was taken to eliminate macroscopic drift in the sample by appropriately filling the sample well, effectively sealing the PDMS to the coverslips, and incorporating a settling time, some non-magnetophoretic particle drift was unavoidable. The non-magnetic control beads present in the rod samples were utilized in order to enable the removal of the non-magnetophoretic drift from the driven rod mobility data. Magnetically driven particle video data sets were taken by positioning the permanent magnet at preset distances and imaging the sample. For each driven mobility data set, two drift control data sets with no applied magnetic field were taken, one before and one after the magnetically driven data set. For these two drift data sets the magnet was withdrawn axially then rotated on the translation arms far away from the sample. There was no magnetic field detectable at the sample using the Hall probe with the magnet in this position. By axially withdrawing the magnet from the sample first, the application of rotational torque to the rods which could disturb the sample was avoided.

Particle Tracking

The position of the rods and beads were tracked post-capture using Video Spot Tracker software developed in house as part of the 3DFM analysis package (courtesy of Russell Taylor, et al). The Video Spot Tracker returns temporally correlated X and Y ordinate positions for particles tracked in video. The net displacement in units of pixels per second was then calculated for the particle. The tracked data was converted to a Matlab file using a file conversion developed in house (courtesy of Jeremy Cribb, et al). The resulting Matlab file was read by the Edit Video Tracking Graphical User Interface (EVT GUI) software (courtesy of Jeremy Cribb, et al) which allowed graphical editing of the data set. A linear fit to the rod displacement was used to calculate the ordinate components of the rod displacement in the driven data sets.

Drift Subtracted Velocity

In order to determine the drift velocity for each zero field data set, the center of mass (COM) displacement of the vector displacements of the individual control beads was calculated using the EVT GUI software. The ordinate components of the COM displacement for the drift data before and after the bracketed driven mobility data set were averaged. The average X and average Y COM displacements of all the tracked control beads in the drift data sets taken before and after the driven data set were then subtracted from the corresponding driven particle ordinate displacements in order to return the drift subtracted ordinate velocities $V_{X_{DriftSub}}$, $V_{Y_{DriftSub}}$. These velocity values were then used to calculate the net driven particle velocity according to equation 3.1.

$$V_{DriftSub} = \left[\left(V_{X_{DriftSub}} \right)^2 + \left(V_{Y_{DriftSub}} \right)^2 \right]^{1/2}. \qquad \text{Equation 3.1}$$

The standard deviation between the ordinate COM displacements ($\sigma_{X,}$ σ_Y) of the two drift data sets which bracketed the driven data were used as the uncertainties in the ordinate particle displacements. The drift subtracted particle velocity $V_{DriftSub}$ was converted from pixels/second to microns/second using the previously discussed calibration ratio in order to obtain a practical particle velocity in units of meters per second.

The uncertainty in the particle drift subtracted velocity (σ_V) was used to calculate the uncertainty in the measured magnetic force applied to the particles. σ_V was calculated according to equation 3.2 where the partial derivatives of V are defined in equations 3.3 and 3.4.

$$\sigma_V = \left[\left(\frac{dV}{dx} \right)^2 \sigma_x{}^2 + \left(\frac{dV}{dy} \right)^2 \sigma_y{}^2 \right]^{1/2}$$ Equation 3.2

$$\frac{dV}{dx} = 1/2 \left[\left(V_X\right)^2 + \left(V_Y\right)^2 \right]^{-1/2} \cdot 2V_X$$ Equation 3.3

$$\frac{dV}{dy} = 1/2 \left[\left(V_X\right)^2 + \left(V_Y\right)^2 \right]^{-1/2} \cdot 2V_Y$$ Equation 3.4

Magnetic Force Uncertainty

Due to the broad distribution of the particle velocities, and the necessity to normalize the driven velocities of the particles in order to enable their comparison, care was taken to track the propagation of error in the calculations leading to the normalized mobility values. Through the propagation of error calculations it was determined that the distribution in the final mobility values were not due to propagation of measurement error. The calculations showed that the error due to the uncertainty in the length measurements of the rods was small compared to the rod to rod variation of the magnetic force. The variation of magnetic force on the rods was therefore a function of differences in the magnetic properties of the rods themselves. The fabrication of the rods involved the dissolution of the membrane template using a strongly oxidizing solution of concentrated sodium hydroxide as described previously. This is likely to have produced a variable surface oxide layer on the rods resulting in a rod-to-rod variation in the magnetic properties.

Results and Discussion

The discussion of the results of the magnetophoretic experiments described in this chapter is composed of two sections. First the results of the driven particles studies in Karo were used to calculate the forces applied to the particles by utilizing the measured particle velocities, the measured drag coefficients of the particles, and the measured viscosity of the Karo. These measured forces were compared to the forces theoretically predicted. The applied magnetic forces measured for the particles in Karo were then used to study the driven mobility of the particles in the DNA solutions. Each of these sections will now be discussed in detail.

Magnetophoresis of Particles in Karo

The results of the magnetically driven particle experiments in Karo enabled the calculation of the magnetic force applied to the rods and beads based on the velocity measurements of the particles, the measured drag coefficients of the particles and the measurement of the bulk viscosity of the Karo. These applied forces were then compared to the theoretically predicted applied magnetic forces based on the magnetic characteristics of the particles which were measured in chapter 2 and the applied field as a function of distance from the permanent magnetic measured in this chapter.

To predict the force on the particles as a function of their distance from the permanent magnet, a mathematical function which described the magnetic field as a function of the axial distance from the magnet face was calculated based on the magnetic field measurements. The comparison of the theoretically predicted magnetic forces applied to the MyOne beads and the nickel rods with the magnetic forces calculated from the measured velocities are compared in figures 3.7 and 3.8 respectively. This comparison between the measured forces with the forces predicted based on the characteristics of the whole magnetophoretic system serve to close the loop between theory and observation.

Calculation of Magnetic Force from Particle Velocitometry

The magnetophoretic forces F applied to the driven particles in Karo were calculated using the drift subtracted velocity and the drag coefficients (γ) of the particles in Karo according to equation 3.5.

$$F = -\gamma V \qquad \text{Equation 3.5}$$

As the particle velocity measurements used will always be the drift subtracted particle velocities as described previously, they will henceforth be referred to simply as the velocity (V) values. Due to the high degree of monodispersity of the MyOne beads, the determination of γ was universally applicable to all of the MyOne beads. The determination of γ for the nickel rods was more involved however due to the lack of length uniformity of the particles. This required the calculation of individual drag coefficients for each rod based on the measured length of the rod.

Determination of MyOne Drag Coefficient in Karo

The drag coefficient for the MyOne beads, given by the Stokes' equation for drag on a sphere in a viscous medium, is given by equation 3.6 where η is the viscosity of Karo and r is the bead radius.

$$\gamma_{sphere} = 6\pi\eta r \qquad \text{Equation 3.6}$$

The viscosity of the Karo was measured to be 3.4 Pa sec (unpublished data Cribb) as previously described, and the radius of a MyOne bead was 525 nm as confirmed by electron microscopy. Using these values, the drag coefficient of a MyOne bead in Karo was calculated according to equation 3.7.

$$\gamma_{MyOne} = 6\pi\eta r = 6\pi\left(3.4 Pa \cdot s\right)\left(5.25 \cdot 10^{-7} m\right) = 3.4 \cdot 10^{-5} Pa \cdot s \cdot m \qquad \text{Equation 3.7}$$

Determination of Rod Drag Coefficients in Karo

Measuring Rod Length

To calculate γ_{rod} for the driven rods in Karo, the dimensions of the each rod needed to be measured. The rod diameter however was known to be 200 nm as dictated by the pore size of the AAO membrane. Most rods which were observed were shorter than the original fabrication length of 38 μm due to damage during sample processing. The length of each driven rod was therefore measured from the video data extracting single frames from each of the driven data sets using a Graphical User Interface (GUI) developed in house (courtesy of Jeremy Cribb). From this single frame, the length of the rod L was measured in the number of pixels using Adobe Photoshop software. The rod length in units of pixels was then converted to microns using the pixel to micron conversion ratio discussed previously.

Since multiple video files were taken for each rod, corresponding to different positions of the magnet, a single frame was extracted from each video file and the length of the rod in that frame was measured as described. For example, if five video files were recorded for particular rod corresponding to five magnet positions (five different applied field conditions), a single frame was extracted for each video file resulting in five images of the rod from which to measure the length. The length of the same rod was measured in all five images and the values of L for all images extracted for the same rod were averaged. The average length of the rod was used for all future calculations of that rod. The uncertainty in the length measurement σ_L was taken as the standard deviation of the five length measurements.

Calculating Rod Drag Coefficient from Measured Lengths

The rod drag coefficient for the axially translating rods in Karo is given by equation 3.8 where a = radius (100 nm), L = length, η = viscosity of Karo, and $\nu_{||}$ = - 0.19.[26]

$$\gamma_{RodKaro} = \frac{2\pi\eta L}{\ln(\frac{L}{2a}) + \nu_{||}} \qquad \text{Equation 3.8}$$

The variable $\nu_{||}$ in equation 3.8 is an end correction for a cylinder translating with its easy axis parallel to the velocity. The end correction $\nu_{||}$ is dependent on the aspect ratio of the rod with larger values corresponding to smaller aspect ratios. The length of rods used in these experiments were on the order of 10 μm, and as such the end correction value of -0.19 was used for $\nu_{||}$ as described by Tirado et al. Utilizing these values the drag coefficient of an axially translating rod in Karo was calculated as a function of rod length according to equation 3.9 and the uncertainty in $\gamma_{RodKaro}$ was calculated from σ_L.

$$\gamma_{RodKaro} = \frac{2\pi\eta L}{\ln(L) - \left[\ln(200nm) + (-0.19)\right]} = \frac{\left(21.36\left(Pa\cdot s\right)\right)\cdot L}{\ln(L) + 15.62} \qquad \text{Equation 3.9}$$

Normalization of Magnetic Forces for All Rods

The magnetic driving forces and drag forces acting on a magnetically driven rod are proportional to the geometric dimensions of the rod. The greater the volume of the magnetized rod, the larger the magnetic moment and thus the greater the magnetophoretic force. The drag experienced by the rod also increases with the size of the rod. In order to compare the net force applied to different rods of different lengths and consequently different volumes, the observed force was normalized with respect to *L*. This was accomplished by dividing the magnetic force on each rod by the length of the rod in microns according to equation 3.10.

$$\frac{F}{L(\mu m)} = \frac{-\gamma v}{L(\mu m)} \qquad \text{Equation 3.10}$$

Based on the measured drag coefficients for the particles, as described above, the applied magnetic forces on the particles in Karo were then calculated from the measured particle velocitometry data.

Calculation of Magnetic Field as a Function of Axial Distance

In order to calculate a theoretical magnetophoretic force on the particles, it was necessary to determine the mathematical function which described the axial magnetic field and the axial field gradient of the permanent magnet. The magnetic field *B* as a function of distance axially z from the face of a cylindrical magnet is described by equation 3.11 where M_s is the saturation magnetization of the magnet, L is the length of the magnet, and R is the magnet's radius.

$$B(z) = \frac{M_s \mu_0}{2}\left[\frac{-z}{\sqrt{z^2+R^2}} + \frac{L+z}{\sqrt{(z+L)^2+R^2}}\right] \qquad \text{Equation 3.11}$$

The function of the magnetic field of the magnet as a function the axial distance was calculated by fitting equation 3.11 to the field versus distance data in figure 3.4 using the Origin software package. The variables of the fit were based on the measured physical dimensions and the maximum field of the magnet. In order to achieve the best agreement between the fit and the experimental conditions, the fit was performed over the z range which was relevant to the particle magnetophoresis experiments corresponding to 3 to 10 mm as plotted in figure 3.4 B.

The fit of equation 3.11 to the field versus distance data resulted in a R^2 value of 0.99. The fit determined values of the magnetic saturation M_s and the radius of the magnet R were in agreement with the measured values of the magnet within the fit uncertainties. The fit determined variable corresponding to the length of the magnet L was not in agreement with the measured length of the magnet however. Constraining all of the fit variables to the empirically determined physical characteristics of the permanent magnet resulted in a poor fit to the data. The fit routine was therefore performed with M_s and R constrained to the measured values but with L allowed to vary in order to obtain the best fit. A more in depth description of the fitting process and results is set out in appendix 7.

The gradient of the field axially in *z* was determined simply by taking the derivative of the equation of *B(z)* with respect to *z* according to equation 3.12

$$\frac{dB(z)}{dz}=-\frac{M_s\mu_0}{2}\left[\frac{-z^2}{\left(z^2+R^2\right)^{3/2}}-\frac{1}{\sqrt{z^2+R^2}}-\frac{\left(L+z\right)^2}{\left(\left(z+L\right)^2+R^2\right)^{3/2}}+\frac{1}{\sqrt{\left(L+z\right)^2+R^2}}\right] \qquad \text{Equation 3.12}$$

The values of the variables M_s, L, R as determined through the fit process were then used to calculate the gradient of the field of the permanent magnet as a function of *z*. This functional form of the field gradient in *z* will be used later for the calculation of the theoretical magnetophoretic forces on the particles.

Theoretical Magnetic Forces on Beads and Rods in Karo

The theoretical magnetic force applied to the particles as functions of the distance from the permanent magnet were calculated using the measured magnetic susceptibility of the particles, the measured applied magnetic field, and the magnetic field gradient as derived from the field versus distance data as described. The functions which were calculated for the theoretical forces on individual MyOne beads and rods were plotted (solid lines) as functions of the distance from the permanent magnet in figures 3.7 and 3.8 respectively. Upper and lower uncertainties of the theoretical forces were calculated using the uncertainties of the fit parameters. These functions were plotted as the upper and lower curves (dashed lines). Because of the complex nature of the calculations they were performed using the Mathematica software package. The measured magnetic forces were also plotted in these figures as will be discussed next.

Magnetic Force on Particles as Measured in Karo

The average magnetophoretic velocities of the MyOne beads and rods in Karo were measured as functions of the distance from the permanent magnet as described in the experimental section. The magnetic force which was applied to the MyOne beads in Karo was calculated from the measured average velocity data using equations 3.0 and 3.7 and plotted along with the theoretically predicted force in figure 3.7. The bars on the data points in the figure do not represent error in the measurements but rather indicate the distribution of velocities resulting from differences between individual particles. The magnetically driven mobility measurements of the MyOne beads had a low variability with a standard deviation of less than 10% as determined through equation 3.4.

The length normalized magnetic force which was applied to the rods in Karo was calculated from the measured average velocity data using equations 3.9 and 3.10 and plotted along with the theoretically predicted force in figure 3.8. As was true for the MyOne beads, the bars on the data points represent uncertainty derived from the distribution of magnetic forces attributed to rod-to-rod to variation in physical properties of the particles. While it was not possible with the instrumentation employed in this investigation to measure the magnetic properties of individual particles to establish an empirical distribution of the magnetic properties, it is proposed that rod-to-rod variation in the domain structures of the particles would lead to a variation in the magnetic properties. It is reasonable that the synthesis and processing of the rods may have resulted in a variable degree of oxidation of the nickel rods. Differences in the oxidation of the rods would naturally result in differences in their magnetization, with a greater oxidation corresponding to a lower magnetization. Consequently differences in oxidation between the rods would result in a distribution of the magnetophoretic mobilities of the rods. While care was taken to only collect data for rods which appeared linear and undamaged, variation in the surface roughness and small differences in the shapes of the rods which could not be measured on a rod to rod basis may have also been in part responsible for the variability in the rod velocities.

It can be seen through figure 3.7 that the magnetic force applied to the MyOne beads as calculated from the velocitometry measurements agrees with the theoretically predicted force based on the quantified characteristics of the magnetophoretic system. While the MyOne force values are slightly greater than the predicted force the measured and theoretical forces agree within the distribution of forces on the individual particles and the theoretical uncertainties.

Similarly the forces applied to the rods in Karo, as shown in figure 3.8, are also in agreement with the theoretical force predictions. The measured magnetic forces on the rods are slightly less than the predicted forces, but agree well within the relative uncertainty. The full characterization of the relevant magnetophoretic parameters of the system enabled the measured forces to be connected to the theoretical forces. The correlation of the measured magnetic forces on the MyOne beads and the nickel rods with the forces predicted closes the loop between the theory and observation of the magnetophoresis of these investigations and represents an important first in the field of micro-magnetophoresis. The measurements of the magnetic forces applied to the particles in Karo, a medium with known rheological properties, enabled the magnetophoretic investigations of the DNA solutions as will be described in then next section of the discussion.

Magnetic Force on Particles as Measured in DNA

Figure 3.9 presents the magnetically driven velocities of the rods (represented by open squares) and the MyOne beads (represented by open circles) in the two concentrations of DNA and in Karo. Differences in the lengths of individual rods resulted in rods experiencing different magnetophoretic and drag forces. In order to compare the magnetophoretic velocities of individual rods in figure 3.9, the rod velocities were normalized with respect to the rod length. This was accomplished by dividing the velocity of a rod by the length of that rod in microns, and multiplying by the geometric component of γ_{rod}, referred to henceforth as $\tilde{\gamma}_{rod}$. For the convenience of the reader, the geometry normalized rod mobility is defined in equation 3.13.

$$\frac{v}{L(\mu m)}\tilde{\gamma}_{rod} = \frac{v}{L(\mu m)}\left(\frac{2\pi L}{ln(L)-\left[ln(2r)+v_{\|}\right]}\right) \qquad \text{Equation 3.13}$$

The MyOne beads were homogeneous and did not inherently require any normalization of their velocities, however to enable the convenient comparison of the bead velocities with those of the rods, they were similarly multiplied by their geometric drag component as defined in equation 3.14.

$$\tilde{\gamma}_{MyOne} = 6\pi r \qquad \text{Equation 3.14}$$

Particle Velocity versus $B\nabla B$ in Karo and DNA

The velocities of magnetically driven particles are directly proportional to the applied field and gradient, and as such the velocities of the particles in this investigation are presented as functions of $B\nabla B$ in figure 3.9. The values of $B\nabla B$ in the figure are representative of applied field conditions which are readily accessible using conventional permanent magnets. The presentation of the data in figure 3.9 in terms of the applied field conditions necessary to achieve a given magnetophoretic mobility enables the comparison of these data with other microparticle magnetophoretic systems. The bars on the data points represent the distribution of the velocities of the particles as previously described for figures 3.7 and 3.8. The distribution of the driven mobilities of the individual rods in the 2.0 mg/mL DNA solution was greater than had been the case in either the 0.7mg/mL DNA solution, or the Karo. The wider distribution of rod mobilities in the 2.0 mg/mL DNA likely reflects the increase in heterogeneity of the DNA solutions with increasing concentration.

Examination of the relative velocities of the particles presented in figure 3.9 reveals an interesting and unexpected phenomenonon. Comparison of the velocity values for the rods in the DNA and Karo in figure 3.9 shows that the rod velocities were greater in the 0.7 mg/mL DNA than in Karo, and less than those of Karo in the 2 mg/mL DNA. The MyOne bead velocities however show a different trend however. The bead velocities in the 0.7mg/mL DNA solutions were less than, or at most equal to, the velocities in Karo. No data were available for the beads in the 2mg/mL due to the lack of measurable displacement of the beads as previously discussed. This result was not predicted based on the simple Stokes’ and was an indication that there was a more complex and interesting mechanism.

Karo is a Newtonian fluid[27], however biomaterials can exhibit non-Newtonian rheological properties. Bulk rheology measurements of solutions of λ-DNA, such as those used in this investigation, have shown a decrease in the apparent viscosities of the media as the result of an applied shear stresses even at relatively low shear rates.[7] When an applied shear stress aligns the polymer strands in a mesh such as the DNA solutions examined here, a decrease in the apparent viscosity may be observed. The response of a material to an applied shear stress is apparent by plotting the measured (or apparent) viscosity as a function of the maximum shear rate ($\dot{\gamma}_{\max}$). The maximum shear rate of the types of particles examined here moving through a medium occurs at the surface of the particle which is at a 90^0 angle to the velocity. Equation 3.15 defines $\dot{\gamma}_{\max}$ at the surface of a sphere, where v is the particle velocity and r is the radius of the sphere.

$$\dot{\gamma}_{\max} = \frac{3v}{2r} \qquad \text{Equation 3.15}$$

Equation 3.15 served as a first order approximation of the lower limit of shear on a rod. From equation 3.15 it is apparent that because of the smaller radius of the rods compared to the beads that a bead with the same driven velocity as a rod would produce a shear rate which was five times less than that of the rod.

Because the magnetic forces applied to the MyOne beads were known as functions of distance from the magnet, the viscosities of the DNA solutions as experienced by the beads, referred to as the *apparent viscosities* (η_{app}), were able to be measured by solving equations 3.5 and 3.6 for η using the known force values. Likewise the η_{app} values of the DNA solutions as experienced by the rods were calculated by solving equations 3.8 and 3.10 for η using a known (length normalized) force. These apparent viscosities of the Karo and the DNA solutions were plotted with respect to the maximum shear rates to elucidate the phenomena apparent in the velocity data in figure 3.9.

Apparent Viscosity versus Shear Rate in Karo

The apparent viscosities of the MyOne beads (blue dots) and the rods (black squares) are plotted as functions of the maximum shear rate in figure 3.10. The bulk viscosity of Karo is plotted as a constant with a value of 3.4 Pa s. The results of plotting the η_{app} as a function of $\dot{\gamma}$ for the beads and the rods in Karo show the results expected for a Newtonian fluid. All of the data are distributed about the bulk viscosity of Karo and the apparent viscosities of the Karo as experienced by both the beads and the rods are therefore independent of the shear rates.

Apparent Viscosity versus Shear Rate in DNA

In contrast to the constant apparent viscosity of the Karo demonstrated by figure 3.10, the plot of η_{app} as a function $\dot{\gamma}_{\max}$ for the particles in the DNA solutions in figure 3.11 shows decreasing η_{app} with increasing shear rate with a power law dependence indicating shear thinning. In figure 3.11 the average η_{app} values of the MyOne beads are represented by open circles, the rods in the 0.7 mg/mL DNA solution are represented by open squares, and the 2 mg/mL DNA rod data are represented by half filled squares. In addition to the data from this investigation, bulk rheology data from other sources represented by lines has been included on the plot. The apparent viscosity values and the maximum shear rates cover a range of four decades from 10^{-2} – 10^{2} (1/s) and 10^{-2} – 10^{2} (Pa s) respectively. The η_{app} of the DNA solutions were in all cases greater than 1 $\times 10^{-3}$ Pa s corresponding to the viscosity of the DNA buffer alone as expected.

Bulk Apparent Viscosity versus Shear Rate of DNA

To aid the reader in interpreting the data in figure 3.11, bulk rheology measurements of η_{app} as a function $\dot{\gamma}_{\max}$ for λ-DNA have been included on the plot. Heo and Larson have measured the apparent viscosity of λ-DNA at concentrations from 0.21 to 0.72 mg/mL by bulk rheology.[7] The researchers measured the apparent viscosity of the DNA solutions at shear rates as low as 0.1 (1/s). A plot of η_{app} as a function $\dot{\gamma}_{\max}$ from Heo has been reproduced in figure 3.12. The lines in the figure are the results of fits of the Carreau-Yasuda model to the data. The values of the parameters of the fit for each concentration were also reported by the authors.

Only the most concentrated DNA solution investigated by Heo (0.72mg/mL) corresponded to a concentration of DNA (0.7mg/mL) which was investigated here. The bulk rheology results obtained by Heo for the 0.72mg/mL were therefore able to be compared to the apparent viscosities measured in this investigation by the magnetically driven particles for the 0.7mg/mL DNA solution. The data for the 0.72mg/mL DNA solution measured by Heo has been plotted as a dashed magenta line in figure 3.11.

Extrapolation to 2mg/mL

The other DNA solution used in this investigation (2mg/mL) was reportedly too concentrated to be able to be measured using the viscometer employed by Heo. In order to facilitate a comparison of the results reported by Heo with the apparent viscosities measured in this investigation for the 2mg/mL DNA, the parameter values for the fit model presented by Heo were extrapolated to a concentration of 2mg/mL. Each of the parameter values were plotted as functions of their corresponding DNA concentrations and fit to the power law in equation 3.16.

$$f(x) = Ax^b \qquad \text{Equation 3.16}$$

The resulting extrapolated function for η_{app} of a 2 mg/mL DNA solution as function of $\dot{\gamma}_{\max}$ is plotted as a dotted blue line in figure 3.11. In addition to the bulk rheology of lambda DNA reported by Heo, Cribb has measured η_{app} of a 1.44 mg/mL DNA solution as function of $\dot{\gamma}_{\max}$ using a cone-and-plate rheometer (unpublished data). These data are plotted as a solid pink line in figure 11.

Interpretation of the Thinning Shear Rate

As seen in figure 3.12, the shear rate which corresponds to beginning of the thinning regime (1/τ) gets smaller with increasing DNA concentration. The higher the concentration of the DNA therefore the smaller the shear rate is needed to produce thinning behavior. 1/τ occures in the extrapolated 2mg/mL data at a shear rate of approximately 0.02 1/s. This is also the shear rate which corresponds to the lowest value measured for the rods in the 2mg/mL DNA solution. Based on the extrapolation to 2mg/mL therefore, the 2mg/mL rod data would be expected to show thinning behavior. The observation that the 2mg/mL rod data does show thinning is therefore consistent with the behavior predicted by the extrapolated data.

The 0.7mg/mL rod data has associated shear rates which are below 1/τ for the bulk 0.72mg/mL of Heo. The existence of shear thinning behavior at the shear rates measured for the rods in 0.7mg/mL is therefore also consistent with the bulk rheology data. The 0.7mg/mL MyOne bead data would be expected to be below the shear rates which would result in shear thinning based on the 0.72mg/mL bulk data from Heo. It is not obvious from figure 3.12 however whether the negative slope is necessarily indicative of the thinning regime. To identify whether the MyOne data at 0.7mg/mL was demonstrating shear thinning, and to quantitatively compare the driven particle data with the bulk rheology data in figure 3.11, the data sets were fit to power law functions of the form of equation 3.16. The variables of the fits to the particle data were compared with those of the bulk measurements to interpret the apparent viscosities as experienced by the particles as functions of the shear rates in terms of the expectations based on bulk rheology. The values of these fits are shown in table 3.0.

Interpretation of Power Law Exponents of Shear Thinning Data

Table 3.0 will guide the comparison of the shear thinning behavior observed for the driven particle and bulk rheology data sets. Based on figure 3.12. it is expected that the power law exponent in the thinning regime should increase with increasing DNA concentration however the change should fall off exponentially. It is not surprising therefore that the exponent of the data for the rods in 0.7mg/mL and 2mg/mL, bulk 0.72mg/mL, and the bulk 1.44 mg/mL, all fit a power law with an exponent of between -0.9 and -0.8. The extrapolated 2mg/mL data has a higher exponent value of -1 though there may be significant error in this estimate. The power law exponent of the MyOne 0.7mg/mL data by contrast has a value of only -0.6. The exponent of the MyOne 0.7mg/mL was significantly smaller than the others in table 3.0. The lower power law exponent of the MyOne 0.7mg/mL data and the corresponding shear rates which are shown to be lower than the thinning regime for the bulk 0.7mg/mL data lead to the conclusion that the data do not indicate shear thinning.

The values for the driven particle apparent viscosities are all greater than the corresponding bulk rheology data. The reason for the increase in the measured apparent viscosities is not conclusively known and some of Cribb's data (unpublished results) may challenge this as a general phenomena. The bulk rheology experiments performed using a bob-and-cup design as in the report by Heo and Larson as well as the cone-and-plate design employed by Cribb et al do not measure compression. Therefore, one possible explanation for the increased apparent viscosities of the driven particle measurements over those of the bulk measurements involved compression of the DNA strands in front of the particles.

This mechanism has been treated for the case of entangled actin networks by Uhde and Sackmann.[28] The polymer system investigated by these researchers is more rigid than the DNA strands investigated here. The explanation of an additional force resulting from the osmotic pressure of the compressed polymers may not hold for the system investigated here. Another possible explanation for the increase in the measured viscosities, which has been treated by Rubenstein[29], involves the increase in the effective radius of the particle as it moves through the DNA. While experiments using these particles and DNA solutions have shown that there is no significant physisorbtion of DNA to the particles, the collision with DNA strands as the particles are pulled through the network could result in an increase in the effective radius of the particles.

Conclusions

In this investigation the magnetically driven mobility of nickel rods and MyOne beads in Karo and DNA were studied. The measurements of the particles' mobilities in a fully characterized magnetophoretic system using Karo as the medium enabled the investigation of the particles' velocities in the DNA solutions where the viscosity was not known. The characterization of the magnetophoretic system included all parameters related to the magnetophoresis of the particles: the magnetic field, the magnetic field gradient, the viscosity of the medium, the magnetic properties of the particles, and the particle dimensions. The independent quantification of these parameters of the total magnetophoretic system allowed the prediction of the magnetophoretic mobility and the forces applied to the particles. The validity of the theoretical magnetic force was compared with the force observed through the velocity measurements of the particles. The observed magnetic forces were in agreement with the predicted force, within the uncertainty of the observed and predicted values. The closing of the loop between the theoretical magnetophoretic forces, based on the magnetic characteristics of the system, with the forces measured by velocitometry represent a significant advance in the field.

The magnetophoretic systems of particles and media utilized in this investigation were pragmatic models for the investigation of magnetically driven particles in biological media. The MyOne beads and nickel rods were large enough to conveniently permit the observation of individual particles, but small enough to be relevant to other low Reynolds number micromagnetophoretic particle systems. The MyOne beads and the rods had large magnetic susceptibilities enabling the application of significant magnetic driving forces resulting in large mobilities over reasonable experimental timescales. The combination of spheres and high aspect ratio rods allowed the investigation of the relationships between the length scales of the media and those of the particles.

While these factors contributed to the successful use of these particles and media for quantifying the magnetophoretic system and investigating the shear thinning phenomena, the length scales of the systems are too large to be directly relevant to many life science applications. The particles utilized in this study were not biologically compatible due to their size and composition. The dimensions of the particles and length scales of the media used in this investigation were on the order of hundreds to thousands of nanometers. While the length scales of biological media are generally on the scale of ten nanometers or less.[12] The following chapter quantifies the magnetophoretic mobility of a nanoscale biocompatible magnetic label on a model particle platform. The final chapter builds on the results of this and the following chapters by demonstrating the magnetic transportation of a novel, magnetic, high aspect ratio, biomaterial, composite particle having dimensions which are directly relevant to the lengths scales of biological media.

Figures

Figure 3.0

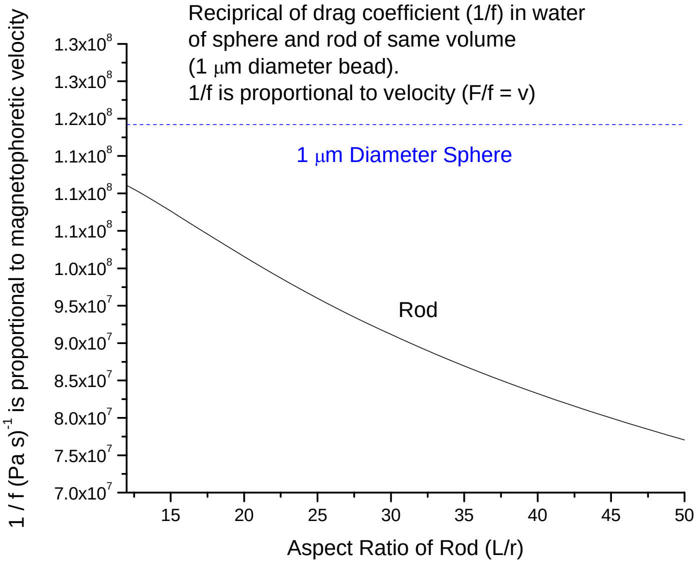

The magnetophoretic mobilities in a Newtonian medium of a sphere and rod of the same material, the same volume, and in the same field are proportional to 1/drag coefficient of each particle. For convenience the volume of a sphere having a diameter of 1 micron is used. It can be seen that because a sphere has a smaller drag coefficient, a sphere has the greatest mobility regardless of the aspect ratio of the rod.

Figure 3.1

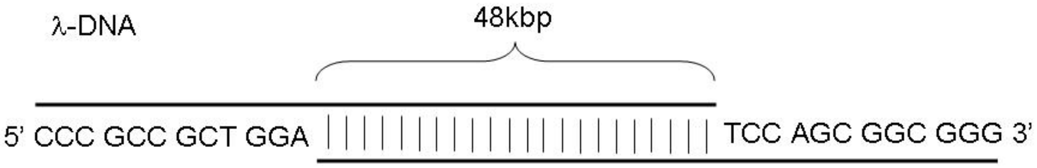

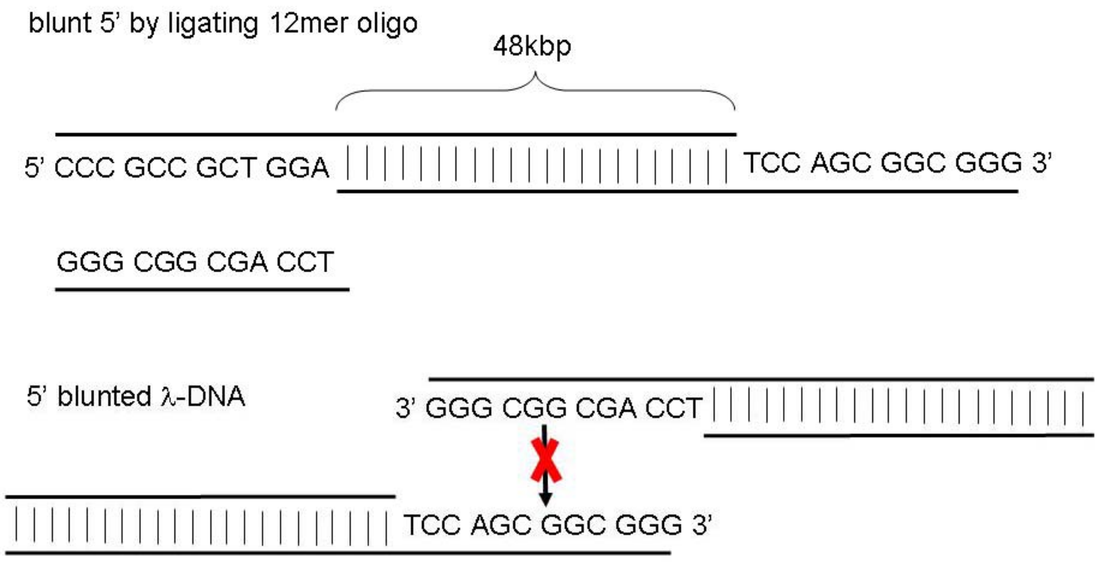

The above figure shows the sequence of DNA ligation to prevent end-to-end hybridization.

Figure 3.2

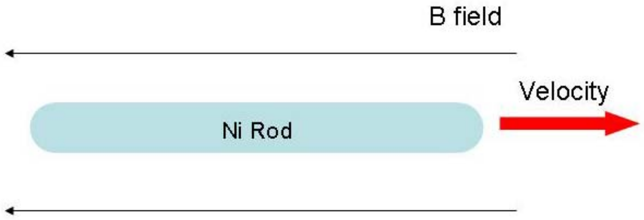

Magnetophoretic translational rod orientation

Figure 3.3

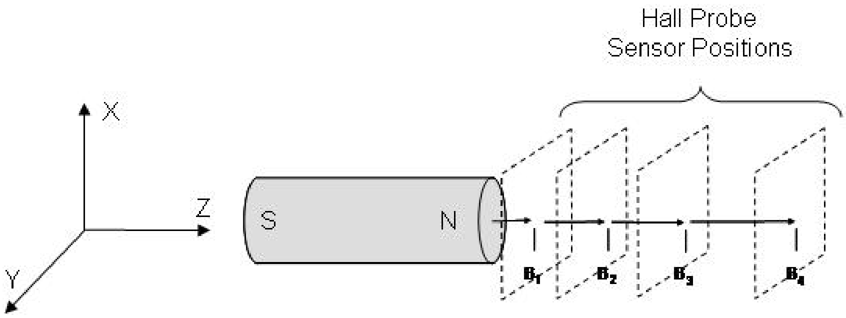

This figure depicts the orientation of the magnetic field measurements from axial face of permanent cylindrical magnet. The diagram is not to scale and the polar designations of the magnet are arbitrary.

Figure 3.4

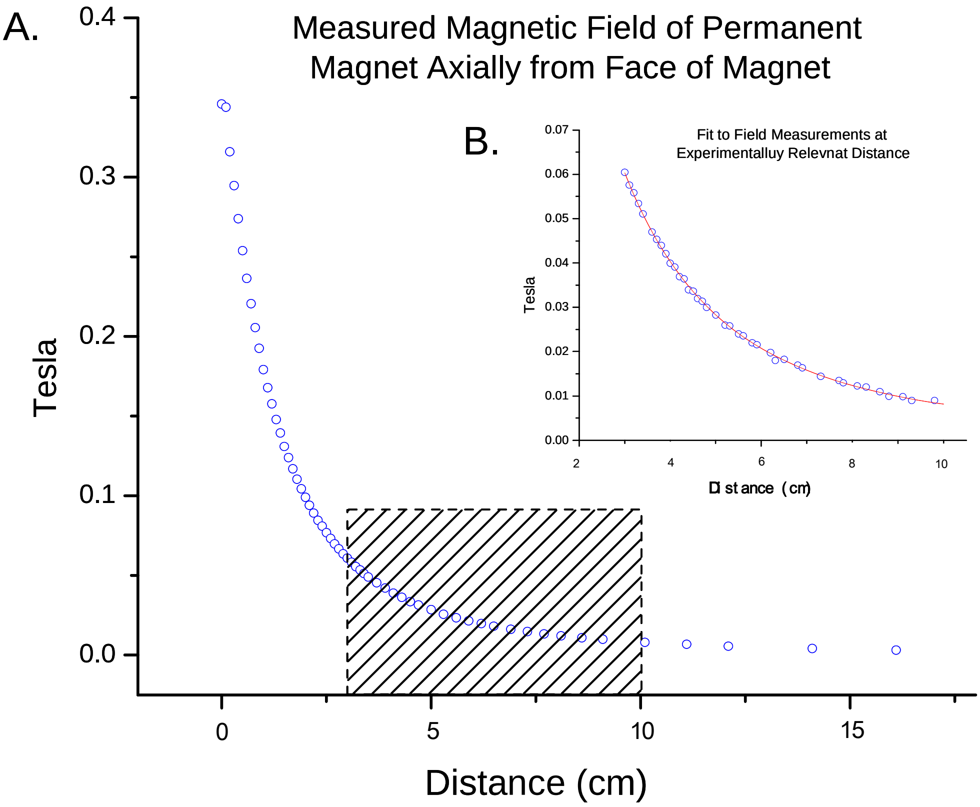

Measured magnetic field as a function of distance from the face of the cylindrical permanent magnet used as the magnetic source. The shaded box represents the field measurements over the experimentally relevant distance range. The mathematical fit to these data is plotted in figure 8.

Figure 3.5

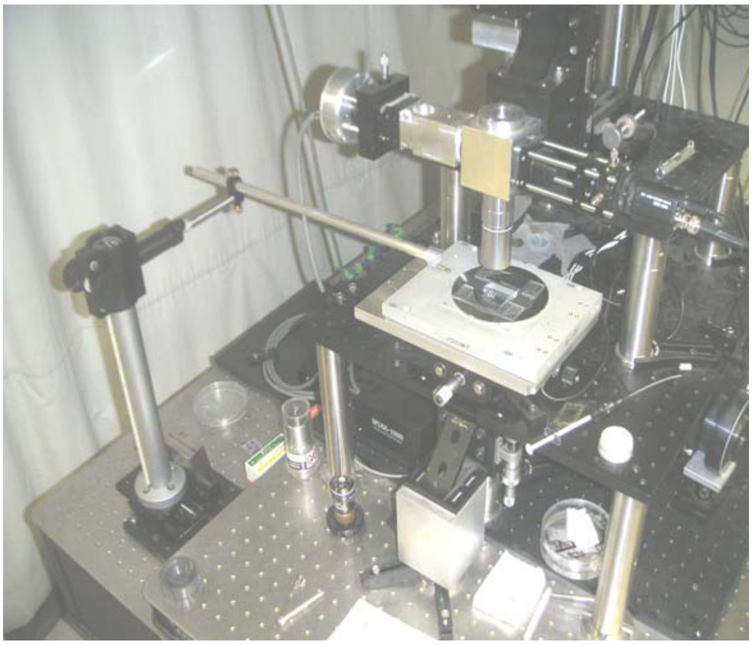

Magnetophoretic experimental apparatus consisting of an inverted microscope, a video camera for data collection, and a spring-loaded translation stage with the permanent magnet mounted on an aluminium translation arm. The entire apparatus was mounted on a compressed gas vibration isolation table.

Figure 3.6

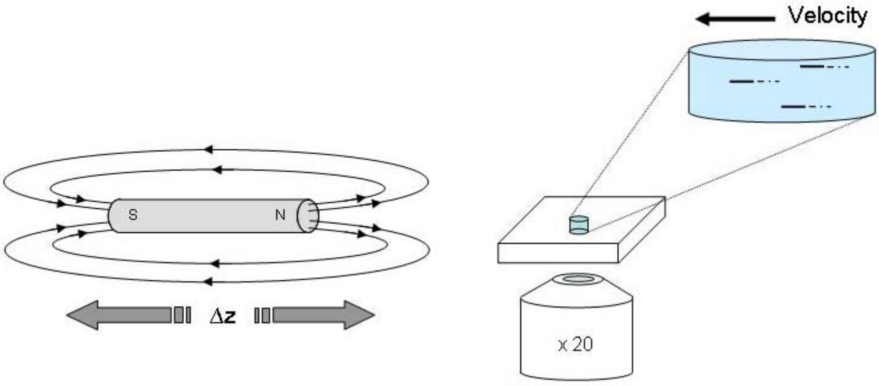

A magnetic field was applied to a magnetic particle suspension contained in a PDMS well using a cylindrical permanent magnet. The magnitudes of the applied field and field gradient were varied by adjusting the *z* position of the magnet with respect to the sample. The particles were tracked by imaging with an x20 objective and an inverted microscope. The diagram is not to scale and the polar designations of the magnet are arbitrary.

Figure 3.7

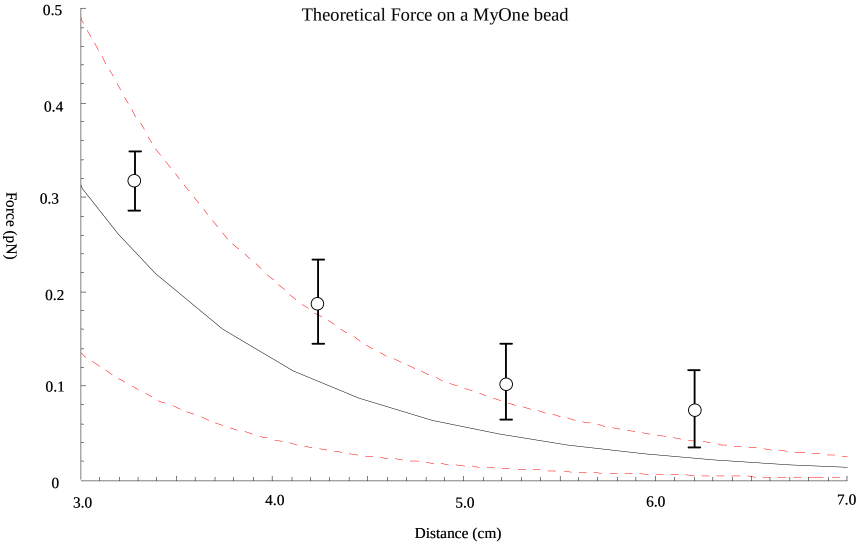

The average magnetophoretic force applied to MyOne beads as a function of the distance from the permanent magnet as plotted as circles. The error bars on these data are the standard deviation of the forces as calculated based on the velocities of the individual beads. The black solid line is the plot of the function of the theoretical force on the beads based on the measured magnetic properties of the beads and the quantified applied field. The red dotted lines are the upper and lower bounds on the uncertainty of the theoretical force.

Figure 3.8

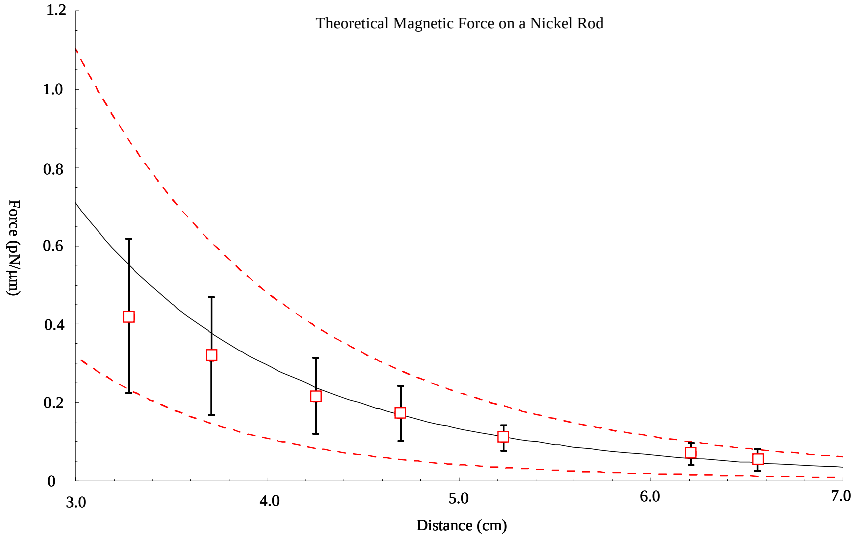

Average magnetophoretic force applied to a nickel rod in Karo as a function of the distance from the permanent magnet. The bars on these data are the standard deviations of the empirical force on the bead set as calculated based on the velocities of the individual rods. The variation of forces is attributed to differences in the magnetic characteristics of individual rods. The black solid line is the plot of the function of the average theoretical force on a rod per micron length based on the measured magnetic

Figure 3.9

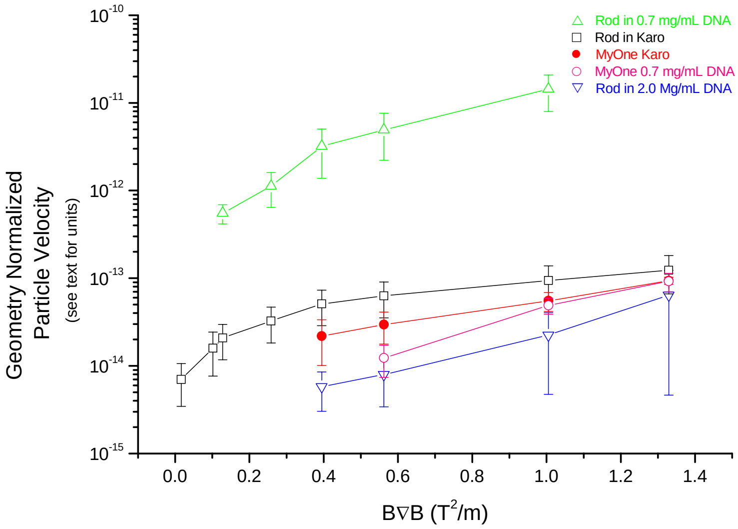

Normalized mobilities of rods and MyOne beads in Karo, 0.7 mg/mL and 2.0 mg/mL DNA solutions as a function of the magnetic force proportionality $B\nabla B$. The particle mobilities have been normalized with respect to their geometric components of their drag coefficients ($\tilde{\gamma}$) and the rods have additionally been normalized with respect to their lengths in microns. The units of the normalized velocities for the rods and the beads are m^2/s per μm length of the rod and m^2/s respectively. The bars on the data points represent the deviation of individual particle velocities and do no indicate measurement error.

Figure 3.10

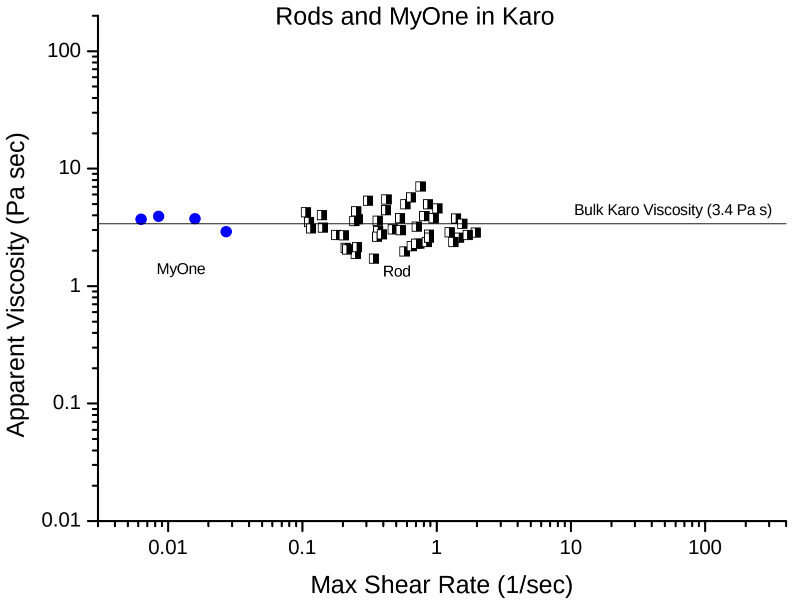

This figure shows the dependence of the apparent viscosities of Karo as experienced by MyOne beads and nickel nanorods as functions of the maximum shear rates. The line represents the bulk viscosity of Karo.

Figure 3.11

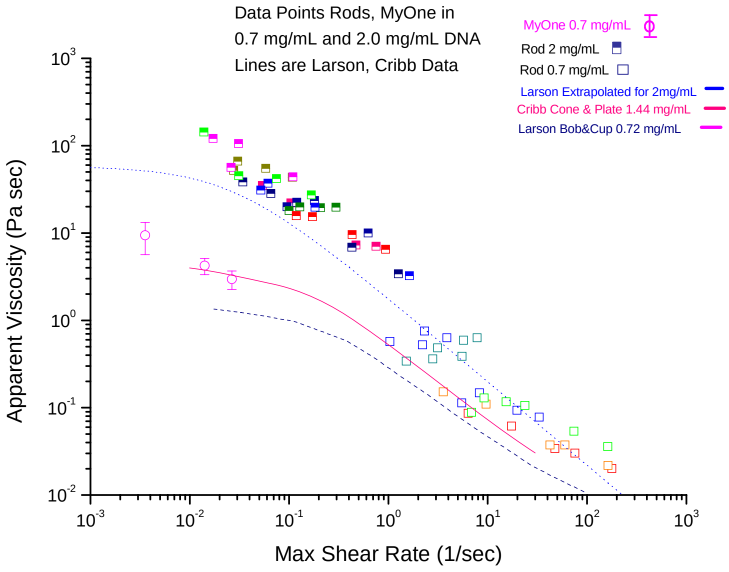

This figure shows the dependence of the apparent viscosities of λ-DNA at concentrations of 0.7 mg/mL and 2 mg/mL as experienced by MyOne beads and nickel nanorods as functions of the maximum shear rates.

Figure 3.12

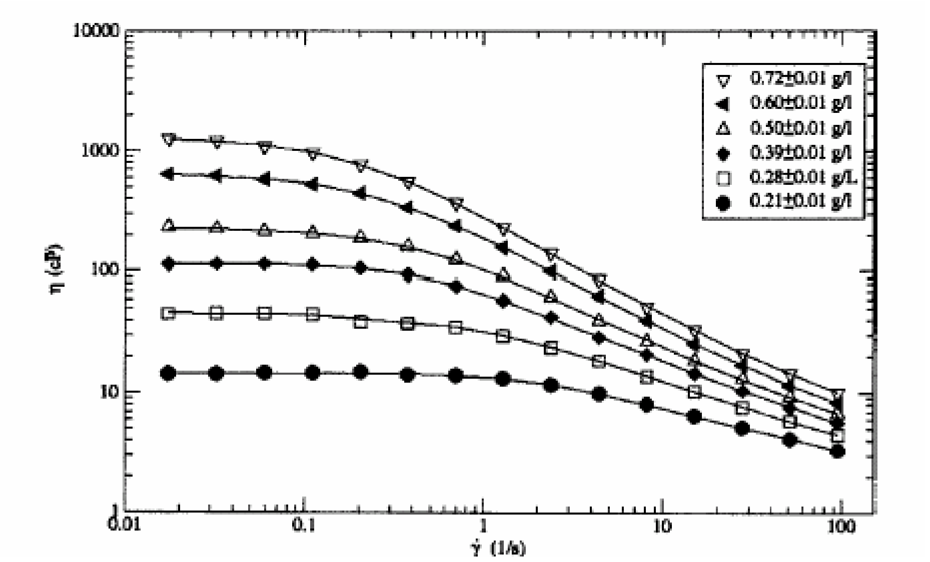

This figure of apparent viscosity as a function of the maximum shear rate for different concentrations of lambda – DNA has been reproduced from Heo, Larson 2005.All data were taken at 25C. The lines are fits to the data using the Carreau-Yasuda model.[7]

Table 3.0

Description	DNA Concentration (mg/mL)	Power Law Exponent	Design
MyOne	0.7	-0.6	Particle
Rod	0.7	-0.8	Particle
Rod	2.0	-0.8	Particle
Heo, Larson	0.72	-0.8	B&C
Extrapolated	2	-1	B&C
Cribb	1.44	-0.85	C&P

The table above list the exponents (b) of the fit of the power law $f(x) = ax^b$ to the data for the given concentrations. In the last column B&C refers to the bob-and-cup rheometer used to make the measurements and C&P refers to the cone-and-plate rheometer used to make that measurement.

References

1. Wirix-Speetjens, R., de Boeck, J., *On-chip magnetic particle transport by alternating magnetic field gradients.* Ieee Transactions on Magnetics, 2004. **40**(4): p. 1944-1946.

2. Deng, T., et al., *Manipulation of magnetic microbeads in suspension using micromagnetic systems fabricated with soft lithography.* Applied Physics Letters, 2001. **78**(12): p. 1775-1777.

3. Lee, H., A.M. Purdon, and R.M. Westervelt, *Manipulation of biological cells using a microelectromagnet matrix.* Applied Physics Letters, 2004. **85**(6): p. 1063-1065.

4. Lee, C.S., H. Lee, and R.M. Westervelt, *Microelectromagnets for the control of magnetic nanoparticles.* Applied Physics Letters, 2001. **79**(20): p. 3308-3310.

5. Lee, H., et al., *Controlled assembly of magnetic nanoparticles from magnetotactic bacteria using microelectromagnets arrays.* Nano Letters, 2004. **4**(5): p. 995-998.

6. Zborowski, M., et al., *Analytical Magnetapheresis of Ferritin-Labeled Lymphocytes.* Analytical Chemistry, 1995. **67**(20): p. 3702-3712.

7. Heo, Y. and R.G. Larson, *The scaling of zero-shear viscosities of semidilute polymer solutions with concentration.* Journal of Rheology, 2005. **49**(5): p. 1117-1128.

8. Gupta, R.B., *Nanoparticle Technology for Drug Delivery*. 2006: Informa Healthcare.

9. Edgeworth, R., Dalton, B. J., Parnell, T., *The Pitch Drop Experiment.* European Journal of Physics, 1984: p. 198-200.

10. Donald Voet, J.V., Charlotte Pratt, *Fundamentals of Biochemistry*. 1999, New York: John Wiley and Sons, Inc.

11. Fournier, R.F., *Basic Phenomena in Biomedical Engineering*. 2007, Taylor and Francis Group: New York.

12. Yurchenco, P.D., Y.S. Cheng, and H. Colognato, *Laminin Forms an Independent Network in Basement-Membranes.* Journal of Cell Biology, 1992. **117**(5): p. 1119-1133.

13. Michael Rubenstein, R.C., *Polymer Physics*. 2003, Oxford: Oxford University Press.

14. Hays, J.B., M.E. Magar, and B.H. Zimm, *Persistence Length of DNA.* Biopolymers, 1969. **8**(4): p. 531-&.

15. Wang, M.D., et al., *Stretching DNA with optical tweezers.* Biophysical Journal, 1997. **72**(3): p. 1335-1346.

16. Invitrogen. Carlsbad California 92008.

17. Hofmann, H., et al., *Localization of Flexible Sites in Thread-Like Molecules from Electron-Micrographs - Comparison of Interstitial, Basement-Membrane and Intima Collagens.* Journal of Molecular Biology, 1984. **172**(3): p. 325-343.

18. Fuh, C.B., L.Y. Lin, and M.H. Lai, *Analytical magnetapheresis of magnetically susceptible particles.* Journal of Chromatography A, 2000. **874**(1): p. 131-142.

19. Amblard, F., et al., *A magnetic manipulator for studying local rheology and micromechanical properties of biological systems.* Review of Scientific Instruments, 1996. **67**(3): p. 818-827.

20. Watarai, H., M. Suwa, and Y. Iiguni, *Magnetophoresis and electromagnetophoresis of microparticles in liquids.* Analytical and Bioanalytical Chemistry, 2004. **378**(7): p. 1693-1699.

21. Huang, N.P., et al., *Poly(L-lysine)-g-poly(ethylene glycol) layers on metal oxide surfaces: Surface-analytical characterization and resistance to serum and fibrinogen adsorption.* Langmuir, 2001. **17**(2): p. 489-498.

22. Kenausis, G.L., et al., *Poly(L-lysine)-g-poly(ethylene glycol) layers on metal oxide surfaces: Attachment mechanism and effects of polymer architecture on resistance to protein adsorption.* Journal of Physical Chemistry B, 2000. **104**(14): p. 3298-3309.

23. Sypris. Orlando FL.

24. www.med.unc.edu/olioli. UNC Oligonucleotide Synthesis Core Facility.

25. James Joseph Greene, V.B.R., *Recombinant DNA Principles and Methodologies*. 1998: CRC Press. 790.

26. Tirado, M.M. and J. Garciadelatorre, *Translational Friction Coefficients of Rigid, Symmetric Top Macromolecules - Application to Circular-Cylinders.* Journal of Chemical Physics, 1979. **71**(6): p. 2581-2587.

27. Cribb, J., *Unpublished data*. 2007.

28. Uhde, J., Sackmann, Erich, *Osmotic Force Controlled Microrheometry of Entangeld Actin Networks.* PRL, 2005. **94**(198102).

29. Rubinstein, M., *Polymer Physics*. 2003: Oxford University Press.

CHAPTER FOUR: Magnetic Force Quantification on Individual Ferritin Loaded Beads

Introduction

Ferritin has been identified as an attractive biocompatible magnetic label for magnetophoretic biomedical applications. While the utility of ferritin as a magnetic label in biological media has been widely studied, there are no examples in the literature of the ferritin loading being quantifiably correlated with the magnetophoretic velocity of ferritin labeled particles. [1-7] The connection between the magnetic properties of ferritin, the loading, and the magnetic force which can be applied to individual ferritin molecules, or to an individual ferritin labeled particle, is essential for the design of future ferritin based magnetophoretic systems. This investigation reports for the first time the correlation between the magnetic properties of ferritin and the measured magnetic force applied to ferritin.

In a practical ferritin based magnetophoretic system, whether for a separations application, gene transfection or drug delivery, a variety of particle platforms might be utilized depending on the considerations of the specific application. The nature of the media, the size and the shape of the carrier particle, and the magnetophoretic velocity requirements are all contributing factors in the selection of the platform.[8] For example, a high aspect ratio particle might be more effective as a carrier in a biological medium where the relative length scales of the particle and the medium would have an influence on the magnetophoretic velocity of the particle. In contrast, a sphere in a separations application utilizing a homogeneous medium would have a greater driven velocity, as shown in chapter 3, and might therefore be a more appropriate choice of particle.

The size of the ferritin labeled b is a significant consideration in maximizing the magnetophoretic velocity. The magnetophoretic force which is applied to the labeled bead is proportional to the amount of ferritin on the surface of the bead, which is in turn related to the surface area of the bead. The magnetic driving force is therefore related to the square of the particle's radius (area). However, the viscous drag is directly proportional to the radius of the spherical particle through Stokes' Law as previously discussed. These relationships, which are summarized in equation 4.1 and 4.2, result in the conclusion that the velocity of a magnetically driven, surface labeled sphere in a viscous medium, will increase with increasing size.

$$F_{mag} = \left[\frac{2}{3}\frac{\pi\chi\nabla B^2}{\mu_0}\right]r^3 \qquad \text{Equation 4.1}$$

$$F_{drag} = \left(6\pi\eta v\right)r \qquad \text{Equation 4.2}$$

While a larger ferritin labeled bead will have a greater magnetophoretic velocity, an upper size limit of the bead may be considered to be set in part by the sedimentation rate. A bead which is too large may sediment on the time scale of the experiment. For example, a bead tens of microns would settle out on the bottom coverslip in a few minutes. This could result in the particle interacting with surfaces, thereby adding drag, which will serve to decrease its magnetophoretic velocity. For this investigation, a model polymer microsphere support was chosen in order to quantify the ferritin loading and to correlate it with the measured magnetophoretic velocities of individual particles. The selection of a 6 μm diameter polymer bead for this investigation was determined to be an appropriate choice for maximizing the particle size without compromising the suspension stability of the colloidal platform. The beads were monodispersed and highly symmetric, serving to limit bead to bead variation in ferritin loading and minimize the variation of the magnetically driven velocities of individual beads.

The magnetization of a ferritin labeled bead is typically much smaller than commercial paramagnetic particles, (such as the MyOne microspheres described previously), due to the small relative susceptibility of ferritin.[6] Because of the Brownian motion experienced by colloidal systems at ambient temperature, velocitometry measurements of ferritin loaded beads may be dominated by non-directional diffusive motion provided there is not a large driving force. A high ferritin loading on the support beads was therefore desired to provide a large magnetophoretic force. By maximizing the ferritin loading, the magnetophoretic velocities of the particles were likewise maximized, resulting in a greater signal-to-noise ratio of the velocity measurements and a commensurate reduction in the measurement error.

Protein loading onto surfaces has been the focus of numerous studies both for the enhancement and prevention of protein adsorption.[9-13] Hydrophobic surfaces such as the polystyrene beads used in this study have been shown to strongly physisorb proteins.[14, 15] In order to attach ferritin to the beads in a more robust manner than physisorbtion alone, the beads were additionally functionalized with ferritin by the covalent attachment to the beads through an amide bond.

The protein loading on a surface can be measured by a multitude of direct and indirect methods.[16-18] A traditional method of quantifying the adsorption of protein, known as a depletion method, is performed by measuring the concentration of the protein in solution before and after the introduction of the adsorbent surface.[19, 20] The concentration of ferritin in solution was therefore measured before and after incubation with the beads, to determine the depletion of ferritin from solution, which corresponded to the loading of ferritin on the beads.

A convenient method of determining the concentration of a protein in solution is the measurement of the UV absorbance of the solution at 280 nm as described in 1942 by Warburg and Christian.[21] The aromaticity of the phenylalanine, tyrosine, and tryptophan amino acid residues present to some degree in all proteins, results in a strong absorbance at this wavelength. The ubiquity of these amino acids in proteins provided a straight forward technique for measuring the solution concentration of ferritin. However, the relative ratio of these aromatic residues to the protein as a whole can vary widely between proteins, resulting in different proteins having different 280 nm absorbance intensities relative to the number of aromatic residues they contain. Therefore, in order to use the UV absorbance as a means to quantify the concentration of ferritin in solution, a calibration curve specific for ferritin was determined.

The magnetophoretic velocity of magnetically driven particles can be used as a means of deducing the magnetic properties of the particle.[6, 22] Alternately, if the magnetic properties of a magnetophoretic system are well characterized, theoretical magnetically driven velocities of the particles can be predicted. The characterization of the magnetophoretic parameters relevant to the magnetic velocity of the ferritin labeled particles, in tandem with the quantification of the magnetophoretic velocities of the particles, enabled the correlation of the theoretical magnetic driving forces with the empirically determined velocity values.

Experimental

Ferritin Concentration Determination

Absorbance measurements at 280 nm of ferritin in MES (2-(*N*-morpholino)ethanesulfonic acid) buffer standards were taken over the concentration range of 2 to70 μg / 600 μL using a Cary 400 Bio-UV-visible spectrometer. The absorbance of each concentration standard was measured six times and the replicates were averaged.

Covalent ferritin labeling

A 4 mg sample of 6 μm carboxy (COOH) functionalized polystyrene microspheres, corresponding to 4.2 x10^7 beads (Polyscience, Inc., Warrington, PA) was washed three times by centrifugal sedimentation in MES buffer in order to obtain a homogenous particle suspension. After washing, the beads were resuspended in MES buffer in preparation for covalent labeling with ferritin. Horse spleen derived native ferritin (Sigma-Aldrich) was used as supplied. An incubation solution of ferritin diluted in MES buffer to a concentration of 0.1mg/mL was prepared for labeling the beads. The initial ferritin content of a 600 μL aliquot of the incubation solution was quantified by taking 6 replicate UV absorbance measurements at 280 nm.

The beads, suspended in MES buffer, were added to a 20 μL aliquot of an 80 mg/mL solution of EDAC (*N*-(3-Dimethylaminopropyl)-*N'*-ethylcarbodiimide hydrochloride) in MES buffer which served to activate the carboxy groups on the beads toward the covalent attachment to primary amines present in ferritin. The addition of EDAC to the bead suspension was followed by brief sonication to prevent aggregation of the particles. Immediately following the dispersion of the beads in the EDAC solution, 500 μL of the ferritin incubation solution was added to the sample. The covalent linkage of the ferritin to the beads was allowed to proceed with vortexing for 90 minutes.

Following ferritin functionalization, the beads were slowly sedimented by centrifuging at 1000 rpm for ten minutes. 600 μL of the supernatant was then carefully removed and analyzed by UV absorbance at 280 nm. The ferritin content of the supernatant was calculated using the absorbance versus concentration ferritin calibration curve. After removing the supernatant for analysis, the beads were resuspended in Tris (trishydroxymethylaminomethane) buffer in preparation for use in magnetophoresis experiments.

EDAC catalyzed ferritin sedimentation control

The carbodiimide attachment of ferritin to the beads using EDAC proceeded by activating the carboxy groups on the surface of the beads toward the formation of a covalent bond with primary amines. Primary amines exist in the protein in the forms of lysine residues and as the terminal amine on the last amino acid of the peptide sequence. Any or all of these amines may be available to provide a covalent attachment to the bead.[23]

While the activation of the carboxyl groups on the beads is the desired reaction, an excess of un-reacted EDAC or a high protein concentration may result in covalent agglutination of ferritin by activating the carboxyl groups present in the aspartic and glutamic acid residues of the protein. This might cause the formation of aggregates of ferritin which could potentially sediment during the bead washing steps after the ferritin loading. The determination of the ferritin using a depletion method through subsequent UV absorbance analysis of the supernatant would, therefore, measure a lower solution ferritin concentration, which would not be correctly correlated with the ferritin loading on the beads. This would lead to the erroneous conclusion that a higher loading of ferritin on the beads had been achieved.

A control experiment was performed in order to eliminate the concern of EDAC catalyzed ferritin flocculation. Solutions of high and low concentrations of EDAC were incubated with ferritin under conditions equivalent to those used for ferritin loading on the beads. The low concentration EDAC solution was identical to the concentration used for loading ferritin on the beads. The high EDAC concentration solution was eight-fold more concentrated than the EDAC solution used for ferritin loading. Following the reaction, the samples were centrifuged at 1000 rpm for 10 minutes, in line with the procedure used for ferritin loading on the beads. The ferritin concentration of the supernatants and the original ferritin solution were then measured by UV absorbance at 280 nm as previously described.

The ferritin concentration in the supernatants of the high EDAC samples were 80% lower than the original ferritin solutions, indicating a significant degree of removal of free ferritin from solution. The ferritin concentration of the low EDAC sample supernatant, however, was unchanged within the experimental uncertainty from the original ferritin solution concentration. These results indicated that ferritin flocculation catalyzed by excess EDAC was not a concern under the conditions utilized for the ferritin loading on beads, however that flocculation could occur at higher EDAC concentrations. This control experiment gave confidence that the solution depletion of ferritin was compatible with this ferritin labeling protocol, and that it was a reliable method of determining the ferritin loading on the bead supports.

Results and Discussion

Spectroscopic Ferritin Concentration Calibration

The average absorbance value for each ferritin concentration standard is plotted as a function of the concentration in figure 4.0. The standard deviation of the absorbance values of the six replicates at each concentration were used as the absorbance uncertainties. An error weighted linear regression fit of the data set yielded a R^2 value of 0.999. The slope of the linear fit to the calibration curve was used to calculate the slope of the absorbance versus concentration as 1.4×10^{-2} ($\pm 1.4 \times 10^{-4}$) arbitrary absorbance units (a.u.) per μg of ferritin / μL of solution. The slope of the calibration curve was then used to quantify the ferritin loading on the beads by measuring the absorbance at 280 nm of the ferritin incubation solution before and after incubation with the beads.

Calculation of ferritin loading per bead

UV absorbance measurements of the ferritin solution before and after incubation with the beads indicated a decrease in the solution content of ferritin from 63.9 (±0.40) μg to 4.4 (±0.04) μg. This represented a 93% decrease in ferritin in solution which corresponded to a loading of 59.9 (±0.96) μg of ferritin on the beads. In order to be able to effectively use UV absorbance as a method of determining the concentration of a solution species, the relationship between absorbance and concentration must be linear. Typically, at low protein concentrations, the relationship of absorbance to the concentration is in the linear regime as described by the Beer-Lambert law.[24] The absorbance at 280 nm as a function of the ferritin concentration for the series of concentration standards and incubation samples was linear and was therefore in compliance with Beer-Lambert.

The average ferritin loading per bead resulted in a determination of an average loading of 1.4×10^{-12} g of ferritin per 6 μm bead. This average mass loading of ferritin per bead corresponds to an average of 1.2×10^{6} ferritin molecules per bead. A simple 'parking lot' approximation of the average loading of ferritin per bead based on the surface area of the bead, and the cross sectional area of the spherical ferritin molecule, estimates that this value corresponded to approximately five monolayer equivalents of ferritin per bead. The calculations for these values can be found in appendix 5. It is reasonable that a ferritin loading greater than a monolayer coverage could be achieved by EDAC activation of carboxylic acid groups on immobilized protein, due to a high local ferritin concentration on the bead surface. It should be noted that the ferritin loading per bead is a statistical average of the ferritin loading per bead, however the distribution of ferritin loadings over the entire bead population was not measured.

The diffusive velocity of a bead represents an unavoidable source of noise in measuring the magnetophoretic velocity of a particle. In order to obtain a useful signal-to-noise ratio for the measurement on a reasonable experimental timescale, a magnetophoretic bead velocity several times greater than the diffusive velocity was desirable. Using the average ferritin loading per bead, and the measured susceptibility of ferritin as discussed previously, it was possible to estimate the magnetic field characteristics which were necessary for imparting a measurable magnetophoretic velocity to a ferritin loaded bead. The low susceptibility of ferritin, relative to the MyOne beads or the nickel rods for example, required the application of a large magnetic field and, or field gradient in order to impart a magnetophoretic velocity significantly greater than the diffusive mobility of the particles.

The field gradient of a magnet is related to the physical dimensions of the magnet. As with electric fields, magnetic fields produced by sharp corners result in local large field gradients. A gradient as large as was necessary could not conveniently be applied to the ferritin labeled beads using a macroscale permanent magnet. A sharply pointed magnetic source was needed in order to be able to apply a large magnetic field gradient near individual ferritin labeled beads. Therefore, a microscale magnetic system was required for the application of the high field gradient necessary to obtain a practical magnetophoretic velocity of the ferritin beads.

The three-dimensional force microscope (3DFM), a micro-magnetic instrument developed in house and shown in figure 4.1, was ideally suited to the quantification of the magnetophoretic velocity of individual ferritin particles.[25] The 3DFM enabled the application of a large field gradient near individual beads while simultaneously imaging the sample with a conventional light microscope. The microscale of the 3DFM pole piece resulted in the magnetic field falling off dramatically over a distance of only tens of microns. This enabled the application of the high field gradient, which was necessary for the quantification of the magnetophoretic force on individual ferritin beads by velocitometry.

3DFM Magnetophoresis of Ferritin Beads

Magnetic flux was generated in the 3DFM by electromagnetic coils located outside of the sample chamber. The magnetic flux was directed to the sample by micro-machined poles made from a high susceptibility metal foil. The strength of the magnetic field which was applied to the sample was variable based upon the voltage applied to the coils. The pole geometry and the pole-to-pole spacing could be modified according to the nature of the experiment in order to produce a variety of magnetic field geometries and gradients. Video recording of the particles under the application of the magnetic field enabled the quantification of the magnetophoretic velocities of individual particles.

A pole-flat configuration similar to that shown in figure 4.2 was chosen as the experimental pole geometry because of the large field gradient which is generated near the pole tip. The pole pieces used in this study were coated with a protective polymer layer of perylene to eliminate corrosion of the poles, which could result in contamination of the sample with microscopic ferromagnetic particles. Successful control experiments were conducted with the pole pieces prior to the magnetophoretic experiments in order to confirm that the pole pieces were effectively coated with the protective polymer layer.

These control experiments were performed by loading a sample of nonmagnetic beads, suspended in Tris buffer, which had not been in contact with ferritin into the sample chamber of the 3DFM. The maximum voltage was applied to the coils for several minutes while video data of the bead positions was recorded. Post experiment video tracking and data analysis enabled the conclusion that there was no magnetophoresis of the control beads. This demonstrated that there had been no contamination of the sample by magnetic particulates resulting from corrosion products and, therefore, that the perylene coating effectively prevented the corrosion of the pole pieces.

A suspension of ferritin functionalized beads and nonmagnetic, 1 μm polystyrene control beads in Tris buffer were loaded into the sample chamber of the 3DFM. The greatest magnetic field was generated by applying the maximum voltage of 5V to the electromagnetic coils. The sample was imaged using a x40 objective and video data was recoded at 120 frames per second (fps). Post processing of the video data using software developed in house, enabled single particle tracking. The location of individual ferritin beads as a function of time was used to quantify the magnetophoretic velocity of each bead. The magnetophoretic forces on the ferritin beads were calculated from the bead velocities using a low Reynolds number assumption and Stokes' law as described in the previous chapter. The paths of the non-magnetic control beads were also tracked in order to determine the drift velocities which were subtracted from the magnetically driven velocities of the ferritin beads.

In order to correlate the predicted magnetic force applied to the ferritin labeled particles in the 3DFM with the observed magnetophoretic velocity of the particles, the applied field conditions were determined. The microscopic dimensions of the 3DFM pole piece prevented the direct quantification of the field magnitude and gradient using a traditional Hall probe. It was therefore not possible to calculate a theoretical magnetophoretic force for the ferritin beads in the 3DFM based on the direct measurement of the magnetic field and the field gradient. The theoretical magnetophoretic forces applied to the ferritin beads were therefore calculated by comparison with the forces applied to the magnetically characterized MyOne beads under the same applied field conditions.

The magnetic force which was applied to the MyOne beads in the 3DFM as a function of the distance of the bead from the pole had been measured previously by Fisher et al.[26] The same configuration of pole-flat pole geometry was used in the magnetophoresis of ferritin beads in the 3DFM as was used in this previous investigation. The particle volumes and susceptibilities were measured for both, MyOne beads and ferritin in a proceeding chapter, and the average ferritin loading per bead had been quantified.

As shown previously, ferritin does not saturate, even at an applied field of up to 5 T, which was much greater than could be realized by the 3DFM. The MyOne beads however may begin to saturate at applied fields which are possible under the experimental conditions. If saturation of the MyOne beads had taken place at the distances from the pole corresponding to the distances of the velocitometry data collection of the ferritin labeled beads, then the comparison of the forces on the ferritin loaded beads predicted based on Fisher's data would result in the underestimate of the magnetic force applied to the ferritin labeled beads.

Derivation of theoretical magnetic force on a ferritin bead

While the ferritin beads traveled toward the high magnetic field localized at the pole tip, more precisely they traveled along paths which intersected the *center* of the pole tip. This point in the center of the pole tip was used to represent the origin of the magnetic attraction and will henceforth be referred to as the virtual monopole. In practical terms, the virtual monopole was estimated by measuring the center point of the circle which circumscribed the front edge of the pole tip as shown in figure 4.3. The position of the ferritin beads was described in terms of the radial distance from the position of this virtual monopole.

The magnetic force on a magnetizable bead in the 3DFM was proportional to the volume of the magnetizable material *V*, and the volumetric susceptibility χ_v, according to equation 4.3.

$$F = \frac{1}{2}\frac{V\chi_v \nabla B^2}{\mu_0} \qquad \text{Equation 4.3}$$

Since the magnetic field and the magnetic field gradient product term ∇B^2 were functions of the distance *x* from the virtual monopole, a ferritin bead and a MyOne bead at the same distance would experience the same magnetic field and field gradient. The ratio of the forces on each particle as a function of distance were, therefore, proportional to the ratio of the product of the volume of magnetic material, and the volumetric susceptibility $V\chi_v$ for each particle according to equation 4.4.

$$\frac{F_{ferritin}(x)}{F_{MyOne}(x)} = \frac{V_{ferritin}\chi_{V_{ferritin}}}{V_{MyOne}\chi_{V_{MyOne}}} \qquad \text{Equation 4.4}$$

The use of the susceptibility in this relation assumes that the ferritin beads and the MyOne beads are not saturated by the application of the field at the distances x.

The volume of ferritin loaded on each bead was calculated from the average number of ferritin per bead, and the volume of an individual ferritin protein, as calculated in a previously chapter according to: (ferritin molecules per bead) (volume of ferritin molecule) = average volume of ferritin loaded on a bead

$$\left(1.2\cdot 10^{6}\,\frac{ferritin}{bead}\right)\left(7.2\cdot 10^{-24}\,\frac{m^3}{ferritin}\right) = 8.6\cdot 10^{-18}\,m^3 \qquad \text{Equation 4.5}$$

The product of the volume of ferritin on a single bead as calculated above in equation 4.5 and the volumetric susceptibility as determined in chapter 2 are calculated in equation 4.6. The product of the volume of a MyOne bead and the volumetric susceptibility of the MyOne beads are likewise calculated in equation 4.7.

$$V_{ferritinOnBead}\chi_{v_{ferritin}} = \left(8.6\cdot 10^{-18}\,m^3\right)\left(1.6\cdot 10^{-5}(SI)\right) = 1.4\cdot 10^{-22}\,m^3 \qquad \text{Equation 4.6}$$

$$V_{MyOne}\chi_{v_{MyOne}} = \left(6.1\cdot 10^{-19}\,m^3\right)\left(0.85(SI)\right) = 5.2\cdot 10^{-19}\,m^3 \qquad \text{Equation 4.7}$$

The theoretical magnetic force proportionality for a ferritin bead and a MyOne bead at the same position x can be related by the volume and susceptibility products calculated above in equations 4.6 and 4.7. The magnetic force is proportional to these products and enabled the convenient calculation of the ratio of the predicted magnetophoretic forces based on the magnetic characteristics of the particles according to equation 4.8.

$$\frac{F_{ferritin}(x)}{F_{MyOne}(x)}=\frac{V_{ferritin}\chi_{ferritin}}{V_{MyOne}\chi_{MyOne}}=\frac{1.4\cdot 10^{-22}m^3}{5.2\cdot 10^{-19}m^3}=2.6\cdot 10^{-4} \qquad \text{Equation 4.8}$$

The relationship for the theoretical force on ferritin beads at distance *x* from virtual monopole is described using the proportionality constant calculated in equation 4.8 and expressed in equation 4.9.

$$F_{ferritin}(x)=\left(2.6\cdot 10^{-4}\right)F_{MyOne}(x) \qquad \text{Equation 4.9}$$

The magnetophoretic forces on the ferritin beads were normalized with respect to the magnetophoretic forces on the MyOne beads by dividing the ferritin bead force values measured for individual beads by the conversion factor of 2.6 x10^{-4} as calculated in equation 4.8. To compare the magnetic force applied to the ferritin labeled beads in the 3DFM with that predicted based on magnetic characteristics of ferritin and the MyOne beads, and the forces applied to MyOne beads measured by Fisher, the force values of the ferritin labeled beads were plotted on figure 4.4 along with Fisher's MyOne data. In the figure, Fisher's MyOne bead data is represented by black dots and the ferritin labeled bead force data is represented by blue circles. The forces which were applied to the MyOne beads were much greater than the ferritin labeled beads, owing to the greater susceptibility of the beads. It was not, therefore, possible to use the same Y axis scale to represent both the ferritin labeled bead and the MyOne bead data.

To present both data sets simultaneously in figure 4.4, two Y axis scales were used in the figure. The Y axis in black on the left side corresponds to the MyOne data, while the right side in blue corresponds to the ferritin labeled data. While the values on the two axes correctly relate to the force values of the two data sets, the data points of the MyOne data have been multiplied by the normalization factor according to equation 4.8 to align correctly with the ferritin bead data points.

It is apparent from figure 4.4 that while there is a close correlation in the normalized force values of the MyOne data points and the ferritin labeled data points, that the power laws of the data sets are different. The MyOne has a power law exponent of approximately -1.3. While the broad distribution of the ferritin labeled bead data results in too great of an error to calculate a useful power law exponent, it is apparent that the exponent is slightly greater than that of the MyOne data.

The larger power law exponent of the ferritin labeled beads with respect to that of the MyOne beads is consistent with the prediction that the MyOne beads would begin to saturate. The magnetic moments of the MyOne beads therefore did not maintain the same power law increase as the beads became saturated. The saturation of the MyOne beads therefore resulted in a reduction of the power law exponent of the force on the beads as a function of distance from the pole. Since the ferritin did not saturate, the power law was maintained and was greater than that of the MyOne beads.

Conclusions

The loading of the magnetizable protein ferritin was quantified on a model microsphere support. The magnetophoretic force applied to individual ferritin beads in a microfluidic, high field gradient system has also been quantified. By quantitatively measuring these parameters, a theoretical magnetic force has been calculated for the ferritin beads in this system. This predicted force was found to be well correlated with the observed magnetophoretic force. This investigation is the first quantification of the magnetophoretic forces on individual ferritin labeled particles, and represents an important step forward in the use of ferritin as a magnetic label in quantitative magnetophoresis applications. Additionally, in so far as the loading of ferritin per bead has been measured, this is also the first report of the quantification of the magnetic force per ferritin molecule.

The magnetic force applied to the MyOne beads was on the order of hundreds of pN, approximately four orders of magnitude greater than the magnetic force on the ferritin loaded beads.[26] The large disparity between the magnetic forces which can be applied to the MyOne beads versus ferritin is due to the inherent material properties of the two particles. This fact becomes apparent by comparing the susceptibility values of the two particles in tables 2.1 and 2.2. The mass susceptibility of ferritin is only 0.03% that of the MyOne beads. The volumetric susceptibility of ferritin is an even smaller percentage, being only 0.002% that of the volumetric susceptibility of the MyOne beads. Put another way, in order to obtain a magnetic force on a ferritin loaded particle commensurate with a single MyOne bead one, would require a sphere of ferritin with a diameter of 40 μm. This is 2.4 $x10^5$ times more ferritin than was loaded on each 6 μm polymer bead in this investigation. Clearly, the advantage of ferritin over commercial particles is not due to the large force which can be applied using a small magnetic field.

Commercial magnetic particles, such as the MyOne beads, typically have large susceptibilities but may saturate at relatively small fields.[27] While the susceptibility of ferritin is small compared to the MyOne beads, these beads were observed to saturate under the 3DFM experimental conditions, and the ferritin labeled beads did not. The high saturation field of ferritin is an added advantage over commercial particles. The linear magnetization as a function of the applied field exhibited by ferritin in figure 2.4, and the lack of saturation exhibited by the ferritin labeled particles as compared to the MyOne beads in figure 4.4 demonstrate the unique characteristics afforded ferritin within the context of magnetic labeling.

The primary advantage that ferritin offers as a magnetic label is in its biocompatibility. The polymer beads were used in this investigation as a model platform for the correlation of ferritin loading with the quantified magnetophoretic velocity. The ferritin loaded support beads were selected based on experimental constraints without consideration for their biological compatibility and therefore may not be appropriate for use in vivo. The following chapter builds on the quantification of ferritin in a model magnetophoretic system presented here while extending its use to a biological context.

Figures

Figure 4.0

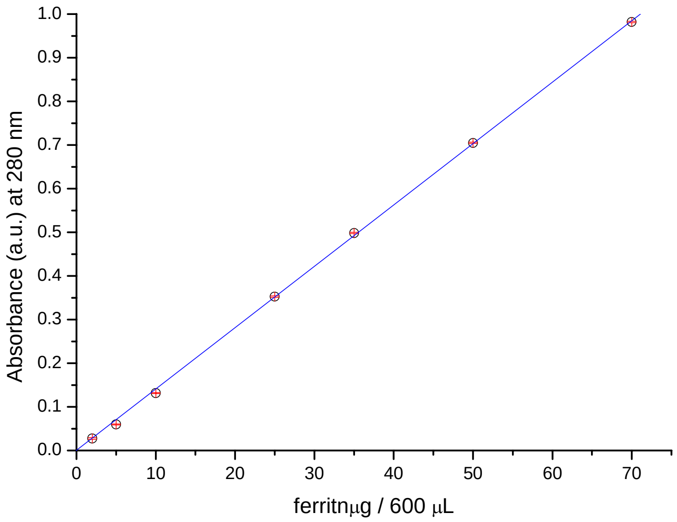

This figure shows the UV-vis calibration curve for absorbance at 280 nm of ferritin concentration standards. Six replicates are averaged for each data point represented by open black circles. The standard deviations of the six replicates represent the uncertainty of the data and are represented on the plot by red error bars (very small). The error weighted linear fit to the data is represented by the blue line. The fit has an R^2 value of 0.999 demonstrating good absorbance versus concentration linearity in obedience with Beer-Lambert.

Figure 4.1

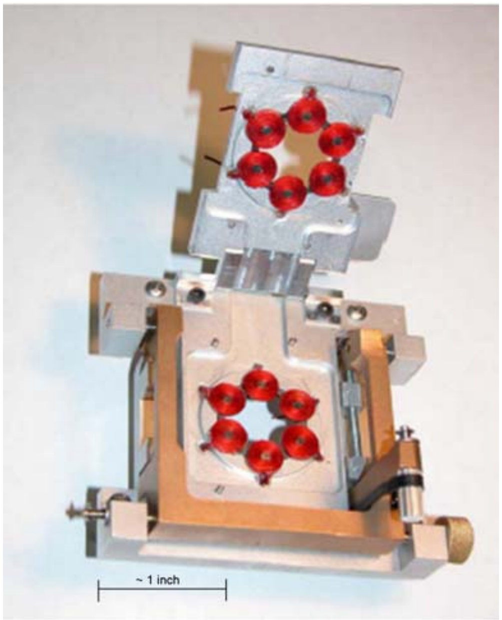

The image in this figure is of the stage of the three-dimensional force microscope (3DFM). Magnetic flux is provided by the red electromagnet coils. Thin foil pole pieces are affixed to a glass cover slip and mounted over the coils. The sample is loaded onto the cover slip and over the central aperture in the stage. The sample is sealed by mounting a second cover slip on top of the pole pieces. A small ring of silicon grease is used to seal the sample and prevent evaporation. The sample is then imaged through the stage aperture using a conventional optical microscope.

Figure 4.2

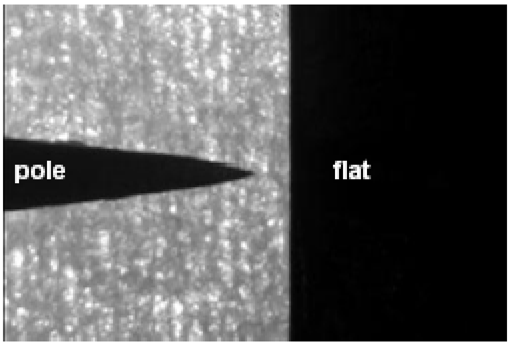

This figure is an optical micrograph of 3DFM pole-flat geometry similar to that used in the ferritin loaded bead magnetophoretic experiments (courtesy Jay Fisher).

Figure 4.3

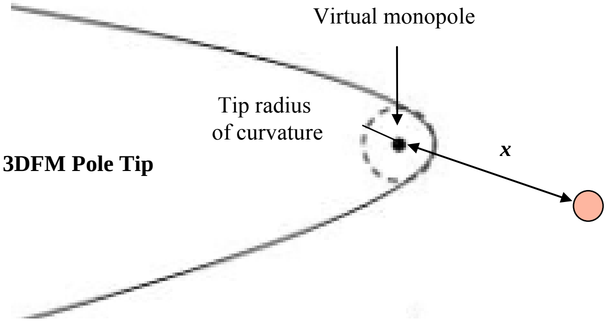

This figure depicts the 3DFM pole tip and a bead. The virtual monopole is defined as the center of the circle constrained by the radius of curvature of the pole tip. The positions *x* of beads were measured with respect to the virtual monopole.

Figure 4.4

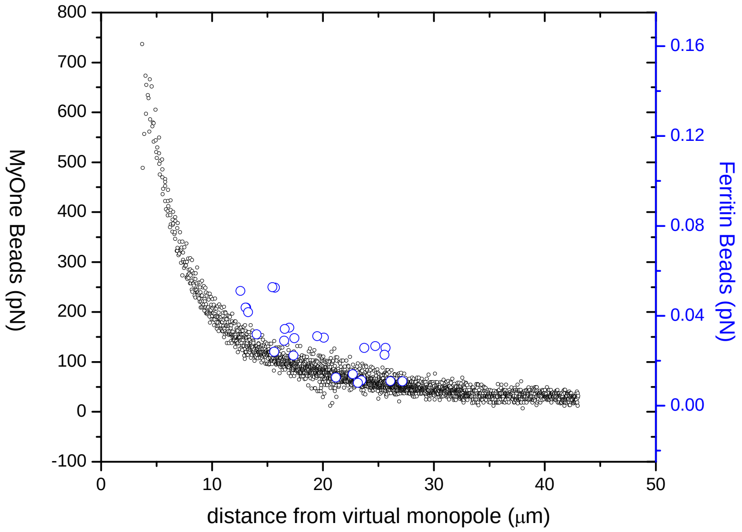

This figure is a plot of the magnetophoretic force on MyOne beads measured by Fisher et al, and the normalized force on ferritin labeled beads in the 3DFM. The magnetic force on the MyOne beads (black) and on the ferritin loaded beads (blue) are plotted as functions of the distance from the virtual monopole in the pole tip of the 3DFM. The forces on the beads were calculated from velocitometry data using a pole-flat geometry with 5V applied to the electromagnetic coils.

The ferritin labeled bead data and the MyOne bead data have independent (color coordinated) Y axes. While the values represented by each Y axis correctly describes the value of the corresponding data set, the data points have been normalized by the force conversion factor of 2.6 x10^{-4} as described by equation 4.7. The close agreement of the MyOne and ferritin bead force data is indicative of a good correlation between the predicted forces on the ferritin loaded beads with the observed forces. The larger absolute value of the exponent in the power law of the ferritin labeled bead data as compared with that of the MyOne beads is indicative of expected saturation of the MyOne beads.

References

1. Odette, L.L., M.A. McCloskey, and S.H. Young, *Ferritin Conjugates as Specific Magnetic Labels - Implications for Cell-Separation.* Biophysical Journal, 1984. **45**(6): p. 1219-1222.

2. Owen, C.S., *High-Gradient Magnetic Capture of Cells and Ferritin-Bound Particles.* Ieee Transactions on Magnetics, 1982. **18**(6): p. 1514-1516.

3. Owen, C.S. and J.G. Lindsay, *Ferritin as a Label for High-Gradient Magnetic Separation.* Biophysical Journal, 1983. **42**(2): p. 145-150.

4. Scott, T.C., *Use of High-Gradient Magnetic-Fields for the Capture of Ferritin.* Aiche Journal, 1989. **35**(12): p. 2058-2060.

5. Zborowski, M., et al., *Immunomagnetic isolation of magnetoferritin-labeled cells in a modified ferrograph.* Cytometry, 1996. **24**(3): p. 251-259.

6. Zborowski, M., et al., *Analytical Magnetapheresis of Ferritin-Labeled Lymphocytes.* Analytical Chemistry, 1995. **67**(20): p. 3702-3712.

7. Zborowski, M., et al., *Modification of Ferrography Method for Analysis of Lymphocytes and Bacteria.* Wear, 1991. **142**(1): p. 135-149.

8. Jones, T.B., *Electromechanics of Particles*. 1995, NY: Press Syndicate of the University of Cambridge.

9. Castner, D.G. and B.D. Ratner, *Biomedical surface science: Foundations to frontiers.* Surface Science, 2002. **500**(1-3): p. 28-60.

10. Ostuni, E., et al., *A survey of structure-property relationships of surfaces that resist the adsorption of protein.* Langmuir, 2001. **17**(18): p. 5605-5620.

11. Sigal, G.B., M. Mrksich, and G.M. Whitesides, *Effect of surface wettability on the adsorption of proteins and detergents.* Journal of the American Chemical Society, 1998. **120**(14): p. 3464-3473.

12. Mrksich, M. and G.M. Whitesides, *Using self-assembled monolayers to understand the interactions of man-made surfaces with proteins and cells.* Annual Review of Biophysics and Biomolecular Structure, 1996. **25**: p. 55-78.

13. Nakanishi, K., T. Sakiyama, and K. Imamura, *On the adsorption of proteins on solid surfaces, a common but very complicated phenomenon.* Journal of Bioscience and Bioengineering, 2001. **91**(3): p. 233-244.

14. Norde, W., *Bioploymers at Interfaces*. 2nd ed. Surfactant Science Series, ed. M. Malsten. Vol. 110. 2003: Marcel Dekker. 908.

15. Shi, L. and K.D. Caldwell, *Mucin adsorption to hydrophobic surfaces.* Journal of Colloid and Interface Science, 2000. **224**(2): p. 372-381.

16. Schneider, S.W., et al., *Molecular weights of individual proteins correlate with molecular volumes measured by atomic force microscopy.* Pflugers Archiv-European Journal of Physiology, 1998. **435**(3): p. 362-367.

17. Jonsson, U., et al., *Real-Time Biospecific Interaction Analysis Using Surface-Plasmon Resonance and a Sensor Chip Technology.* Biotechniques, 1991. **11**(5): p. 620-&.

18. Janshoff, A., H.J. Galla, and C. Steinem, *Piezoelectric mass-sensing devices as biosensors - An alternative to optical biosensors?* Angewandte Chemie-International Edition, 2000. **39**(22): p. 4004-4032.

19. Chehimi, M.M., et al., *Adsorption of macromolecules onto conducting polymers.* Polimery, 1996. **41**(2): p. 75-84.

20. Noh, H. and E.A. Vogler, *Volumetric interpretation of protein adsorption: Competition from mixtures and the Vroman effect.* Biomaterials, 2007. **28**(3): p. 405-422.

21. Simonian, M.H., Smith, John A., *Quantitation of Proteins*, in *Current protocols in molecular biology*. 1996, Wiley: New York.

22. Amblard, F., et al., *A magnetic manipulator for studying local rheology and micromechanical properties of biological systems.* Review of Scientific Instruments, 1996. **67**(3): p. 818-827.

23. Niemeyer, C.M., *Bioconjugation Protocols: Strategies and Methods (Methods in Molecular Biology).* 2004, Totowa NJ: Humana Press.

24. Skoog, D., Leary, James, *Principles of Instrumental Analysis*. 1992: Saunders College Publishers. 681.

25. Fisher, J.K., et al., *Three-dimensional force microscope: A nanometric optical tracking and magnetic manipulation system for the biomedical sciences.* Review of Scientific Instruments, 2005. **76**(5).

26. Fisher, J.K., et al., *Thin-foil magnetic force system for high-numerical-aperture microscopy.* Review of Scientific Instruments, 2006. **77**(2).

27. Connolly, J., T.G. St Pierre, and J. Dobson, *Experimental evaluation of the magnetic properties of commercially available magnetic microspheres.* Bio-Medical Materials and Engineering, 2005. **15**(6): p. 421-431.

CHAPTER FIVE: Magnetic Manipulation of Biomineral Nanoparticles

Introduction

This chapter describes the synthesis of novel ferritin labeled, high aspect ratio calcium phosphate ($Ca_{10}(PO_4)_6(OH)_2$) biomineral nanoparticles and the magnetophoretic manipulation of these particles using a handheld magnet. This is the first report of the synthesis of ferritin biomineral composite nanoparticles as well as the first report of the magnetic concentration of ferritin labeled mineral nanoparticles. This demonstration of the magnetophoretic manipulation of ferritin/biomineral composite nanoparticles has implications in the development of functional biomaterials and as a biologically compatible and biodegradable platform for magnetic particle drug delivery.

The individual mineral and protein components of these novel composite particles have been shown to be biologically compatible enabling their use for in vivo applications.[1] The nanoscale dimensions of the particles are on the order of the microstructures of many biological materials.[2] The relative length scale of the particles as related to biomaterials, the high aspect ratio, the magnetophoretic mobility conferred by the ferritin, and the overall biocompatibility of the materials make these new particles attractive candidates for use as magnetophoretic platforms in biological media.

Hydroxyapatite

Calcium phosphate, referred to in mineralogy as hydroxyapatite (HA), is a common biomineral and a major component of bones and teeth. Nanoparticles of HA have been chemically synthesized in a variety of shapes including high aspect ratio “needle-like” particles, discs and spherical aggregates.[3-5] HA nanoparticles have been used to fabricate medical implants both as a primary component in composites[6, 7] and as a biocompatible coating on metal and ceramic materials.[1] Small biomineral particles, including HA particles, have been proposed as platforms for drug delivery due to their biocompatibility and controllable morphology.[8-10]

Biomaterials

The development of new biomaterials is increasingly drawing inspiration from the properties of biological tissues. One of the characteristics frequently encountered when examining the structure of biological materials is the existence of *functional gradation*.[11] This property of a gradual change from one type of material to another is commonly observed in bones and teeth where a hard biomineral outer layer gives way to a region of soft tissue. Many current synthetic materials used in bone and teeth implants utilize the principle of functional gradation in order to increase the biocompatibility of the material.[12]

The degree of the gradation observed in biological materials varies widely and is specific to the nature of the material. For example, the enamel layer of teeth is less than a millimeter in thickness resulting in a gradation from hard mineral outer layer to a soft interior over a small distance. The structural gradation in bones, however, may occur over tens of millimeters. The degree of the functional gradation of a synthetic biomaterial is therefore dependant on the desired material properties and on the context of the application.[13]

The ability to magnetically control the distribution and localization of biomineral particles would provide a convenient route to the fabrication of novel functionally graded materials. The distribution of particles would be dependant on the applied magnetic field permitting essentially a limitless range of functional gradations depending on the choice of the magnetic field geometry. In addition, the use of a biologically compatible magnetic label would permit functional gradation to be achieved without sacrificing the biocompatibility of the resulting material.

Composite materials formed from HA particles distributed in an entangled biopolymer support matrix such as collagen are commonly used for bone and teeth implants.[12] The system of high aspect ratio particles dispersed in an entangled polymer matrix was described previously in chapter 3 using nickel rods and DNA solutions. The results of that investigation indicated that the high aspect ratio and the nanoscale of HA particles would enable a high degree of magnetophoretic mobility in a polymer matrix such as collagen. Labeling HA particles with ferritin would therefore permit a new level of control over the distribution of HA within the matrix through the application of a magnetic field.

Ferritin/HA Composite Nanoparticles for Magnetic Drug Delivery

Ferritin labeled HA particles also have great potential as biocompatible magnetic drug delivery platforms. The use of small particles as drug delivery vehicles has significant advantages over conventional methods of delivery. Particulate drug delivery systems have demonstrated a controllable release over prolonged periods, and permit the localization of drug release.[14] The use of magnetic particles as the carriers lends added flexibility in directing the distribution of the carriers and thus in the release of the drugs.[15] While the ability to localize drug carrying magnetic particles though the application of magnetic fields is just beginning to be explored as a therapeutic technique, several clinical application are currently in use.[16] Biomineral particles are attractive as a vehicle for drug delivery because they are biocompatible and biologically degraded.[10] The functionalization of biomineral drug delivery particles with a nontoxic magnetic label such as ferritin would permit their manipulated and concentration using an applied magnetic field in order to localize the drug release.

Experimental

Particle Synthesis and Characterization Overview

The HA nanoparticles used in this investigation were prepared by the hydrothermal precipitation of a saturated calcium solution under basic conditions. The HA particles were functionalized with polyacrylic acid (PAA) during synthesis. While native HA bears a net negative surface charge due to the presence of hydroxide groups, functionalization with PAA confers a greater negative surface charge. The negative surface charge served to increase the suspendability of the particles in an aqueous environment. The PAA functionalized HA particles were homogeneously ellipsoidal with dimensions of 10 nm by 100 nm. This was confirmed by scanning electron microscopy (SEM) as shown in figure 5.1**.**

Cationized ferritin was used to magnetically label the HA particles for magnetophoretic manipulation. A transmission electron microscopy (TEM) image of the ferritin alone is presented in figure 5.2 to aid the reader in identifying the protein in later TEM images of HA ferritin composite particles. The large negative surface charge conferred by the PAA functionalization of the HA permitted the attachment of oppositely charged cationized ferritin to the PAA-HA particles through electrostatic physisorbtion. A representative TEM image of ferritin attached to PAA-HA is shown in figure 5.3. A monolayer coverage of ferritin on a PAA-HA particle based on the particle surface area and the cross-sectional area of ferritin predicted a loading of approximately 20 ferritin per HA particle. TEM images of the ferritin labeled HA particles, such as that presented in figure 5.4, suggest that this was a reasonable estimate of ferritin loading on the biomineral particles.

Procedure for Synthesizing HA nanoparticles

1.81 g of calcium hydroxide ($Ca(OH)_2$) was dissolved in 1 L of mili-Q pure water and refluxed at 70^{o} C with stirring. While maintaining heating and stirring, 90 mL of ammonia (NH_3 (28%)) was added. This was followed by the addition of 1 mL of phosphoric acid (H_2PO_4) added drop wise over the course of five minutes. Stirring and refluxing at 70^{o} C were maintained for an additional two hours in order to allow the reaction to proceed to completion. Half of the HA suspension was removed and allowed to cool while the rest of the HA was functionalized with PAA.[17]

Synthesis of PAA-HA

A solution of PAA and NH_3 was prepared by dissolving 0.18 g of PAA (m.w. 2000 g/mol) in 45 mL of NH_3. The PAA solution was added to the refluxing HA suspension half at a time. The first aliquot of the PAA solution was slowly added to the HA suspension and after waiting one hour the remaining PAA solution was slowly added. The reaction solution was continuously stirred and refluxed at 70^{o} C for an additional two hours. The resulting PAA-HA particles were characterized by SEM.

Ferritin Functionalization of PAA-HA

An aliquot of PAA-HA was washed three times with 50 mM pH 5 MES buffer by centrifugation sedimentation to remove reaction byproducts and in order to adjust the pH of the suspension. The PAA-HA was then resuspended in MES buffer following washing. 1.2 mg/mL of cationized ferritin (Sigma-Aldrich) in 50 mM MES pH 5 buffer was incubated with 0.5 mL of PAA-HA suspension overnight. Following incubation, the ferritin PAA-HA was washed in 50 mM pH 5 MES buffer by centrifugation sedimentation, removing the supernatant in order to remove any unbound ferritin from the suspension. The ferritin PAA-HA was then resuspended in mili-Q water. Ferritin functionalization of the PAA-HA particles was confirmed by TEM.

Magnetophoretic Manipulation of Ferritin Labeled HA

The ferritin labeled PAA-HA particles were magnetophoretically manipulated using a 5 cm by 0.5 cm disk shaped, neodymium iron boron handheld permanent magnet. The relative concentration of magnetophoretically deposited HA was determined using

Raman spectroscopy and correlated to the region of the highest applied field and field gradient $B\nabla B$. In order to obtain the maximum magnetic mobility of the HA particles, it was necessary to locate the region of the magnet with the greatest $B\nabla B$ for use in the magnetophoresis of the ferritin labeled HA. A handheld Gaussmeter was used to measure the magnetic field of the magnet as a function of the position from the axial face of the magnet. It was determined from these measurements that the largest value of $B\nabla B$ was located at the edge of the magnet on the face. At this location both B and ∇B had the greatest values, with B equal to 1T and ∇B equal to 10 T/m, resulting in a maximum $B\nabla B$ value at the magnet's edge equal to 10 T^2/m. This high $B\nabla B$ was used to magnetically concentrate ferritin functionalized PAA-HA particles from an aqueous suspension.

The ferritin functionalized PAA-HA particles were magnetically manipulated through the use of a liquid cell containing a small volume (~100 μl) of ferritin PAA-HA suspension. The liquid cell was composed of a PDMS well sandwiched between two number 0 glass coverslips. The top coverslip permitted the Raman laser to penetrate the cell for Raman spectroscopic analysis of the magnetically concentrated particles. A gold coating on the lower coverslip reduced the glass background contribution to the Raman signal. A diagram of the sample cell is shown in figure 5.5. By placing the cell on top of the magnet, ferritin PAA-HA was visibly concentrated on the bottom coverslip. The particles were deposited as a thin band approximately 0.5 mm wide which traced the edge of the permanent magnet as illustrated in the diagram in figure 5.6. Figure 5.7 presents a brightfield optical micrograph at a x5 magnification of the ferritin functionalized PAA-HA particles magnetically concentrated at the edge of the permanent magnet (represented by the dashed curved line). The band of concentrated material had a somewhat diffuse appearance thinning at the edges indicating a higher concentration of HA at the center of the band decreasing away from the edge of the magnet. The diffuse appearance of the concentrated material is consistent with what would be expected for particles which were magnetophoretically concentrated from suspension.

Spatially Resolved Raman Analysis

Raman spectroscopy is a non-invasive, non-destructive characterization method which probes the individual vibrational properties of a material. All Raman spectra were recorded using a Dilor XY triplespectrometer in a backscattering configuration and collected using a CCD cooled with liquid nitrogen (LN_2). The resolution of the spectrometer was 1 cm^{-1}. The 514 nm line of a SpectraPhysics 2017 Argon-ion laser was used as the excitation source. The beam spot on the sample was 1 (±0.1) mm in diameter and the sample was mounted on a micrometer stage allowing for fine control of the positions of individual scans needed to achieve the spatial resolution described.

Results and Discussion

Spatially resolved Raman measurements of the magnetically concentrated band of material revealed a vibrational mode at 961 cm^{-1} which appeared as a sharp peak on top of a broad peak as seen in figure 5.8. Raman analysis revealed that this broad peak was the result of the glass of the coverslip substrate as evinced by the spectrum of glass alone shown in figure 5.9.

Taking spectra both on the band of concentrated material and on the bare glass next to this band revealed that the 961 cm^{-1} peak was correlated with the band of material. Nelson et al, performing Raman measurements of HA, reported the observation of an intense peak at 962 cm^{-1} which was attributed to the totally symmetric $\nu_1(PO_4)$ A_1 stretching mode of the ‘free’ tetrahedral phosphate ion.[18] In addition to the peak at 961 cm^{-1}, a peak at 915 cm^{-1} centered over the broad glass background was observed in the spectrum shown in figure 5.8. Nelson however did not report the observation of a peak in the vicinity of 915 cm^{-1}, nor is one visible in the researchers’ spectra. The peak at 915 cm^{-1} observed in our investigation was not correlated with the band of magnetically concentrated material, nor was it reproducible in other Raman spectra of the sample.

While it was considered likely that the 961 cm^{-1} peak was due to the phosphate vibration mode as observed by Nelson, the components of the suspension in this investigation where analyzed separately to confirm the material source of the vibrational mode. Raman spectra were taken of each of the independent components of the suspension: ferritin, HA, and PAA-HA. The 961 cm^{-1} vibrational mode was observed in samples of both HA and PAA-HA as shown in figures 5.10 and 5.11 respectively.

Raman analysis of the cationized ferritin, however, showed no vibrational modes in the vicinity of the 961 cm^{-1} peak. From these data it was concluded that the 961 cm^{-1} peak was indeed associated with HA, and not simply a result of magnetophoretically concentrated ferritin or residual PAA. The area under the 961 cm^{-1} peak was by definition correlated with the quantity of HA within the scattering volume. The positive identification of the 961 cm^{-1} peak with phosphate in the HA therefore enabled the peak to serve as a metric of the presence of HA.

Assuming that ferritin labeled HA had been magnetically concentrated on the coverslip at the region of high field and field gradient near the edge of the magnet, a decrease in the concentration of HA should be correlated with the decrease in the magnetic field and field gradient. Such a decrease in the field and gradient would indeed occur in moving away from the edge of the magnet as demonstrated by the previously mentioned field and gradient measurements of this magnet. This should have resulted in a decrease in the HA concentration with increasing distance from the magnet's edge. In order to confirm this hypothesis spatially resolved Raman measurements were taken at 2 and 4 mm away from the band.

The areas under the 961 cm^{-1} peaks in the spectra taken at these distances were compared to the peak area of the spectrum taken directly on the band. The peak areas were determined using a numerical peak fitting routine as part of the OriginLab software package. As expected, the area of the 961 cm^{-1} peak decreased as measurements were taken moving away from the band. The peak area of the sample on the band was the greatest and decreased to 21% and 15% of the peak area maximum at 2 mm and 4 mm away from the band respectively. The spatially resolved spectra taken at these distances off the band are shown in relation to the position on the sample in figure 5.12.

Conclusions

Ferritin has many properties that make it attractive as a magnetic label. It is small (24 nm), biologically compatible, and can be chemically functionalized through traditional protein modification chemistry. Furthermore, because ferritin is paramagnetic it has no permanent dipole and thus does not magnetically aggregate. The use of ferritin as a magnetic label, especially in a biological context, has potential applications in a number of fields ranging from materials development to drug delivery. The ability to apply forces at a distance to manipulate biomineral nanoparticles has direct implications in the use of biomineral particles as drug delivery vehicles, and in the fabrication of biomineral based materials. The successful synthesis and magnetic manipulation of ferritin labeled HA nanoparticles has demonstrated the potential application of ferritin labeling and magnetic manipulation of biomineral particles as a means for producing functionally graded materials and for use as a biodegradable magnetic drug delivery system.

Ferritin functionalized drug delivery particles have the potential to be magnetically concentrated at the disease site for directed drug delivery. Because of the biological compatibility of ferritin, its use as a magnetic label would not compromise the inherent ability of biominerals such as HA to be biologically degraded. The magnetic manipulation of ferritin labeled biomineral nanoparticles in biomaterials fabrication would enable the control of the structural composition of the material at the nanoscale. This level of compositional control holds great promise for the development of novel, functionally graded biomaterials.

Raman spectroscopy has been shown to be an effective method for assessing the concentration of deposited HA particles. The identification of an HA vibrational mode at 961 cm^{-1}, enabled the spatially resolved determination of relative HA concentrations which confirmed the magnetophoretic concentration of ferritin PAA-HA particles from suspension. The magnetophoresis of the HA particles was confirmed using spatially resolved Raman spectroscopy to correlate high HA concentration with the area of the greatest applied magnetic field and field gradient.

The magnet source utilized in this study was not selected for its particularly large magnetic field, and the field geometry produced only a modest gradient. Therefore the magnetic forces which were applied to the particles were not very large, but were sufficient for the demonstration of the magnetic manipulation of the nanoparticles. Other magnetic geometries could easily be employed which would be capable of applying greater forces to ferritin labeled biomineral nanoparticles. The method of labeling the particles through the electrostatic attraction of the negatively charged PAA moieties on the HA particles and cationized ferritin provided a convenient means of ferritin loading for this demonstration. Other methods of attachment would certainly be possible which might permit greater ferritin loading with a commensurate increase in the applied magnetic force and the magnetically driven mobility of the particles.

Carbodiimide chemistry was utilized to covalently bond ferritin to the carboxy modified surface of polymer beads as discussed in chapter four. The same attachment chemistry could be applied to covalently link ferritin to PAA-HA particles. The covalent linkage would provide an attachment which would be more robust than the physisorbtion used in this demonstration. Linker molecules such as simple alkane chains or polyethylene glycol (PEG) could also be used to covalently bind ferritin to the particles. These would enable not only the strong attachment of ferritin to the particles but also enable the tuning of the surface properties of the composite particles based on choice of linker. Linker molecules would also serve to increase the surface area of the particles available for ferritin binding thus permitting greater ferritin loading.

Figures

Figure 5.1

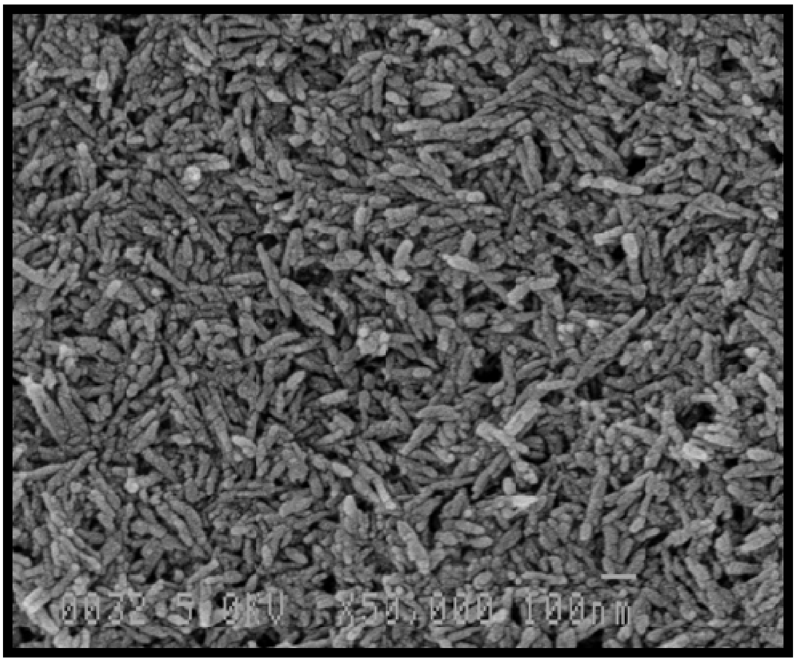

This figure is a SEM micrograph of chemically synthesized polyacrylic acid functionalized hydroxyapatite nanoparticles (PAA-HA). The particle dimensions are 100 nm by 10 nm.

Figure 5.2

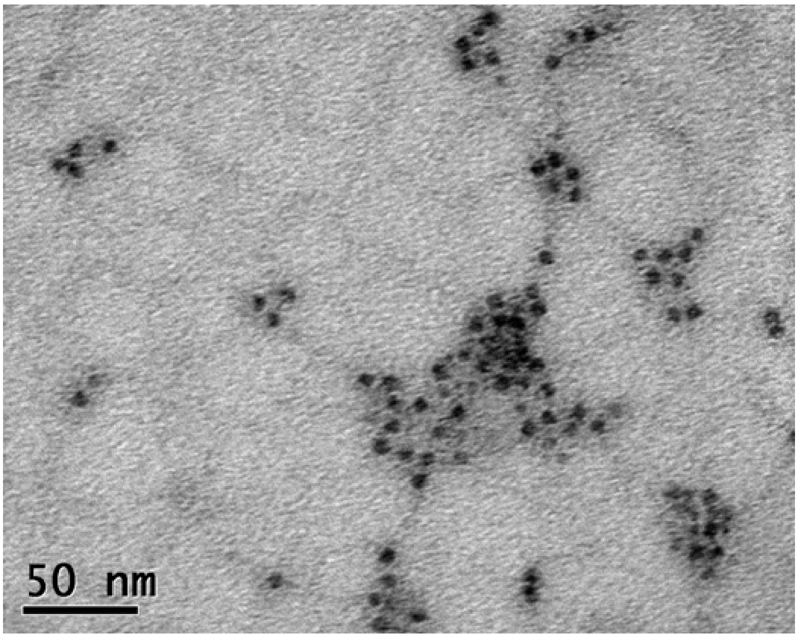

This figure shows a TEM micrograph of native horse spleen derived ferritin. Measurements taken of the ferritin in this image confirmed the diameters of the iron oxide cores of the ferritin to be approximately 6 nm as expected. Wallace Ambrose, UNC is gratefully acknowledged for assistance in obtaining this image.

Figure 5.3

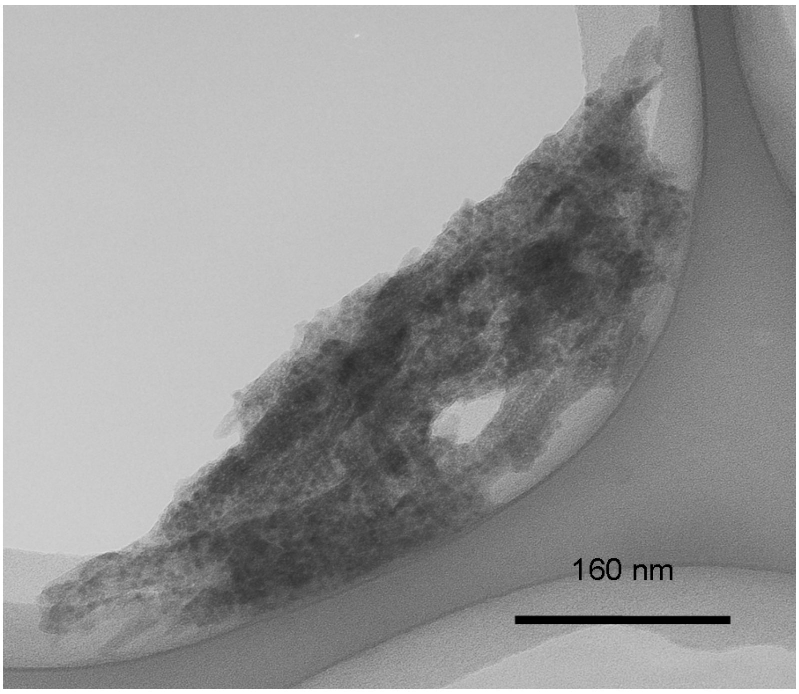

This figure is a TEM image of ferritin functionalized PAA-HA nanoparticles on prepared on a holey carbon TEM grid. The ferritin appear as dark spot covering the needle-like HA particles. Ferritin is not present on the TEM grid except where it is adsorbed to the HA particles confirming the adsorption of ferritin to the HA particles.

Figure 5.4

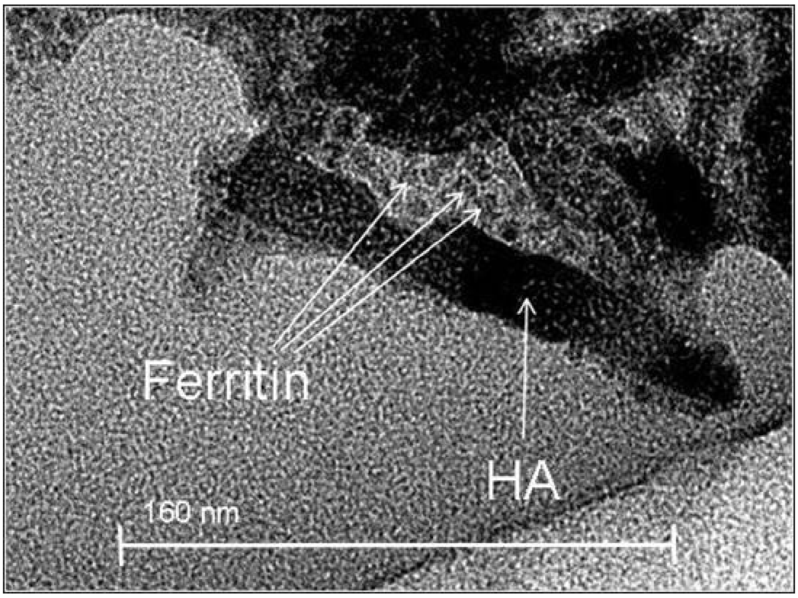

This image shows a high magnification TEM micrograph of ferritin functionalized PAA-HA nanoparticles on the holey carbon TEM grid. The HA particle and three ferritin proteins are labeled and indicated by arrows.

Figure 5.5

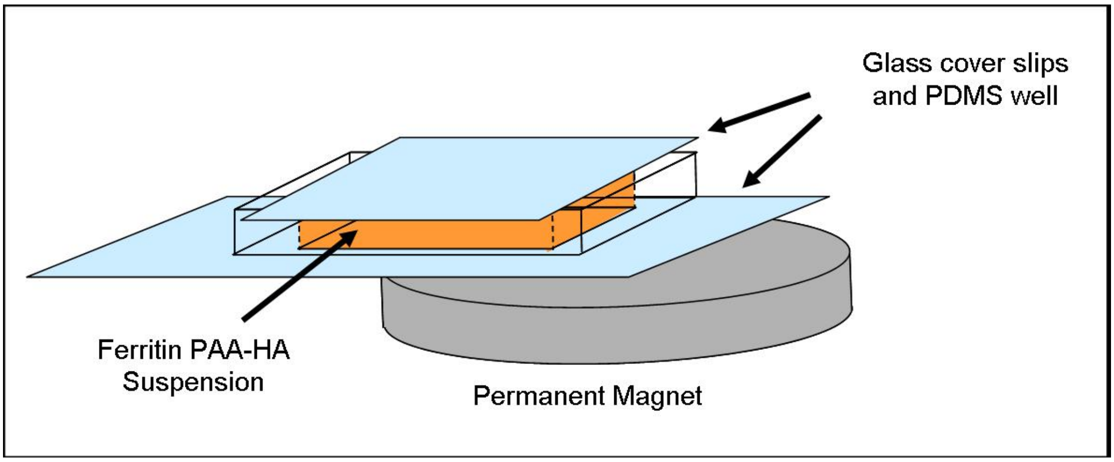

This figure is a schematic of the sample cell which was used to magnetophoretically concentrate ferritin labeled PAA-HA particles from an aqueous suspension. The cell was made by sealing the bottom of a block of PDMS approximately 1 mm thick to a number 0 coverslip. The PDMS block had a hole cut out of the center to form the sample well. The bottom coverslip was coated with gold to minimize the background noise in the Raman spectra. The well was filled with an aqueous suspension of ferritin labeled PAA-HA particles. Another number 0 coverslip was then sealed to the top of the PDMS block in order to contain the suspension. After containing the suspension in the cell it was placed on the edge of the magnet to magnetophoretically concentrate the particles. The depictions in the figure are not to scale.

Figure 5.6

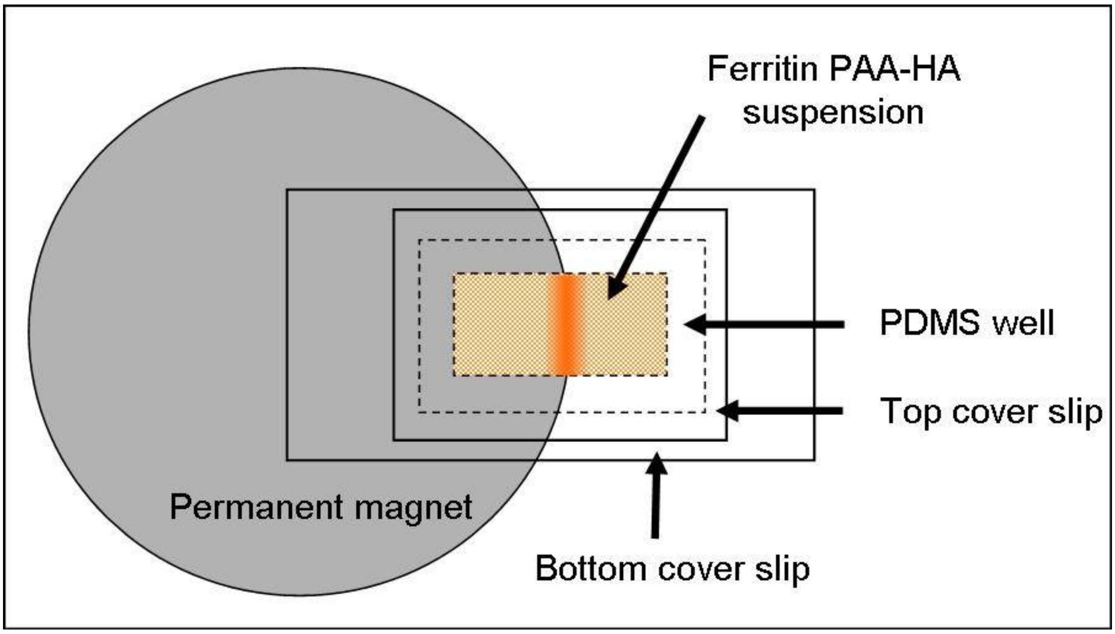

This figure depicts the schematic in figure 5.5 from a top down view to better highlight the location of the magnetically concentrated ferritin PAA-HA particles from aqueous suspension at the edge of the underlying magnet. Particles were magnetophoretically concentrated and deposited on the bottom coverslip by the strong magnetic field gradient present at the edge of the permanent magnet. The depictions in the figure are not to scale.

Figure 5.7

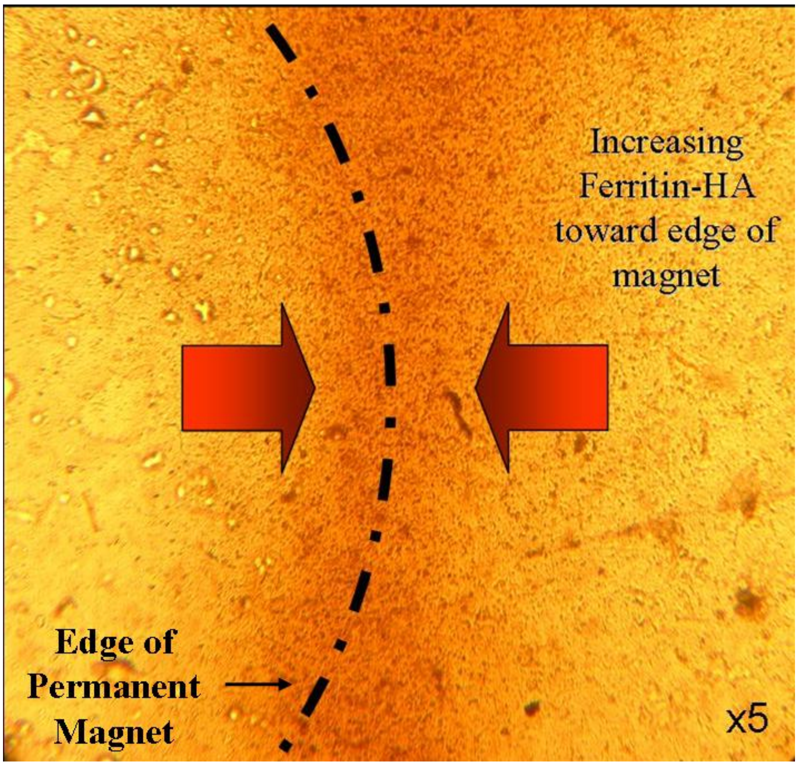

This figure is an optical microscopy (brightfield) image at x5 magnification of the band of magnetophoretically concentrated ferritin PAA-HA particles which were deposited on the bottom gold coated coverslip of the sample cell and depicted in the diagram in figure 5.6. The magnet was removed from under the sample cell in the image to enable better visualization of the magnetophoretically concentrated material. The dotted curved line indicates where the edge of the magnet was located beneath the cell.

Figure 5.8

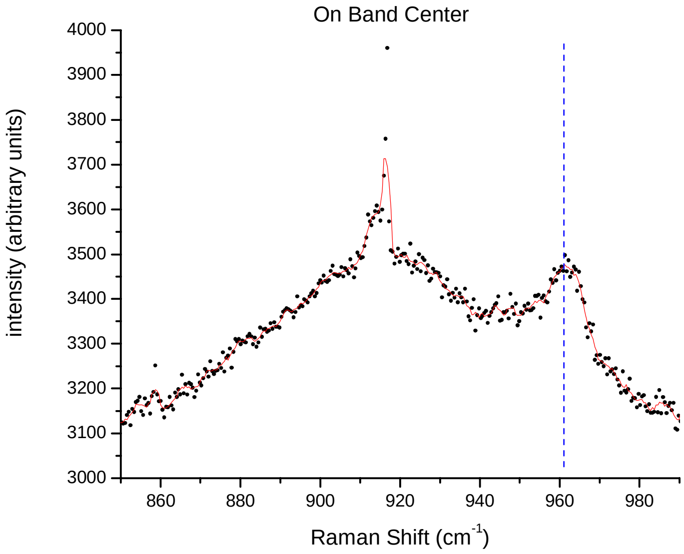

This figure is a Raman spectrum taken on the band of magnetophoretically concentrated ferritin PAA-HA particles. The data are indicated by black points. The red line is the result of averaging of the 5 adjacent points to each data point. The blue dashed line highlights the peak located at a Raman shift of 961 cm^{-1}. The peak was identified as the totally symmetric $\nu_1(PO_{4)}$ A_1 stretching mode of the ‘free’ tetrahedral phosphate ion in the the HA. The peak at 915 cm^{-1} was an anomaly and was not observed in other spectra.

Figure 5.9

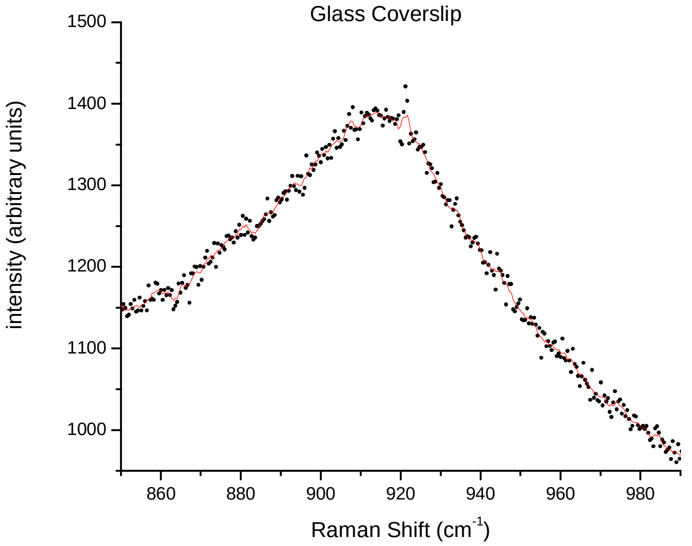

This figure shows the Raman spectrum taken of only the glass coverslip showing the broad background visible in figure 5.8. The data are indicated by black points. The red line is the result of averaging of the 5 adjacent points to each data point.

Figure 5.10

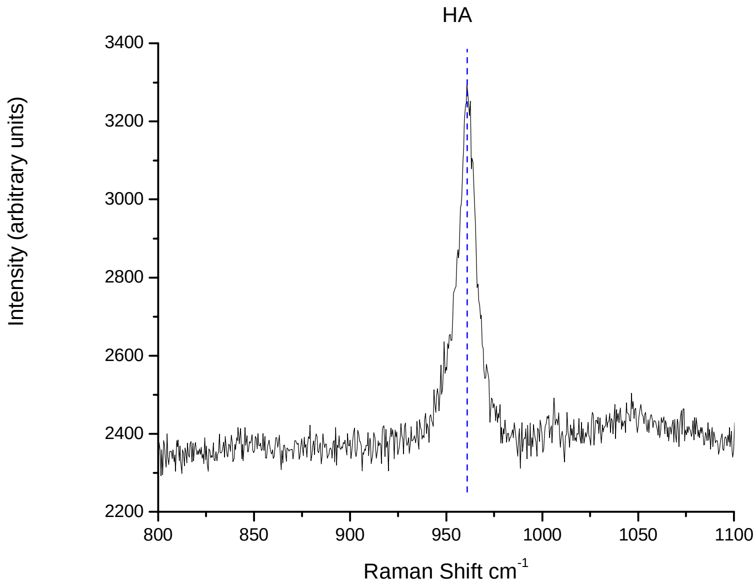

This figure shows the Raman spectrum taken of only the hydroxyapatite (HA) particles which were not functionalized with PAA or ferritin. As in figure 5.8, the blue dashed line highlights the peak located at a Raman shift of 961 cm^{-1}.

Figure 5.11

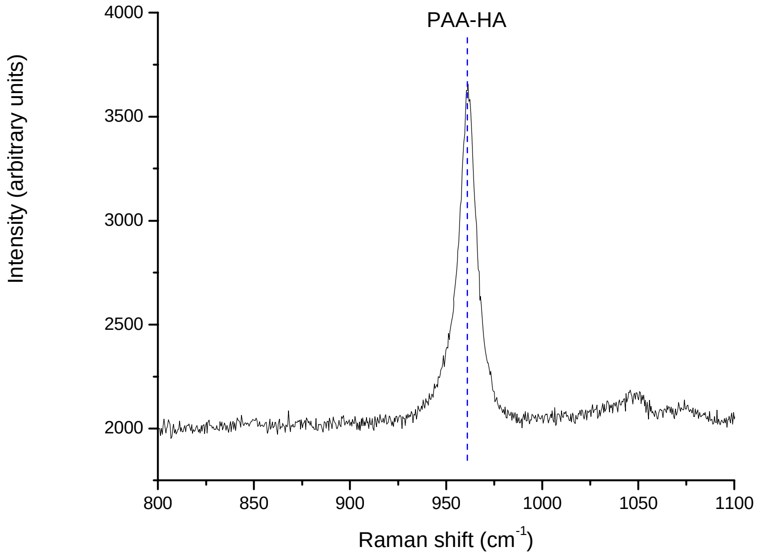

This figure shows the Raman spectrum taken of only polyacrylic acid functionalized Hydroxyapatite (PAA-HA) without ferritin. The dashed blue line highlights the peak located at a Raman shift of 961 cm^{-1} as in the previous figures.

Figure 5.12

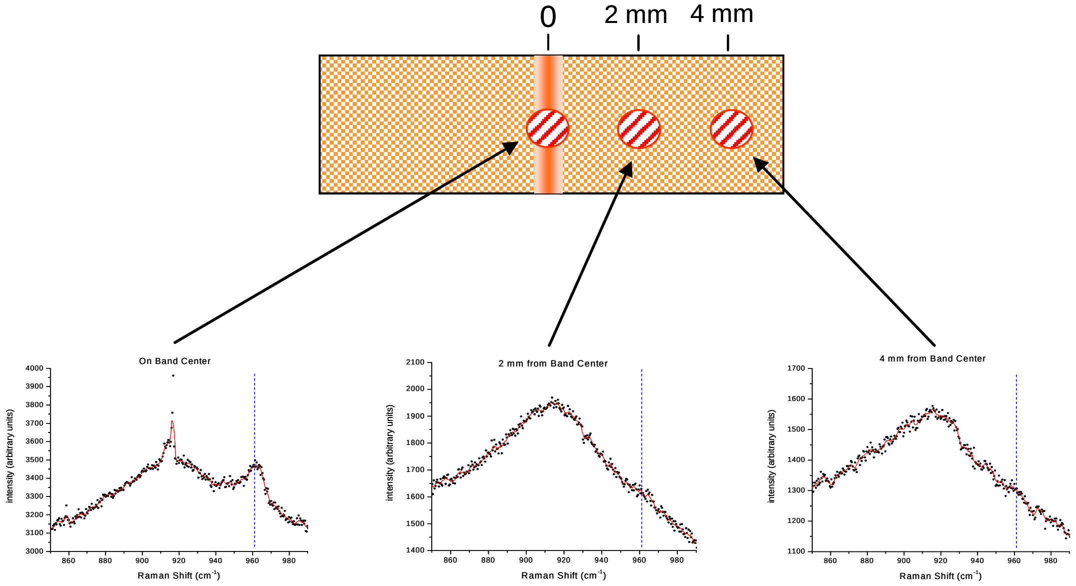

This figure, spatially resolved Raman spectra taken on the band, 2 mm away from the band, and 4 mm away from the band are shown below a diagram of the sample. The red circles represent the location of the Raman laser spot with respect to the band of deposited ferritin PAA-HA. The dotted line in each spectrum is located at a Raman shift of 961 cm^{-1} as previously discussed. The area under the 961 cm^{-1} peak was observed to decrease with distance away from the band indicating a decrease in the amount of deposited HA.

Figure 5.13

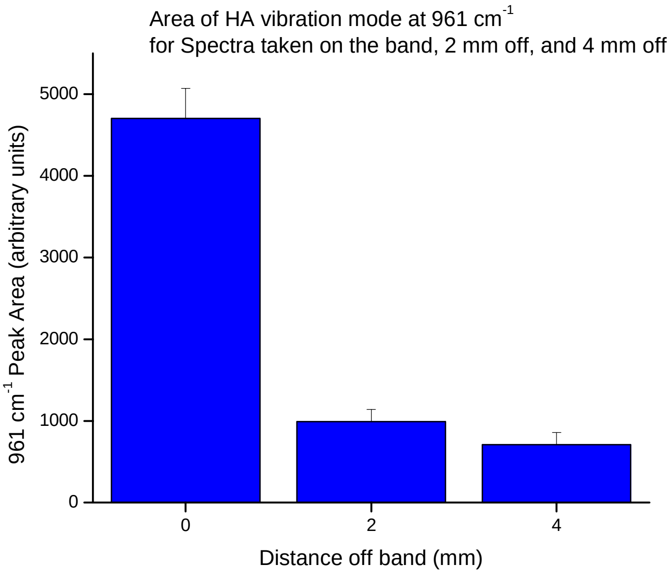

Plotted in this figure are the areas of the 961 cm^{-1} peaks from the spectra taken on the band, 2 mm and 4 mm away from the band shown in figure 5.12 The peak area is a maximum on the band (distance 0) decreasing to 21% of the maximum at 2 mm and further decreases to 15% of the maximum at 4 mm from the band.

References

1. Sun, L.M., et al., *Material fundamentals and clinical performance of plasma-sprayed hydroxyapatite coatings: A review.* Journal of Biomedical Materials Research, 2001. **58**(5): p. 570-592.

2. Torchilin, V.P., *Nanoparticulates as Drug Carriers*. 2006, London: Imperial College Press.

3. Bouyer, E., F. Gitzhofer, and M.I. Boulos, *Morphological study of hydroxyapatite nanocrystal suspension.* Journal of Materials Science-Materials in Medicine, 2000. **11**(8): p. 523-531.

4. Bertoni, E., et al., *Hydroxyapatite polyacrylic acid nanocrystals.* Journal of Materials Chemistry, 1999. **9**(3): p. 779-782.

5. Zhang, S. and K.E. Gonsalves, *Preparation and characterization of thermally stable nanohydroxyapatite.* Journal of Materials Science-Materials in Medicine, 1997. **8**(1): p. 25-28.

6. Furuzono, T., A. Kishida, and J. Tanaka, *Nano-scaled hydroxyapatite/polymer composite I. Coating of sintered hydroxyapatite particles on poly(gamma-methacryloxypropyl trimethoxysilane)-grafted silk fibroin fibers through chemical bonding.* Journal of Materials Science-Materials in Medicine, 2004. **15**(1): p. 19-23.

7. Galego, N., et al., *Characterization and application of poly(beta-hydroxyalkanoates) family as composite biomaterials.* Polymer Testing, 2000. **19**(5): p. 485-492.

8. Duan, Y.R., et al., *Preparation of nano-HAP as vectors for targeting delivery system*, in *Bioceramics, Vol 16*. 2004. p. 887-890.

9. Saleem, I.Y., et al., *Improving peptide-based assays to differentiate between vaccination and Mycobacterium bovis infection in cattle using nanoparticle carriers for adsorbed antigens.* Journal of Controlled Release, 2005. **102**(3): p. 551-561.

10. Zhu, S.H., et al., *Hydroxyapatite nanoparticles as a novel gene carrier.* Journal of Nanoparticle Research, 2004. **6**(2-3): p. 307-311.

11. Yaszemski, *Biomaterials in Orthopedics*. 2004, NY NY: Marcel Dekker.

12. Pompe, W., et al., *Functionally graded materials for biomedical applications.* Materials Science and Engineering a-Structural Materials Properties Microstructure and Processing, 2003. **362**(1-2): p. 40-60.

13. Liu, D.X., *Functional Materials and Biomaterials*. 2007: Springer.

14. Duguet, E., et al., *Magnetic nanoparticles and their applications in medicine.* Nanomedicine, 2006. **1**(2): p. 157-168.

15. Alexiou, C., et al., *Medical applications of magnetic nanoparticles.* Journal of Nanoscience and Nanotechnology, 2006. **6**(9-10): p. 2762-2768.

16. Gijs, M.A.M., *Magnetic bead handling on-chip: new opportunities for analytical applications.* Microfluidics and Nanofluidics, 2004. **1**(1): p. 22-40.

17. Lutton, C.A., *Hydroxyapatite/Polymer Nanocomposite Material for Bone Replacement Implants*, in *Chemistry*. 2003, UQ: Brisbane.

18. Nelson, D.G.A. and B.E. Williamson, *Low-Temperature Laser Raman-Spectroscopy of Synthetic Carbonated Apatites and Dental Enamel.* Australian Journal of Chemistry, 1982. **35**(4): p. 715-727.

APPENDICES

Appendix 1 Magnetic Force

For a magnetically linear, spherical particle the effective dipole moment m_{eff} is expressed through the Clausius-Mossotti function *K* shown in equation a1.0. In equation a1.0 *R* is the radius of the particle, *H* is the magnetic field, μ_2 is the permeability of the particle, and μ_1 is the permeability of the particle's medium.

$$\overline{m}_{eff} = 4\pi R^3 K(\mu_2, \mu_1)\overline{H} \qquad \text{Equation a1.0}$$

The Clausius-Mossotti factor in the above equation is defined in terms of permeability by equation a1.1.

$$K(\mu_2, \mu_1) = \frac{\mu_2 - \mu_1}{\mu_2 + 2\mu_1} \qquad \text{Equation a1.1}$$

The Clausius-Mossotti factor shown in equation a1.1 can also be expressed in terms of susceptibility χ through the following identities

$\mu_1 = \mu_o(\chi_1 + 1)$ and $\mu_2 = \mu_o(\chi_2 + 1)$. Substituting these identities for μ in equation a1.1 results in *K* as a function of χ as shown by equation a1.2.

$$K(\chi_2, \chi_1) = \frac{(\chi_2 + 1)\mu_o - (\chi_1 + 1)\mu_o}{(\chi_2 + 1)\mu_o + 2(\chi_1 + 1)\mu_o} = \frac{\mu_o\left[(\chi_2 + 1) - (\chi_1 + 1)\right]}{\mu_o\left[(\chi_2 + 1) + 2(\chi_1 + 1)\right]} = \frac{\chi_2 - \chi_1}{\chi_2 + 2\chi_1 + 3} \qquad \text{Equation a1.2}$$

For values of χ much smaller than 3 the denominator of *K* in equation a1.2 can be approximated as 3. For typical experiments, where $\chi \approx 10^{-2} - 10^{-6}$, equation a1.2 can be simplified to equation a1.3.

$$K \simeq \frac{\chi_2 - \chi_1}{3} \qquad \text{Equation a1.3}$$

When the susceptibility of the particle is much greater than that of the medium ($\chi_2 \gg \chi_1$), as is often the case for under magnetophoresis conditions, equation a1.3

further simplifies to $K \simeq \frac{\chi_2}{3}$. This simplifying assumption is generally valid for aqueous media and magnetic beads which have a volumetric susceptibility on the order of $\chi_2 \approx 10^{-2}$.

The force *F* on a magnetized particle in a magnetic field gradient is given by equation a1.4.

$$\vec{F} = \left(\mu_o \vec{m}_{eff} \bullet \vec{\nabla}\right) \vec{H} \qquad \text{Equation a1.4}$$

When the effective dipole, as expressed in equation a1.1, is substituted into equation a1.4 we obtain equation a1.5.

$$\vec{\mathrm{F}} = \left(\mu_0 4\pi R^3 K(\mu_2, \mu_1) \vec{H} \bullet \vec{\nabla}\right) \vec{H}\,. \qquad \text{Equation a1.5}$$

By using the previously discussed $3 \gg \chi_2 \gg \chi_1$ approximation, equation a1.5 can be expressed as equation a1.6 or more simply as equation a1.7 where *V* is the volume of the magnetized particle.

$$\vec{\mathrm{F}} = \left(\mu_0 \tfrac{4}{3} \pi R^3 \chi_2 \vec{H} \bullet \vec{\nabla}\right) \vec{H} \qquad \text{Equation a1.6}$$

$$\vec{\mathrm{F}} = \left(\mu_0 V \chi_2 \vec{H} \bullet \vec{\nabla}\right) \vec{H} \qquad \text{Equation a1.7}$$

Equation a1.7 can be rearranged to the conventional equation describing the magnetic force on a particle expressed in terms of the magnetic field *H* as shown in equation a1.8.

$$\vec{\mathrm{F}} = \tfrac{1}{2}\left(\mu_0 V \chi_2 \vec{\nabla}\right) H^2 \qquad \text{Equation a1.8}$$

By common convention, the magnetic force on a particle is often described in terms of the magnetic induction *B* rather than *H*. It is therefore helpful to demonstrate the conversion of the expression for magnetic force shown in equation a1.8 to the expression in terms of *B* as shown in equation a1.14.

The following steps described by equations a.1.9 through a1.14, illustrate the conversion of the magnetic force shown in equation a1.9 in terms of *H* to equation a1.14 in terms of *B*.

$$\vec{\nabla}\left(\vec{A}\bullet\vec{B}\right)=\left(\vec{B}\bullet\vec{\nabla}\right)\vec{A}+\left(\vec{A}\bullet\vec{\nabla}\right)\vec{B}+\vec{B}\times\left(\vec{\nabla}\times\vec{A}\right)+\vec{A}\times\left(\vec{\nabla}\times\vec{B}\right) \qquad \text{Equation a1.19}$$

If $\vec{A}=\vec{B}=\vec{H}$ then the cross product quantities in equation (a1.9) go to zero under electrostatic conditions resulting in only the dot products remaining as shown in equation a1.10 and simplified in equation a1.11.

$$\vec{\nabla}\left(\vec{H}\bullet\vec{H}\right)=\left(\vec{H}\bullet\vec{\nabla}\right)\vec{H}+\left(\vec{H}\bullet\vec{\nabla}\right)\vec{H} \qquad \text{Equation a1.10}$$

$$\vec{\nabla}\left(\vec{H}\bullet\vec{H}\right)=2\left(\vec{H}\bullet\vec{\nabla}\right)\vec{H} \qquad \text{Equation a1.11}$$

Since the dot product of a vector with itself is the square of the magnitude of the vector, equation a.1.12 becomes a1.13.

$$\vec{\nabla}\left(H^2\right)=2\left(\vec{H}\bullet\vec{\nabla}\right)\vec{H} \qquad \text{Equation a1.12}$$

$$\tfrac{1}{2}\vec{\nabla}\left(H^2\right)=\left(\vec{H}\bullet\vec{\nabla}\right)\vec{H} \qquad \text{Equation a1.13}$$

Finally, conversion of *H* to *B* according to the relationship $H=\dfrac{B}{\mu_0}$ enables the formulation of the magnetic force in terms of the magnetic induction as shown in equation a1.14.

$$\vec{F}=\tfrac{1}{2}\frac{V\chi_2}{\mu_0}\vec{\nabla}B^2 \qquad \text{Equation a1.14}$$

Dimensional analysis of equation a1.14 provides confidence in its form. The permittivity of free space μ_o has a value equal to $4\pi x 10^{-7}\dfrac{T\cdot m}{A}$, volume V has units of m^3, the volumetric susceptibility of the particle χ_2 is unitless, and the gradient of B squared ($\vec{\nabla}B^2$) has units of $\dfrac{T^2}{m}$. By substitution of $T=\dfrac{kg}{A\cdot s^2}$ for Tesla, the fundamental units of force $\left(\dfrac{kg\cdot m}{s^2}\right)$ are obtained.

Table a1.0

Magnetic Properties

Term	Symbol	SI unit	CGS unit	Conversion Factor
Magnetic Induction	B	Tesla (T)	Gauss (G)	1 T = 10^4 G
Magnetic Field	H	A/m	Oersted (Oe)	1 A/m = $4\pi/10^3$ Oe
Magnetization	M	A/m	emu/cm^3	1 A/m = 10^{-3} emu/cm^3
Mass Magnetization	σ	Am^2/kg	emu/g	1 Am^2/kg = 1 emu/g
Magnetic Moment	m	Am^2	emu	1 Am^2 = 10^3 emu
Magnetic/Volumetric Susceptibility	χ, κ	Dimensionless	Dimensionless	4π (SI) = 1 (cgs)
Mass Susceptibility	χ/ρ, χ	m^3/kg	emu/Oe g	1 m^3/kg = $10^3/4\pi$ emu/Oe g
Permeability of Free Space	μ_o	H/m	Dimensionless	$4\pi 10^{-7}$ Tm/A, H/m = 1 (cgs)

Appendix 2 Dielectrophoretic Force

The following mathematical description of the dielectric force on a particle with an induced electric polarization should is intended to introduce the reader to the fundamental similarities between the electric and magnetic polarization of particles as well as the forces which may result from the application of field gradients to such polarized particles. The electrical polarization of a particle due to an applied electric field is described in appendix 2 using the Clausius-Mossotti factor in a similar manner as was done previously in appendix 1.0. The effective electric dipole $\left(\overline{p}_{eff}\right)$ is shown in equation a2.0 similar to the expression for a magnetic dipole given in equation a1.0.

$$\overline{p}_{eff} = 4\pi\varepsilon_1 R^3 K(\varepsilon_1,\varepsilon_2)\overline{E}_o \qquad \text{Equation a2.0}$$

Where as the magnetic polarization of a particle was described using the Clausius-Mossotti factor in terms of the permeability in equation a1.1, the effective electric polarization of a particle is described in terms of the permittivity as expressed in equation a2.0. In this equation, ε_2 and ε_1 represent the permitivities of the particle and the medium respectively.

$$K(\varepsilon_2,\varepsilon_1) = \frac{\varepsilon_2 - \varepsilon_1}{\varepsilon_2 + 2\varepsilon_1} \qquad \text{Equation a2.1}$$

The dielectrophoretic force on an a particle having an induced electric dipole in an electric field gradient given by the dot product of the dipole and the field gradient according to equation a2.2.

$$\overline{F}_{DEP} = (\overline{p}_{eff} \bullet \nabla)\overline{E} \qquad \text{Equation a2.2}$$

The substitution of $\left(\bar{p}_{eff}\right)$ from equation a2.0 into equation a2.2 results in the expanded form of the equation given by equation a2.3.

$$\bar{F}_{DEP} = 2\pi\varepsilon_1 R^3 K(\varepsilon_2, \varepsilon_1)\nabla E_o^2 \qquad \text{Equation a2.3}$$

The samples of dielectrophoretic experiments often have permitivities which may be closely related to those of the media. The simplifications which were made to the equations which described magnetic force are thus not functionally helpful. The expression for the dielectrophoretic force on a particle as shown in equation a2.3 will therefore be left in the extended form as it is the most utilitarian.

Table a2.0

	Electrophoresis	Dielectrophoresis	Magnetophoresis	Variable Defined
Phenomena	homogeneous field, monopole	Field Gradient, Electric Dipole	Field Gradient, Magnetic Dipole	
Mobility	$m = \frac{v}{E} = \frac{q}{f}$		$m = \frac{\Delta\chi V}{f}$ $v = {}^2\!/_9 \frac{\Delta\chi}{\mu_o \eta} r^2 (B \bullet \nabla) \bullet B$	f = frictional coefficient, v = velocity
Force Proportionality	$\bar{F} \propto q\bar{E}$	$\bar{F}_{DEP} \propto R^3 K \nabla E_o^2$	$F \propto V \Delta\chi \nabla B^2$	
Force	$\bar{F} = q\bar{E}$	$\bar{F}_{DEP} = 2\pi\varepsilon_1 R^3 K(\varepsilon_2, \varepsilon_1)\nabla E_o^2$	$\bar{F}_{MAG} = 2\pi\mu_o(1+\chi_1)R^3 \frac{\chi_2 - \chi_1}{3 + 2\chi_1 + \chi_2}\nabla H_o^2$	$K(\chi_2, \chi_1) = \frac{\chi_2 - \chi_1}{3 + 2\chi_1 + \chi_2}$
Dipole Moment	NA	$\bar{p}_{eff} = 4\pi\varepsilon_1 R^3 K(\varepsilon_1, \varepsilon_2)\bar{E}_o$	$\bar{m}_{eff} = 4\pi R^3 K(\mu_1, \mu_2)\bar{H}$	$K(\varepsilon_2, \varepsilon_1) = \frac{\varepsilon_2 - \varepsilon_1}{\varepsilon_2 + 2\varepsilon_1}$

Appendix 3 MyOne Hemocytometer Bead Count

A 1:10^4 dilution of MyOne beads were counted by microscopic hemocytometry. Beads were counted in 5 squares in the hemocytometer counting chamber. The dimensions of each square in the chamber were 25 x10^{-5} m x 25 x10^{-5} m and the sample depth was 1 x10^{-4} m. This resulted in a volume per square of 6.25 x10^{-12} m^3. Five squares were counted per sample resulting in a sampling volume of 3.13 x10^{-11} m^3. The average count of the MyOne beads was 74 (±5.6) which resulted in a bead concentration of 2.4 x10^{12} beads per m^3. Accounting for the dilution of the beads from the stock resulted in a stock concentration of 2.4 x10^{16} (±2 x10^{15}) beads per m^3, or 2.4 x10^7 (±8%) beads per μL.

A sample volume of 20 μL stock MyOne bead suspension was analyzed by SQUID susceptometry. According to the hemocytometer count described above, the sample volume corresponded to 4.7 x10^8 (±4 x10^7) beads as shown by equation a3.0.

$$20\mu L \times 2.4 \cdot 10^7 \pm 1.79 \cdot 10^6 \frac{beads}{\mu L} = 4.7 \cdot 10^8 \pm 0.4 \cdot 10^8 \frac{beads}{20\mu L} \qquad \text{Equation a3.0}$$

Appendix 4 Ambient Temperature Magnetic Characterization of Ferritin according to Kilcoyne et al

Kilcoyne et al measured the DC magnetization of freeze dried ferritin at four temperatures using an Oxford instruments vibrating sample magnetometer (VSM) (Figure). Figure a1 (figure 2.5 in chapter 2) is a plot of the mass magnetization (σ) of ferritin as a function of the applied magnetic field (B) at temperatures ranging from 40 K to 290 K. From the plot it is apparent that the magnetization was not linearly dependant on the applied field at low temperatures. At 290 K however, the magnetization as a function of the applied field was well approximated by a linear fit. Figure a1.

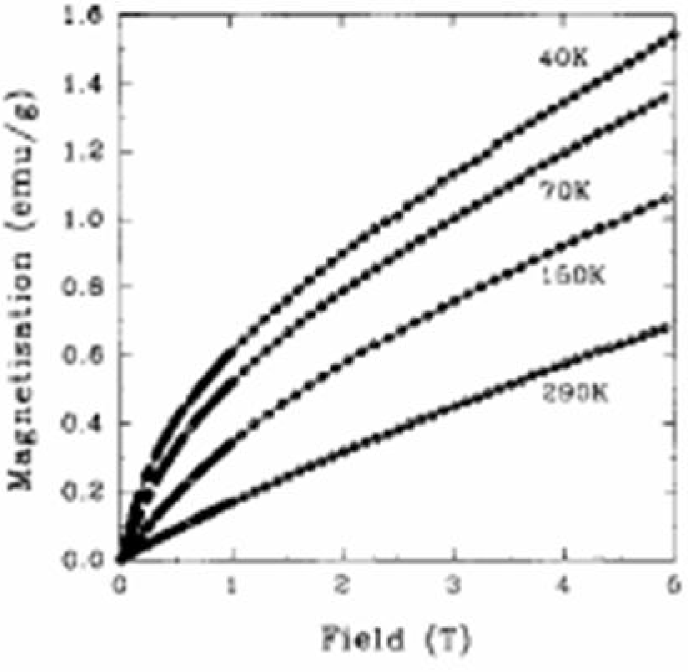

Fig. 4. Typical initial magnetic isotherms obtained from dc magnetisation measurements on ferritin. The solid lines are least-squares fits of the modified Langevin function (discussed in the text) to the data.

[1]

While the graph plots the mass magnetization σ (emu/g) as a function of magnetic induction *B* (T), it is desirable to compare the magnetization to the applied magnetic field strength *H* (A/m) instead. In order to convert *B* to *H* the following relationship is used

$B = \mu_o (H + M)$, where *M* is volume magnetization (A/m, emu/cm^3). Rearrangement of this relationship to solve for *H* results in equation a4.0.

$$H = \frac{B}{\mu_o} - M \,, \qquad \left(\frac{A}{m} = T \frac{A}{Tm} - \frac{A}{m} \right) \qquad \text{Equation a4.0}$$

The volume susceptibility, κ (dimensionless) is related to σ and *H* by equation a4.1 where χ (m^3/kg, emu/Oe·g) is the mass susceptibility and ρ is density.

$$\chi = \frac{\sigma}{H} = \frac{\kappa}{\rho} \,, \qquad \left(\frac{m^3}{kg} = \frac{Am^2}{kg} \frac{m}{A} = \frac{(unitless)}{kg/m^3} \right) \qquad \text{Equation a4.1}$$

κ is related to *M* through equation a4.2.

$$\kappa = \frac{M}{H} \Rightarrow H = \frac{M}{\kappa} \,, \qquad \left(unitless = \frac{A}{m} \frac{m}{A} \Rightarrow \frac{A}{m} = \frac{A/m}{unitless} \right) \qquad \text{Equation a4.2}$$

Substitution of *H,* in terms of equation a4.2, in equation a4.1 shows that *M* is equal to the product of the mass magnetization and the density as in equation a4.3.

$$\frac{\sigma}{M/\kappa} = \frac{\kappa}{\rho} \Rightarrow \frac{\sigma}{M} \kappa = \frac{\kappa}{\rho} \therefore \frac{\sigma}{M} = \frac{1}{\rho} \Rightarrow \sigma\rho = M \qquad \text{Equation a4.3}$$

By substitution of *H* from equation a4.0, equation a4.1 becomes equation a4.4.

$$\sigma\left(\frac{B}{\mu_o}-M\right)^{-1}=\frac{\kappa}{\rho}$$ Equation a4.4

Multiplying equation a4.3 by the density results in equation a4.5.

$$\sigma\rho\left(\frac{B}{\mu_o}-M\right)^{-1}=\kappa$$ Equation a4.5

Substitution of $\sigma\rho$ for M from equation a4.3 into equation a4.5 yields equation a4.6.

$$\sigma\rho\left(\frac{B}{\mu_o}-\sigma\rho\right)^{-1}=\kappa$$ Equation a4.6

The value for the mass magnetization at 3T, σ_{3T} is taken as value for σ although any values in the linear region of the plot would be equally acceptable. The value for σ_{3T} of 0.41 emu/g (0.41 Am^2/kg) is found directly from the plot. The standard density for ferritin is ρ = 2.37 g/cm^3.[2] Therefore the product of $\sigma\rho$ yields a value of M = 9.71×10^2 (A/m). Substitution of this value for M in equation a4.6 results in equation a4.7 where Tesla is equivalent to (H/m) and (A/m).

$$9.71x10^2(A/m)\left(\frac{3T}{4\pi x10^{-7}(H/m)}-9.71x10^2(A/m)\right)^{-1}=\kappa$$

$4.1 \times 10^{-3} = \kappa$ (dimensionless) Equation a4.7

It should be noted that this value is fifty times larger than the ferritin volumetric susceptibility cited by Zborowski et al.[2]

Appendix 5 Nickel Rod Fabrication

The nickel rods used in this investigation were fabricated in house (courtesy of Kwan Skinner) by electrochemical deposition using a commercially available anodized alumina oxide (AAO) membrane (Anadisc, Whatman) as the template. The fabrication method was adapted from a protocol reported by Neilsch et al.[3] The (AAO) membrane (Anadisc, Whatman) membrane had a pore size of 200 nm which defined the diameter of the rods. The membrane had a pore density of 9 $x10^{12}$ pores/ m^2. The diameter of the pores and the number density corresponded to a 28% surface area composed of pore area.

The membrane was sealed on one side by the thermal evaporation of a thin film of silver which served as the working electrode during the deposition process. The membrane was mounted in an electrochemical cell constructed in house. A three electrode setup was employed consisting of a Pt counter electrode, a Ag/AgCl reference electrode, and the membrane itself as the working electrode. A commercial potentiostat/galvanostat (Radiometer Analytical PST050) was used to control the current. A sacrificial film of silver was initially deposited into the bottom of the membrane pores in order to fill the branched portion of the membrane. The silver deposition was performed using a commercial silver plating solution (Silver 1025, Technic) at a current density of approximately 1 mA/cm^2 for 30 minutes. Once the deposition was complete, the silver solution was removed from the cell and the membrane was rinsed three times with distilled water.

The cell was then filled with a nickel plating solution consisting of 300 g/L $NiSO_4$, 45 g/L $NiCl_2$•H_2O, and 45 g/L H_3BO_4. The nickel deposition proceeded for one hour at a current density of approximately 1 mA/cm^2. Upon completion of the deposition process, the plating solution was removed from the cell and the membrane was rinsed three times with distilled water. The evaporated silver layer and the initial deposition of silver were dissolved by immersing the membrane in concentrated nitric acid for 15 seconds. This was repeated once more rinsing the membrane between steps with distilled water. The membrane was then dissolved by immersion in 3M NaOH for 30 minutes.

The NaOH did not dissolve the nickel rods, though it likely reacts with the nickel to form a thin oxide layer on the rods. The NaOH solution containing the free nanorods was replaced with ethanol by centrifugal washing three times. The rods were centrifuged at 4000 rpm for 4 minutes during each washing step without noticeable damage to the rods. Following washing, the rods were resuspended in a 0.01% (v/v) sodium dodecyl sulfate (SDS) solution and sonicated for approximately one hour in order to inhibit flocculation and increase the monodispersity of the rod suspension.

Appendix 6 Uncertainty in Rod Drag Coefficient

The uncertainty in *f* was calculated through equation a6.1 using the uncertainty of *L* according to equation a6.0 where *A* = $2\pi\eta$, *B* = $\left[\ln(200nm)+\nu_{\parallel}\right]$.

$$f=\frac{A\cdot L}{\ln(L)-B}=A\cdot L\left[\left(\ln(L)-B\right)^{-1}\right]$$ Equation a6.0

$$\frac{df}{dL}=A\left(\ln(L)-B\right)^{-1}+A\cdot L\left[-1(\ln(L)-B)^{-2}\right]\frac{1}{L}=A\cdot\left[\left(\ln(L)-B\right)^{-1}-\left(\ln(L)-B\right)^{-2}\right]$$ Equation a6.1

Since $\left(\ln(L)-B\right)^{-1}\gg\left(\ln(L)-B\right)^{-2}$ the second term in equation a6.1 can be eliminated, resulting in equation a6.2.

$$\frac{df}{dL}\approx A\cdot\left(\ln(L)-B\right)^{-1}$$ Equation a6.2

The uncertainty in *f* can be expressed by equation a6.3.

$$\sigma_f=\sqrt{\left(\frac{df}{dL}\right)^2\sigma_L{}^2}=\sqrt{\left(A\cdot\left(\ln(L)-B\right)^{-1}\right)^2\cdot\sigma_L{}^2}$$ Equation a6.3

The uncertainty in *F/L*(μm) was calculated using the uncertainties of *V*, *f*, and *L* according to equations a6.4 and a6.5

$$\frac{\sigma_F}{F/L(\mu m)}=\sqrt{\left(\frac{\sigma_V}{V}\right)^2+\left(\frac{\sigma_L}{L}\right)^2+\left(\frac{\sigma_f}{f}\right)^2}\ \therefore$$ Equation a6.4

$$\sigma_F=\sqrt{\left(\frac{\sigma_V}{V}\right)^2+\left(\frac{\sigma_L}{L}\right)^2+\left(\frac{\sigma_f}{f}\right)^2}\cdot F/L(\mu m)$$ Equation a6.5

Appendix 7 Magnetic Field of Cylindrical Magnet as a Function of Axial Distance

Measurements of the magnetic field magnitude *B* as a function of axial distance from the face of the magnet were taken using a Gaussmeter. The *B* values in Tesla were plotted as a function of the distance *z* in meters. The distant dependant magnetic field data over the range of 3 to 10 mm, corresponding to the distance range utilized in the magnetophoresis mobility experiments of the MyOne beads and nickel rods, were fit to the equation of the magnetic field as a function of axial distance from a cylindrical magnet expressed in equation a7.0 where *R* is the radius and *L* the length of the magnet.

$$B(z)=\frac{M_s\mu_0}{2}\left[\frac{-z}{\sqrt{z^2+R^2}}+\frac{L+z}{\sqrt{(z+L)^2+R^2}}\right] \qquad \text{Equation a7.0}$$

The saturation magnetization M_s is calculated from the measured field magnitude at the face of the magnet. The magnitude of the field measured at the face of the magnet was 0.3545 T, and therefore $B_{magnet}=M_s\mu_o=0.3545$ Tesla. For convenience, the fit was performed using Origin® software using the variables *R*, *L*, and $A=\frac{M_s\mu_0}{2}$, and is shown in figure a7.0. The values of the fit variables and the associated uncertainty are tabulated in table a7.0. The R^2 value of the fit was equal to 0.99011.

Figure a7.0

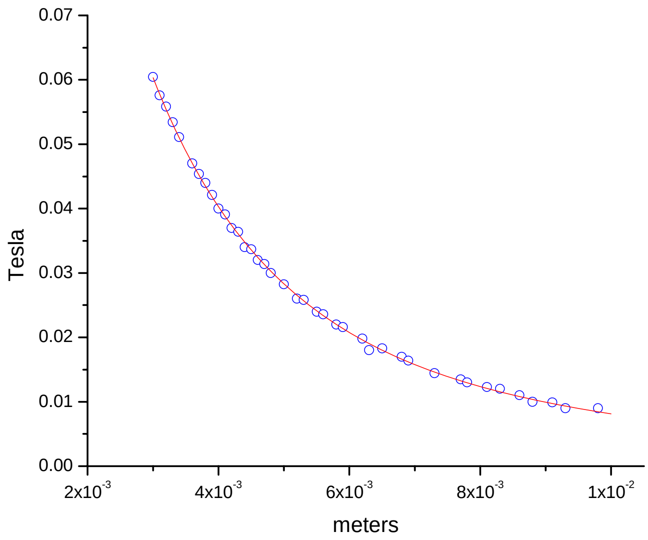

Table a7.0

Variable	Fit Value	Fit Uncertainty
A	0.23053	±0.05043
R	0.09364	±0.0049
L	0.00289	±0.00058

Appendix 8 Determination of Expression for Magnetic Field Characteristics of Permanent Magnet

Expressions for the magnetic field and the field gradient as functions of distance from the permanent magnet were determined using the Mathematica® software package. The fit parameters from the measurements of the magnetic field of the magnetic shown in table a7.0 were used as the variable values in the following equations. Equation a8.0 was the Mathematica compatible representation of equation a7.0, were Chi was used to represent the quantity $\frac{M_s \mu_0}{2}$.

$$A\,\mathrm{Chi}\left(-\frac{x}{\sqrt{R^2+x^2}}+\frac{L+x}{\sqrt{R^2+(L+x)^2}}\right)$$ Equation a8.0

The gradient of the magnetic field in the single direction *x* axially away from the face of the magnet was determined by taking the derivative of equation a8.0, as shown in equation a8.1.

$$-A\left(\frac{x^2}{(R^2+x^2)^{3/2}}-\frac{1}{\sqrt{R^2+x^2}}-\frac{(L+x)^2}{(R^2+(L+x)^2)^{3/2}}+\frac{1}{\sqrt{R^2+(L+x)^2}}\right)$$ Equation a8.1

The magnetic field force proportionality was calculated as the product of equations a8.0 and a8.1, as shown in equation a8.2.

Equation a8.2

$$-A^2\,\mathrm{Chi}\left(\frac{x^2}{(R^2+x^2)^{3/2}}-\frac{1}{\sqrt{R^2+x^2}}-\frac{(L+x)^2}{(R^2+(L+x)^2)^{3/2}}+\frac{1}{\sqrt{R^2+(L+x)^2}}\right)\left(-\frac{x}{\sqrt{R^2+x^2}}+\frac{L+x}{\sqrt{R^2+(L+x)^2}}\right)$$

The uncertainty of the force was determined using the partial derivatives of equation a8.2 with respect to each of the variables A,R,L, and Chi as show in equations a8.3 to a8.6 respectively.

Equation a8.3

$$-2\,A\,\mathrm{Chi}\left(\frac{x^2}{(R^2+x^2)^{3/2}}-\frac{1}{\sqrt{R^2+x^2}}-\frac{(L+x)^2}{(R^2+(L+x)^2)^{3/2}}+\frac{1}{\sqrt{R^2+(L+x)^2}}\right)\left(-\frac{x}{\sqrt{R^2+x^2}}+\frac{L+x}{\sqrt{R^2+(L+x)^2}}\right)$$

Equation a8.4

$$\begin{aligned}&A^2\,\mathrm{Chi}\left(-\left(\frac{R\,x}{(R^2+x^2)^{3/2}}-\frac{R\,(L+x)}{(R^2+(L+x)^2)^{3/2}}\right)\left(\frac{x^2}{(R^2+x^2)^{3/2}}-\frac{1}{\sqrt{R^2+x^2}}-\frac{(L+x)^2}{(R^2+(L+x)^2)^{3/2}}+\frac{1}{\sqrt{R^2+(L+x)^2}}\right)-\right.\\&\quad\left.R\left(-\frac{3\,x^2}{(R^2+x^2)^{5/2}}+\frac{1}{(R^2+x^2)^{3/2}}+\frac{3\,(L+x)^2}{(R^2+(L+x)^2)^{5/2}}-\frac{1}{(R^2+(L+x)^2)^{3/2}}\right)\left(-\frac{x}{\sqrt{R^2+x^2}}+\frac{L+x}{\sqrt{R^2+(L+x)^2}}\right)\right)\end{aligned}$$

Equation a8.5

$$A^2\,\mathrm{Chi}\,R^2\left(\frac{-\frac{x^2}{(R^2+x^2)^{3/2}}+\frac{1}{\sqrt{R^2+x^2}}+\frac{(L+x)^2}{(R^2+(L+x)^2)^{3/2}}-\frac{1}{\sqrt{R^2+(L+x)^2}}}{(R^2+(L+x)^2)^{3/2}}+\frac{3\,(L+x)\left(L\sqrt{R^2+x^2}+x\sqrt{R^2+x^2}-x\sqrt{R^2+(L+x)^2}\right)}{\sqrt{R^2+x^2}\,(R^2+(L+x)^2)^3}\right)$$

Equation a8.6

$$-A^2\left(\frac{x^2}{(R^2+x^2)^{3/2}}-\frac{1}{\sqrt{R^2+x^2}}-\frac{(L+x)^2}{(R^2+(L+x)^2)^{3/2}}+\frac{1}{\sqrt{R^2+(L+x)^2}}\right)\left(-\frac{x}{\sqrt{R^2+x^2}}+\frac{L+x}{\sqrt{R^2+(L+x)^2}}\right)$$

The uncertainty was calculated according to equation a8.7.

Equation a8.7

$$\begin{aligned}\sqrt{\Bigg(}&4.87539\times10^{-29}\,A^4\left(\frac{x^2}{(R^2+x^2)^{3/2}}-\frac{1}{\sqrt{R^2+x^2}}-\frac{(L+x)^2}{(R^2+(L+x)^2)^{3/2}}+\frac{1}{\sqrt{R^2+(L+x)^2}}\right)^2\left(-\frac{x}{\sqrt{R^2+x^2}}+\frac{L+x}{\sqrt{R^2+(L+x)^2}}\right)^2+\\&0.0101727\,A^2\,\mathrm{Chi}^2\left(\frac{x^2}{(R^2+x^2)^{3/2}}-\frac{1}{\sqrt{R^2+x^2}}-\frac{(L+x)^2}{(R^2+(L+x)^2)^{3/2}}+\frac{1}{\sqrt{R^2+(L+x)^2}}\right)^2\left(-\frac{x}{\sqrt{R^2+x^2}}+\frac{L+x}{\sqrt{R^2+(L+x)^2}}\right)^2+\\&3.364\times10^{-7}\,A^4\,\mathrm{Chi}^2\left(-\left(\frac{R\,x}{(R^2+x^2)^{3/2}}-\frac{R\,(L+x)}{(R^2+(L+x)^2)^{3/2}}\right)\left(\frac{x^2}{(R^2+x^2)^{3/2}}-\frac{1}{\sqrt{R^2+x^2}}-\frac{(L+x)^2}{(R^2+(L+x)^2)^{3/2}}+\frac{1}{\sqrt{R^2+(L+x)^2}}\right)-\right.\\&\quad\left.R\left(-\frac{3\,x^2}{(R^2+x^2)^{5/2}}+\frac{1}{(R^2+x^2)^{3/2}}+\frac{3\,(L+x)^2}{(R^2+(L+x)^2)^{5/2}}-\frac{1}{(R^2+(L+x)^2)^{3/2}}\right)\left(-\frac{x}{\sqrt{R^2+x^2}}+\frac{L+x}{\sqrt{R^2+(L+x)^2}}\right)\right)^2+\\&0.00002401\,A^4\,\mathrm{Chi}^2\,R^4\left(\frac{-\frac{x^2}{(R^2+x^2)^{3/2}}+\frac{1}{\sqrt{R^2+x^2}}+\frac{(L+x)^2}{(R^2+(L+x)^2)^{3/2}}-\frac{1}{\sqrt{R^2+(L+x)^2}}}{(R^2+(L+x)^2)^{3/2}}+\frac{3\,(L+x)\left(L\sqrt{R^2+x^2}+x\sqrt{R^2+x^2}-x\sqrt{R^2+(L+x)^2}\right)}{\sqrt{R^2+x^2}\,(R^2+(L+x)^2)^3}\right)^2\Bigg)\end{aligned}$$

Appendix 9 Ferritin Susceptibility

Ferritin is made up of an iron core, averaging 4 nm in diameter, surrounded by a spherical protein shell. The protein shell has essentially the same susceptibility as the surrounding aqueous media, and therefore the susceptibility of the protein can be assumed to be solely due to the iron core. The susceptibility of ferritin, while higher than water, is not orders of magnitude greater. It is therefore appropriate to include the influence on the effective magnetization of ferritin due to the aqueous medium. A polymeric bead functionalized with ferritin will have an effective magnetization m_{eff} proportional to the number of ferritin proteins N_{ferr}, the difference between the susceptibilities of ferritin and water $\Delta\chi = \chi_{ferr} - \chi_{H_2O}$, and the volume of an individual iron core V_{ferr}.

$m_{eff} \propto N_{ferr}\Delta\chi V_{ferr}$. The effective magnetization is therefore described by equation a9.0.

$$m_{eff} = N_{ferr}\Delta\chi V_{ferr} = N_{ferr}\left[87.9\text{x}10^{-6} - (-9.0\text{x}10^{-6})\right]\left[\tfrac{4}{3}\pi(4nm)^3\right] \quad \text{Equation a9.0}$$

Appendix 10 Ferritin Loading Quantification

4 mg of beads were covalently functionalized with ferritin. Based on the manufacturer's specifications this mass of beads corresponded to 4.2 x10^7 beads. Based on solution depletion 59.9 μg of ferritin was loaded on the bead sample corresponding to 1.4 x10^{-12} g of ferritin loaded per bead as shown in equation a10.0.

$$\frac{59.9\mu g}{4.2\cdot 10^7 beads}=\frac{1.4\cdot 10^{-12}g}{bead} \qquad \text{Equation a10.0}$$

Ferritin has an average molecular weight (including the iron core) of 750 kDa resulting in a mass of 1.2 x10^{-18} g per ferritin molecule. Using this mass per ferritin the average number of ferritin molecules loaded on a bead was calculated to be 1.2 x10^6 according to equation a10.1.

$$\frac{ferritin}{1.2x10^{-18}g}\frac{59.9x10^{-6}g}{4.2x10^7 beads}=1.2x10^6 \text{ ferritin per bead} \qquad \text{Equation a10.1}$$

A simple spatial estimation of the monolayer equivalents which equates to the number of ferritin per bead can be made using the surface area of a bead and the cross sectional area of the spherical ferritin molecule. It was determined, through equation a10.2, that 2.4 x10^5 ferritin had the cross sectional area equal to the surface area of a 6 μm bead. The radius of a bead (r_{bead}) was 3mm and the radius of a ferritin molecule ($r_{ferritin}$) was 12 nm.

$$\frac{4\pi r_{bead}{}^2}{\pi r_{ferritin}{}^2}=\frac{1.1x10^{-10}m^2}{4.5x10^{-16}m^2}=2.4x10^5 \text{ ferritin per one monolayer} \qquad \text{Equation a10.2}$$

Based on the result of the above calculation, it was calculated that the average number of ferritin loaded on a bead corresponded to 5 monolayers equivalents as shown by equation a10.3.

$$\frac{1.2x10^{6}\ ferritin}{bead}\frac{monolayer}{2.4x10^{5}\ ferritin}\approx 5 \text{ monolayers per one bead} \qquad \text{Equation a10.3}$$